SEDIMENTOLOGY the journal of the International Association of Sedimentologists

Sedimentology (2019) doi: 10.1111/sed.12642

From marine bands to hybrid flows: Sedimentology of a Mississippian black shale

JOSEPH F. EMMINGS*† , SARAH J. DAVIES*, CHRISTOPHER H. VANE†, VICKY MOSS-HAYES† and MICHAEL H. STEPHENSON†
*School of Geography, Geology and the Environment, University of Leicester, University Road, Leicester, LE1 7RH, UK (E-mail: josmin65@bgs.ac.uk)
†British Geological Survey, Keyworth, Nottingham, NG12 5GG, UK

ABSTRACT

Organic-rich mudstones have long been of interest as conventional and unconventional source rocks and are an important organic carbon sink. Yet the processes that deposited organic-rich muds in epicontinental seaways are poorly understood, partly because few modern analogues exist. This study investigates the processes that transported and deposited sediment and organic matter through part of the Bowland Shale Formation, from the Mississippian Rheic–Tethys seaway. Field to micron-scale sedimentological analysis reveals a heterogeneous succession of carbonate-rich, siliceous, and siliciclastic, argillaceous muds. Deposition of these facies at basinal and slope locations was moderated by progradation of the nearby Pendle delta system, fourth-order eustatic sea-level fluctuation and localized block and basin tectonism. Marine transgressions deposited bioclastic 'marine band' (hemi)pelagic packages. These include abundant euhaline macrofaunal tests, and phosphatic concretions of organic matter and radiolarian tests interpreted as faecal pellets sourced from a productive water column. Lens-rich (lenticular) mudstones, hybrid, debrite and turbidite beds successively overlie marine band packages and suggest reducing basin accommodation promoted sediment deposition via laminar and hybrid flows sourced from the basin margins. Mud lenses in lenticular mudstones lack organic linings and bioclasts and are equant in early-cemented lenses and in plan-view, and are largest and most abundant in mudstones overlying marine band packages. Thus, lenses likely represent partially consolidated mud clasts that were scoured and transported in bedload from the shelf or proximal slope, as a 'shelf to basin' conveyor, during periods of reduced basin accommodation. Candidate *in situ* microbial mats in strongly lenticular mudstones, and as rip-up fragments in the down-dip hybrid beds, suggest that these were potentially key biostabilizers of mud. Deltaic mud export was fast, despite the intrabasinal complexity, likely an order of magnitude higher than similar successions deposited in North America. Epicontinental basins remotely linked to delta systems were therefore capable of rapidly accumulating both sediment and organic matter.

Keywords Bowland Shale, epicontinental seaway, mudstone, organic matter.

INTRODUCTION

Syn-rift to early post-rift epicontinental seaways, such as the Mississippian Rheic-Tethys, were distinct from 'static' interior seaways such as the Cretaceous Western Interior Seaway (Schieber, 2016). These extensional epicontinental marine settings are often associated with the accumulation of organic-rich sediments (Ettensohn, 1997) and are therefore important sinks in terms of element cycling and hydrocarbon prospectivity. Yet the sedimentary processes operating in epicontinental rifted seaways are spatially and temporally transient (Cope *et al.*, 1992) and typified by highly variable sediment supply rates, with potential for development of highly complex successions.

The depositional processes that operated in the Mississippian Rheic-Tethys seaway are poorly understood partly because modern analogues are rare (Nyberg & Howell, 2015). This is especially true for the organic-rich upper unit of the Bowland Shale Formation (Upper Bowland Shale; herein 'Bowland Shale'), deposited in the Rheic-Tethys seaway, defining a key transition between the carbonate-dominated Lower Bowland Shale (Newport *et al.*, 2018) and the Millstone Grit Group, a siliciclastic toe of slope fan system (Holdsworth & Collinson, 1988; Aitkenhead *et al.*, 1992; Martinsen *et al.*, 1995; Waters *et al.*, 2009). The Bowland Shale is also the primary target for unconventional hydrocarbon exploration in the UK (Andrews, 2013; Clarke *et al.*, 2018) and in equivalents across Europe, including the Geverik Member (Epen Formation, Netherlands; e.g. Nyhuis *et al.*, 2015) and Upper Alum Shale Formation, Germany (Kerschke & Schulz, 2013). The Bowland Shale is partly age equivalent to the Barnett Shale, a producing unconventional hydrocarbon reservoir (Titus *et al.*, 2015). Despite this interest, the Bowland Shale is poorly understood beyond a few regional (Fraser & Gawthorpe, 1990) and basin-specific studies (Davies *et al.*, 2012; Könitzer *et al.*, 2014; Słowakiewicz *et al.*, 2015; Fauchille *et al.*, 2017; Hennissen *et al.*, 2017; Newport *et al.*, 2018).

To investigate mechanisms of sediment input, transport and deposition, sedimentological observations at field/core to micron-scale were integrated with geochemical proxies for autochthonous [total organic carbon (TOC), carbonate and silica] and allochthonous components (Ti and Zr). This analysis was conducted for three time-equivalent sites in the Craven Basin, UK (Kirby *et al.*, 2000), a basin with ongoing unconventional hydrocarbon exploration (DECC, 2016; Clarke *et al.*, 2018). This study shows that organic-rich sediments accumulated in a dynamic environment host to pelagic to hemipelagic deposition and a variety of subaqueous density flows, moderated by fourth-order eustatic sea-level fluctuation, delta progradation and slope instability, and under variable bottom water salinity. This complexity means that sedimentary packages are interpreted in terms of changing basin accommodation rather than strictly within a sequence stratigraphic framework. Sea-level fall enhanced a shelf to basin bedload conveyor of sand to gravel-sized partially-consolidated mud clasts, as modelled by Schieber *et al.* (2010), which was remotely linked to a mud-rich delta system. The current study contributes to the debate (Schieber, 1994) that shows accumulation of organic-rich sediments is not necessarily coupled to the depositional 'energy' of bottom waters (*sensu* Tissot & Welte, 1978). These findings are important for understanding sedimentary processes and controls on organic carbon burial in epicontinental basins (Berner & Canfield, 1989; Schieber, 2016) and understanding hydrocarbon resource potential (Aplin & Macquaker, 2011).

GEOLOGICAL SETTING

Bowland Shale sediments were deposited in a palaeoequatorial seaway comprising several epicontinental basins that extended from present-day North America to Poland (Davies *et al.*, 1999). This seaway developed in response to oblique collision between Gondwana and Laurussia (Warr, 2000), including phases of

Fig. 1. Palaeogeographic reconstructions during the Mississippian (A) Late Brigantian and (B) Early Arnsbergian of the British Isles. Based upon Waters *et al.* (2009) and Dean *et al.* (2011), with the permission of the British Geological Survey, after Cope *et al.* (1992). AsB: Askrigg Block, CB: Craven Basin. (C) Generalized Visean–Serpukhovian lithochronostratigraphy. Ages from Waters & Condon (2012) after Gastaldo *et al.* (2009) and Davydov *et al.* (2010). Craven Basin composite after Newport *et al.* (2018) and Brandon *et al.* (1998). Estimated areal extent for marine bands from Waters & Condon (2012), including diagnostic ammonoid fauna from Riley (1990). Mesothem definitions from Ramsbottom (1973, 1977). HS: Hind Sandstone Member, PG: Pendle Grit Member, including the Surgill Shale (S), as part of the Pendleton Formation, RC: Rogerley Channel (Dunham, 1990).

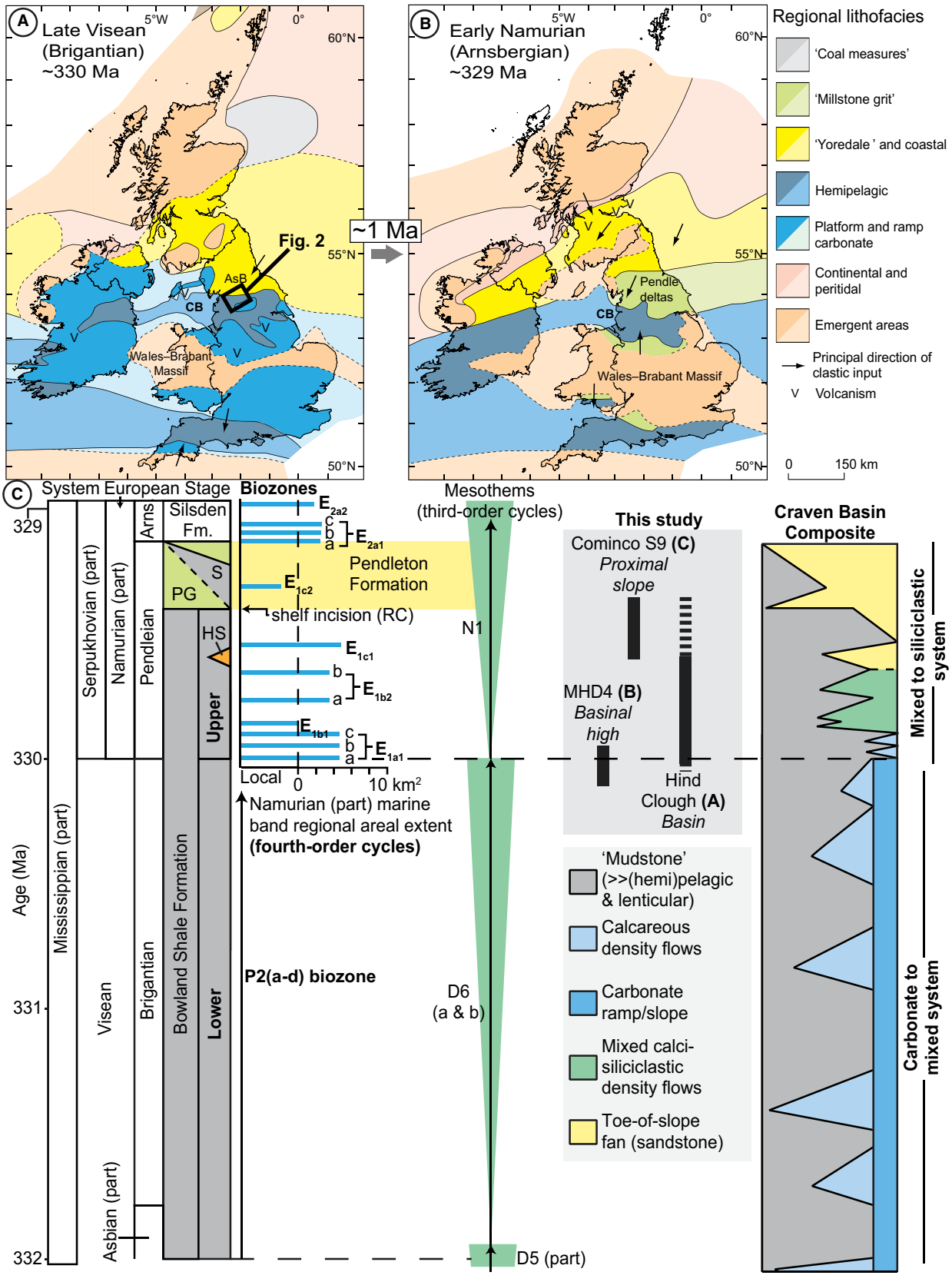

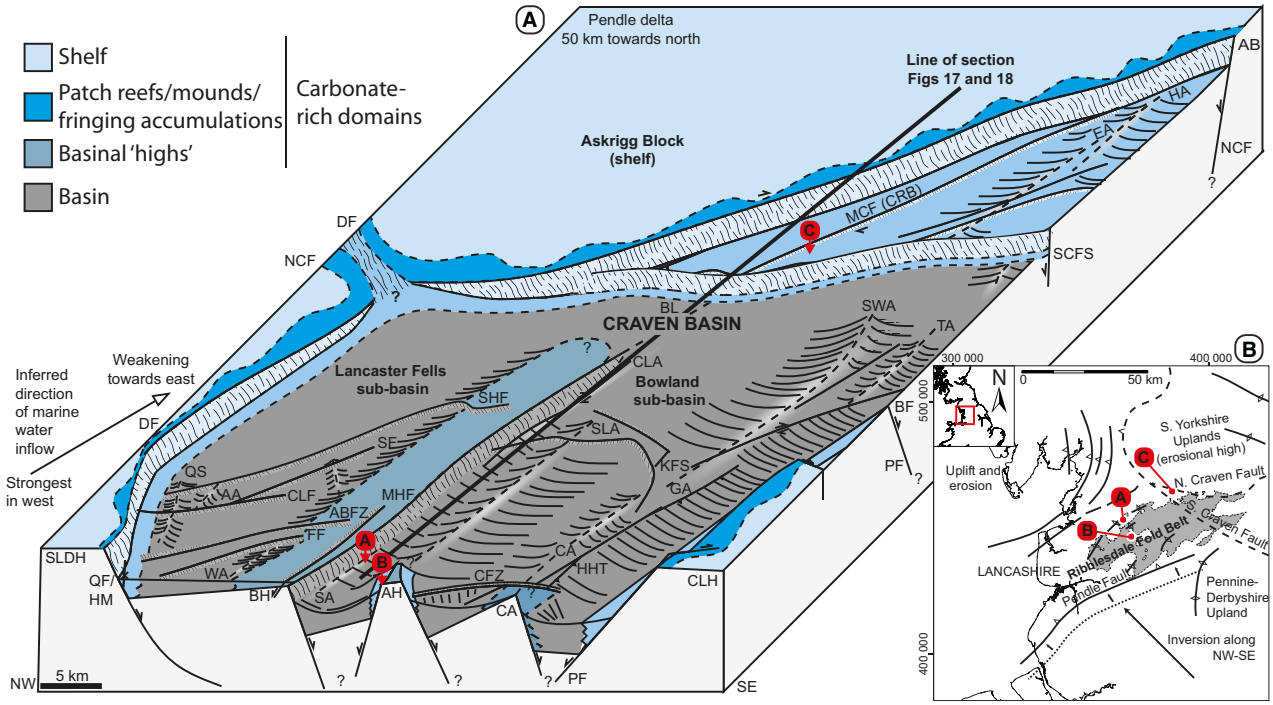

Fig. 2. (A) Inherited Late Brigantian palaeogeography, with approximate positions of Hind Clough (location A), MHD4 (location B) and Cominco S9 (location C) (red circles). After Aitkenhead *et al.* (1992); Brandon *et al.* (1998); Fraser & Gawthorpe (1990, 2003); Riley (1990); Kane (2010); Waters & Condon (2012). AA: Aughton Anticline, ABFZ: Artle Beck Fault Zone, AH: Ashnott High, BF: Barnoldswick Fault, BH: Bowland High, BL: Bowland Line, CA: Clitheroe Anticline, CFZ: Clitheroe Fault Zone, CLA: Catlow Anticline, CLF: Claughton Fault, CLH: Central Lancashire High, DF: Dent Fault (Line), EA: Eshton Anticline, FF: Foxdale Fault, GA: Gisburn Anticline, HA: Hetton Anticline, HHT: Horrocksford Hall Thrust, KFS: Knotts Fault System, MHF: Millers House Fault, NCF: North Craven Fault, PF: Pendle Fault (monocline), QF/HM: Quernmore Fault/Hutton Monocline, QS: Quernmore Syncline, SA: Sykes Anticline, SCFS: South Craven Fault Zone, SF: Stauvin Fault, SHF: Smeer Hall Fault, SLA: Slaidburn Anticline, SLDH: Southern Lake District High, SWA: Swinden Anticline, TA: Thornton Anticline, WA: Ward's Stone Anticline. Structures developed in response to phases of basin rifting and inversion (e.g. Arthurton, 1984; Gawthorpe, 1987; Kirby *et al.*, 2000), some of which may have been absent, inactive, or intermittently active, during the Pendleian. (B) Location map with main structural elements (after Fraser & Gawthorpe, 2003). Outcrop extent data based on DigMapGB-625, with permission of the British Geological Survey. British National Grid projection.

extension (for example, active rifting), thermal subsidence, strike-slip and compression tectonism. Mississippian extension (Leeder, 1982) generated a series of graben and half-graben structures, separated by platform 'blocks' and 'highs', referred to as a 'block and basin' topography (Figs 1A and 2A) (Waters & Davies, 2006). Transition from active rifting to thermal subsidence broadly aligns with subdivision of the Bowland Shale Formation into lower and upper units at the Visean–Serpukhovian boundary (Bisat, 1923; Earp, 1961; Waters *et al.*, 2009)

Fig. 3. (A) Summary sedimentary logs through the Bowland Shale section exposed at Hind Clough and borehole sections Marl Hill 4 (MHD4) and Cominco S9 (letters in red; correspond to Fig. 2). Biostratigraphy from Arthurton (1972), Riley (1988) and Brandon *et al.* (1998), respectively. Please see the text for full lithofacies descriptions including definition based on grain-size. Approximate mud lens (intraclast) grain size (Ø) is interpolated between thin sectioned samples. (B) Log–log mean sediment accumulation rate (SAR) plotted versus time span (115 120 binned data points, with calculated median values and 1σ (thick) and 3σ (thin) error bars), for siliciclastic sedimentary systems, after Sadler (1981), Sadler (1999) and Sadler & Jerolmack (2014). Mean SARs are also estimated for the Upper Bowland Shale (this study), and the Lower Bowland Shale (Newport *et al.*, 2018), Barnett Shale (Loucks & Ruppel, 2007), Morridge Formation (Gross *et al.*, 2015; Hennissen *et al.*, 2017), Woodford Shale (Harris *et al.*, 2013), Holywell Shale (Newport *et al.*, 2018) and Kansas-type cyclothems (Algeo *et al.*, 2008).

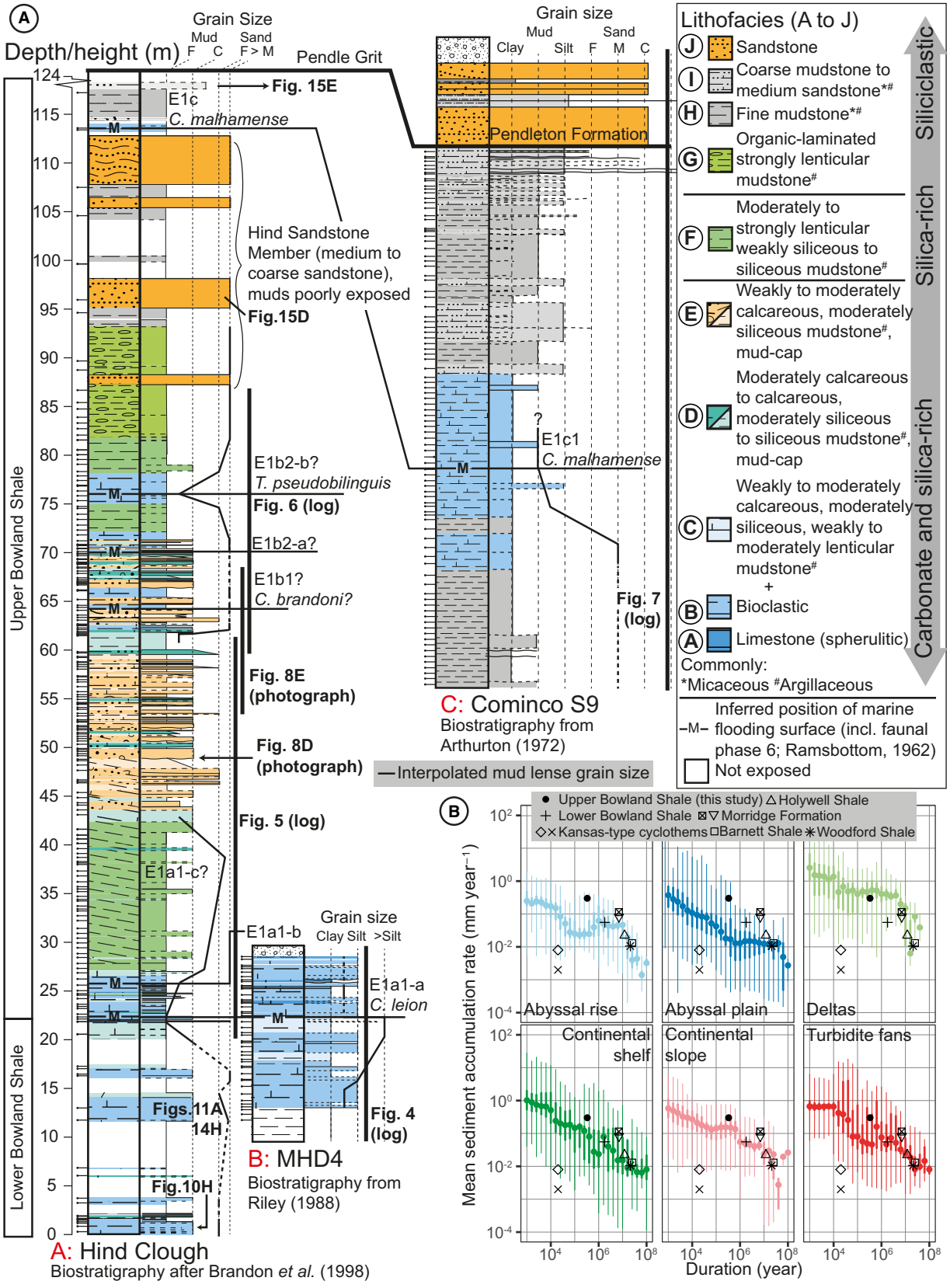

(Fig. 1A to C). The Upper Bowland Shale (this study) was deposited from the early to late Pendleian in the Craven Basin (*ca* 330·0 to 330·7 Ma; Gastaldo *et al.*, 2009; Davydov *et al.*, 2010; Waters & Condon, 2012; Fig. 1C).

Upper Bowland Shale sediments initially accumulated in inherited Visean syn-rift depocentres (Fig. 2A; e.g. Fraser & Gawthorpe, 2003), in water depths ranging from *ca* 100 to 200 m (Holdsworth & Collinson, 1988; Davies, 2008) or several hundred metres (Davies *et al.*, 1993) in the Craven Basin. The basinal slope was likely relatively steep (>1°). Adjacent shelves in the north were likely at least 50 km wide (Waters *et al.*, 2009), including the Askrigg Block and Southern Lake District High, bounded by the Craven Fault Zone and Dent Fault. The Central Lancashire High in the south-east is bounded by the Pendle monocline (Fig. 2A) (e.g. Aitkenhead *et al.*, 1992). The Bowland High, a relatively large intrabasinal titled block (Lawrence *et al.*, 1987), separates the Lancaster Fells and Bowland sub-basins (Brandon *et al.*, 1998) (Fig. 2A) and possibly connects to the Askrigg Block in the north-east (Arthurton *et al.*, 1988). These adjacent shelves and highs were 'shallow' water settings (Elliott, 1975; Dunham & Wilson, 1985; Fairbairn, 2001), and assuming relatively sheltered conditions (Peters & Loss, 2012), likely <50 m deep.

In the earliest Pendleian, basinal highs and lows supported highly localized 'platform and ramp carbonate' and 'hemipelagic' regional facies belts (Fig. 1A), respectively (e.g. Dean *et al.*, 2011). This represented a short-lived inheritance of the Lower Bowland Shale carbonate to mixed sedimentary system (Newport *et al.*, 2018). Mud mounds, patch reefs and/or similar carbonate accumulations likely fringed the Craven Basin during this early stage of post-rift fill (Fig. 2A; e.g. Cope *et al.*, 1992; Waters *et al.*, 2009; Dean *et al.*, 2011). This included localized deposition of Wendsleydale Group crinoidal limestones, and brachiopod–mollusc-rich Sugar Loaf Shales and Sugar Loaf Limestone. These accumulated along the south-west margin of the Askrigg Block on a series of relay ramps across the Craven Fault Zone (Fig. 1) (Arthurton *et al.*, 1988; Fairbairn, 2001). The Bowland High, in addition to other intrabasinal highs such as the Ashnott High, also hosted localized carbonate accumulations (Riley, 1990; Brandon *et al.*, 1998).

Marine bands

Onset of fourth-order (Mitchum & Van Wagoner, 1991) sea-level fluctuation prompted deposition of discrete, macrofauna-bearing, commonly carbonate-rich sedimentary packages termed 'marine bands' during the Namurian (Fig. 1C) (e.g. Ramsbottom, 1977). On shelves, marine bands are comparable to the 'condensed sections' of Loutit *et al.* (1988). These packages typically mark the base of marine to non-marine coarsening-upward packages of the classic 'Yoredale' cyclic regional facies ('cyclothems'), comprising limestone–shale–sandstone triplets commonly capped by coal (Hampson *et al.*, 1997; Waters *et al.*, 2009; Dean *et al.*, 2011). In basins, marine bands are typically <2 m thick and often overlie 'transitional', fossil-'barren' mudstones (Martinsen *et al.*, 1995). Together these mudstone packages are often overlain by turbidite siltstones and sandstones (Martinsen *et al.*, 1995). Basinal marine band packages and underlying 'transitional' mudstones were likely deposited during maximum marine flooding (Martinsen *et al.*, 1995) and the maximum rate of transgression (Posamentier *et al.*, 1988), respectively.

The Upper Bowland Shale includes four index marine bands; E_{1a1} to E_{1c1} (e.g. Brandon *et al.*, 1998) spanning *ca*. 400 ka (Waters & Condon, 2012). Multiple flooding surfaces are recognized for E_{1a1} (a, b and c) and E_{1b2} (a and b) marine bands (Fig. 1C), potentially linked to sub-100 ka precession or obliquity forcing (Waters & Condon, 2012): E_{1a1} and E_{1c1} are also thought to represent peak highs associated with eccentricity (Maynard & Leeder, 1992; Waters & Condon, 2012). Marine band cyclicity in the Namurian was likely a response to far-field ice-sheet volume on Gondwana (Veevers & Powell, 1987). Marine band cycles are possibly superimposed onto 1·1 to 1·35 Ma duration Namurian 'mesothem' cycles (Ramsbottom, 1979), which

Fig. 4. Sedimentary log through the Upper Bowland Shale in borehole Marl Hill 4 (MHD4). Hand specimen description based on Lazar *et al.* (2015). Biostratigraphy from Riley (1988). See *Materials and methods* for a description of methods, including sedimentary classification scheme and derivation of excess Si. Approximate mud lens (intraclast) diameter (*Ø*) and abundance estimated for thin sectioned samples only. HB = high basin accommodation, DB = decreasing basin accommodation, LB = low basin accommodation, IB = increasing basin accommodation. See *Discussion* for further details and Fig. 3 for lithofacies descriptions based on composition.

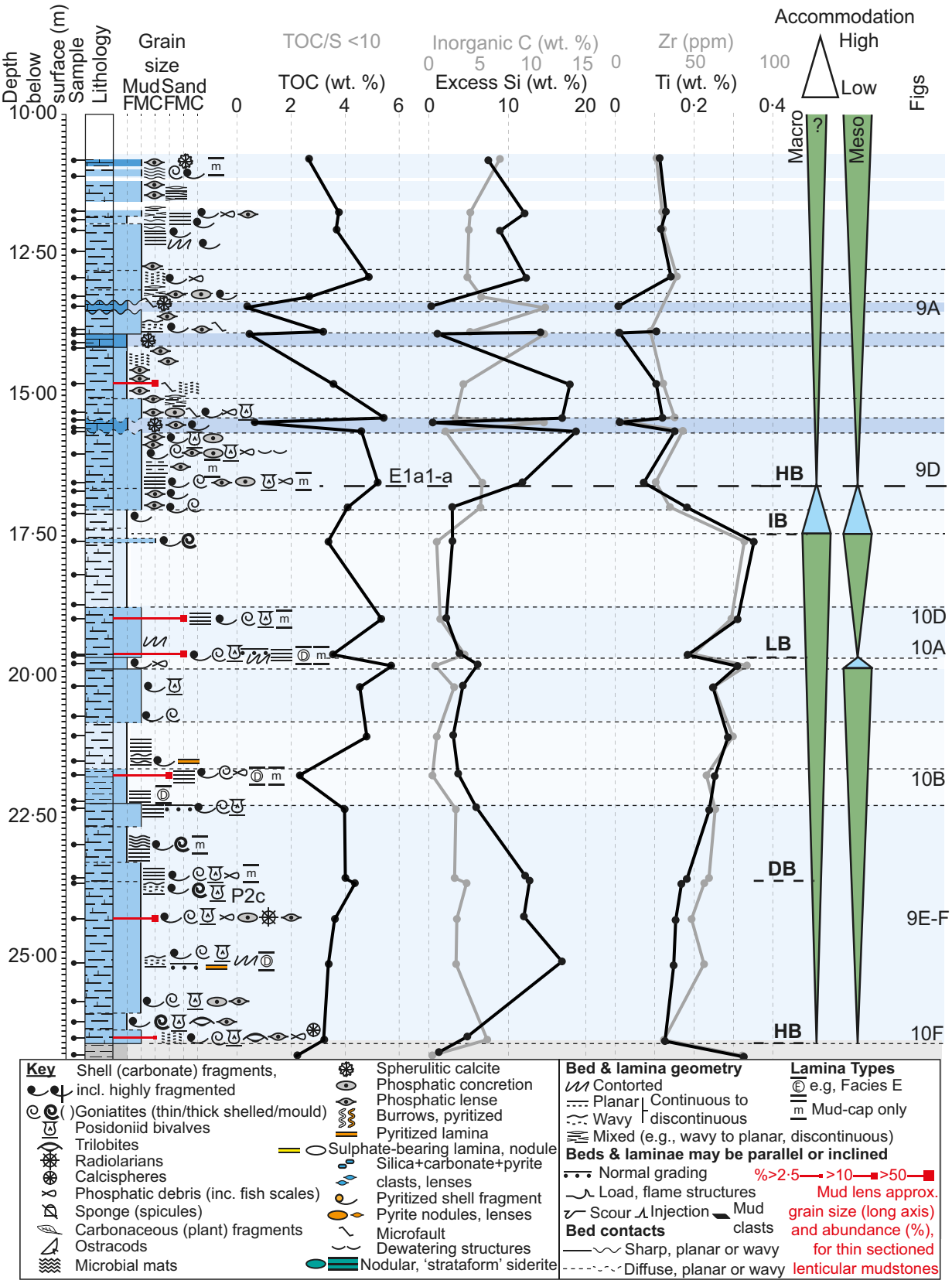

may represent third-order sequences (Posamentier *et al.*, 1988) or avulsive shifts of sediment depocentres in response to localized tectonic uplift and subsidence effects (Holdsworth & Collinson, 1988; Martinsen *et al.*, 1995). Estimates for the amplitude of sea-level cycles ranges between 42 m (Maynard & Leeder, 1992) and 60 to 100 m (Church & Gawthorpe, 1994; Rygel *et al.*, 2008).

Basinal marine bands typically lack or exhibit a low diversity of ichnofossils (e.g. Ramsbottom *et al.*, 1962; Baines, 1977; Eagar *et al.*, 1985; *contra* Loutit *et al.*, 1988) but contain a framework of abundant, low diversity, thin-shelled and thick-shelled macrofaunal body fossils hosted within a mud-rich matrix (e.g. Bisat, 1923; Ramsbottom *et al.*, 1962). Macrofauna are used to differentiate the marine bands from intervening mudstones and permit a high-resolution biostratigraphic framework (Ramsbottom & Saunders, 1985; Holdsworth & Collinson, 1988). Marine bands and overlying mudstones may exhibit a complete faunal succession (phases 6 to 1); thick shelled goniatites (6), thin shelled goniatites (5), molluscan spat (4), *lingula* (3), *planolites* (2), fish remains (1) and barren zones (Ramsbottom *et al.*, 1962; Baines, 1977; Ramsbottom, 1977). These faunal phases are thought to indicate cycling between euhaline (6) and freshwater conditions (1) (Ramsbottom *et al.*, 1962; Holdsworth & Collinson, 1988).

The Pendle delta system

The inherited carbonate to mixed syn-rift system was gradually inundated by siliciclastic sediments ultimately attributed to the 'millstone grit' (deltaic) regional lithofacies (Fig. 1B). Siliciclastic sediments were supplied primarily from advancing fluvio-deltaic and turbiditic systems, linked to the Pendle delta system in the north to north-east (Pendleton Formation; Waters *et al.*, 2009), across and around the Askrigg Block (Arthurton *et al.*, 1988; Martinsen, 1993; Fraser & Gawthorpe, 2003; Kane, 2010). Presence of relatively large distributary channels towards the north of the Askrigg and Alston Blocks, such as the 50 m deep Rogerley Channel, suggest that the Pendle delta likely discharged a large volume of freshwater particularly during flood events (Dunham, 1990; Waters & Condon, 2012). Despite proximity to the Pendle delta, fault activity likely maintained sharp and steep basin margins (i.e. probably 2 to 10°) rather than ramps (Collinson, 1988; Martinsen *et al.*, 1995), which were likely prone to failure (Talling, 2014).

Siliciclastic facies include the Hind Sandstone Member (Moseley, 1952, 1962; Aitkenhead *et al.*, 1992), a sandstone injectite (Kane, 2010) and a variety of 'turbidite' facies often banked against topographic slopes (Collinson, 1988). These were followed by deposition of delta-top facies on the Askrigg Block and a turbidite fan in the basin (Fraser & Gawthorpe, 1990; Kirby *et al.*, 2000) (Fig. 1C). Detrital kaolinite and mixed-layer illite–smectite typically dominate the allochthonous mud fraction in approximately equal proportions (Spears, 2006). Subordinate detrital quartz, feldspar, muscovite and chlorite are often partitioned into the silt to sand-sized fraction (Brandon *et al.*, 1998; Spears, 2006). These components were probably derived from drainage of a variety of igneous and metamorphic rocks in the hinterland (Drewery *et al.*, 1987; Collinson, 1988).

MATERIALS AND METHODS

Three localities in the Craven Basin were selected for analysis; the outcrop at Hind Clough (grid ref: 364430 453210, British National Grid projection) and boreholes Marl Hill 4 (MHD4) (367426 446752) and Cominco S9 (383090 463300) (Fig. 2B). Hind Clough and MHD4 are located on a basinal low and high, respectively. Cominco S9 is located on the north-east basin slope proximal to the Pendle palaeodelta. The stratigraphic framework was based on ammonoid biozones identified by Brandon *et al.* (1998), Riley (1988) and Arthurton (1972), respectively. The *ca* 124 m thick section at Hind Clough is exposed as a stream-cut and

Fig. 5. Sedimentary log through the E_{1a} biozone at Hind Clough. Hand specimen description based on Lazar *et al.* (2015). Biostratigraphy from Brandon *et al.* (1998). See *Materials and methods* for a description of methods, including sedimentary classification scheme and derivation of excess Si. Approximate mud lens (intraclast) diameter (*Ø*) and abundance estimated for thin sectioned samples only. HB = high basin accommodation, DB = decreasing basin accommodation, LB = low basin accommodation, IB = increasing basin accommodation. LTPF = Lower Transitional Plug Flow, QLPF = Quasi-Laminar Plug Flow. See *Discussion* for further details; Fig. 3 for lithofacies descriptions based on composition and Fig. 4 for legend.

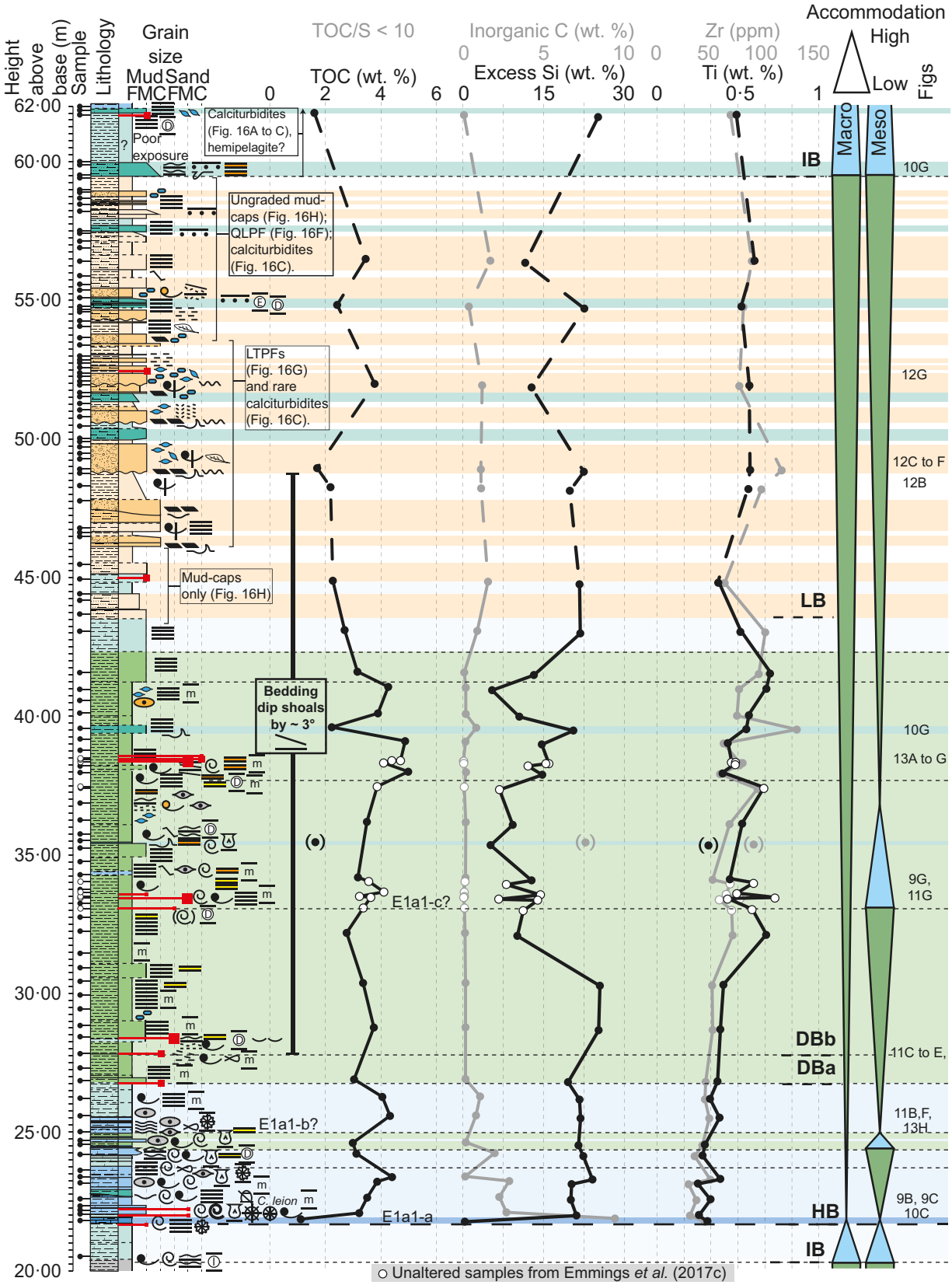

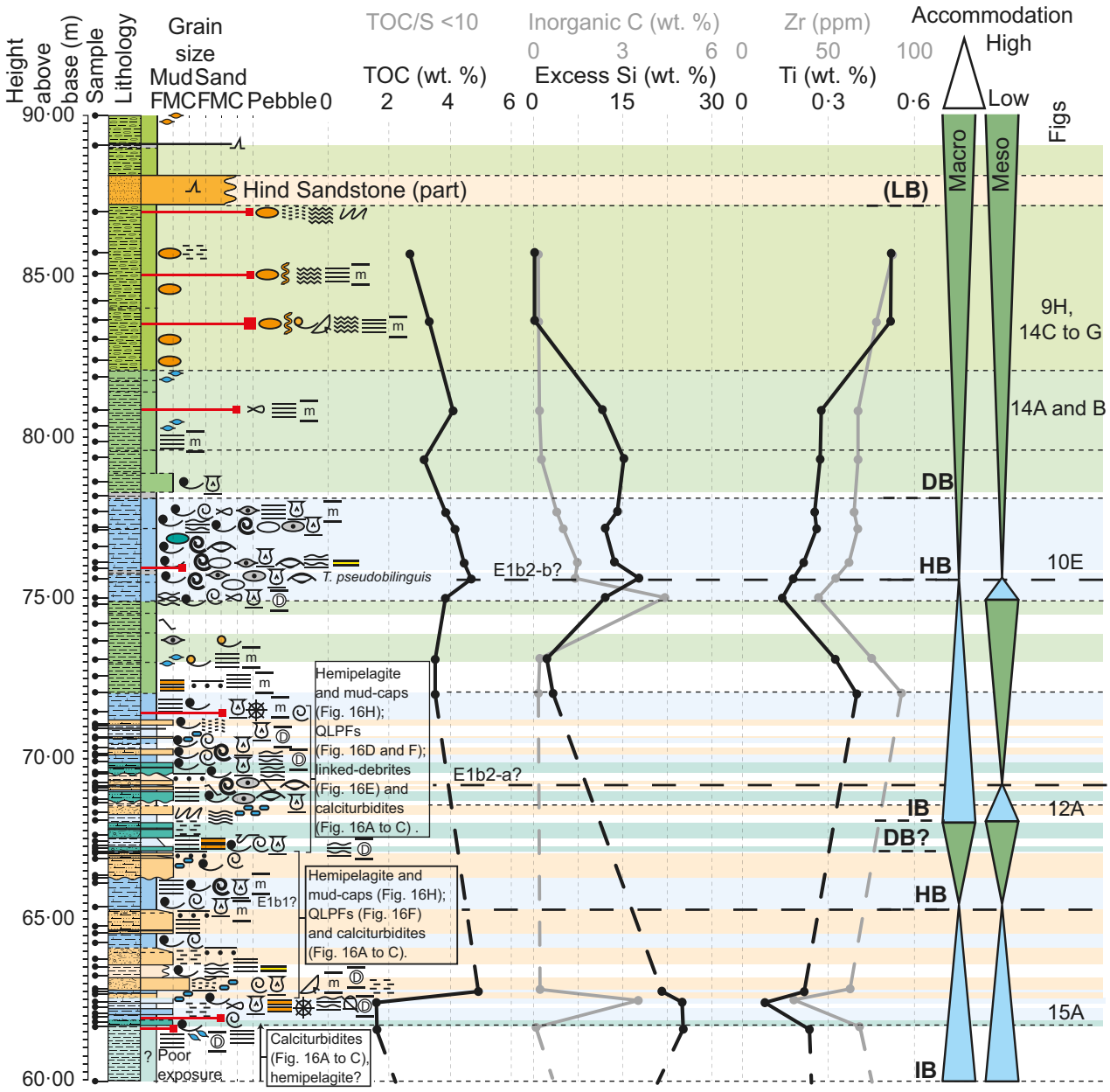

Fig. 6. Sedimentary log spanning the probable E_{1b1} to E_{1b2} biozones at Hind Clough. Hand specimen description based on Lazar *et al.* (2015). Biostratigraphy from Brandon *et al.* (1998). See *Materials and methods* for a description of methods, including sedimentary classification scheme and derivation of excess Si. Approximate mud lens (intraclast) diameter (Ø) and abundance estimated for thin sectioned samples only. HB = high basin accommodation; DB = decreasing basin accommodation, LB = low basin accommodation, IB = increasing basin accommodation. QLPF = Quasi-Laminar Plug Flow. See *Discussion* for further details; Fig. 3 for lithofacies descriptions based on composition and Fig. 4 for legend.

Fig. 7. Sedimentary log through the Upper Bowland Shale in borehole Cominco S9 (spanning probable E_{1b2} to E_{1c} biozone). Hand specimen description based on Lazar *et al.* (2015). Biostratigraphy from Arthurton (1972). See *Materials and methods* for a description of methods, including sedimentary classification scheme and derivation of excess Si. Approximate mud lens (intraclast) diameter (Ø) and abundance estimated for thin sectioned samples only. HB = high basin accommodation, DB = decreasing basin accommodation, LB = low basin accommodation, IB = increasing basin accommodation. See *Discussion* for further details; Fig. 3 for lithofacies descriptions based on composition and Fig. 4 for legend.

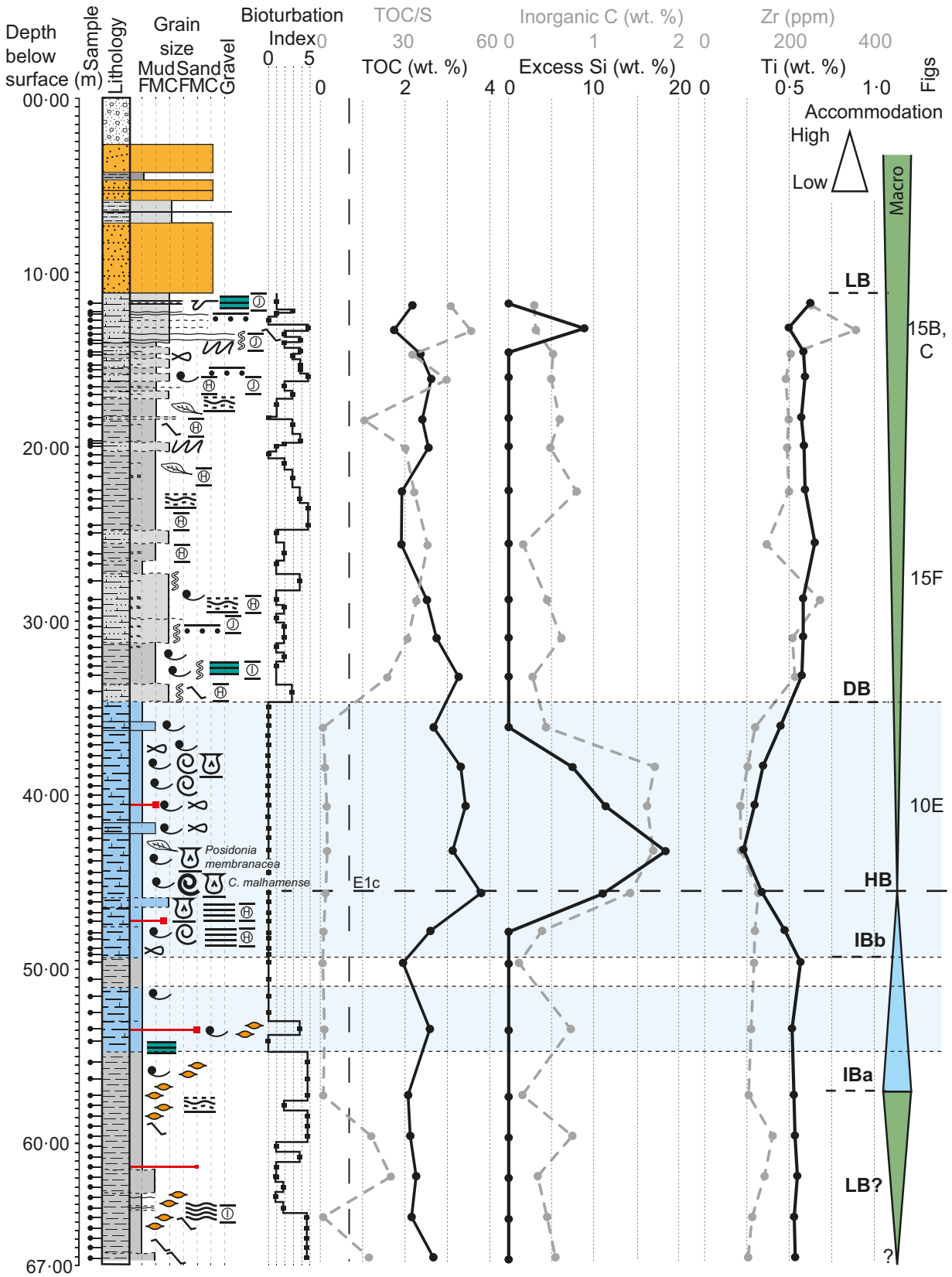

Table 1. Description and interpretation of sedimentary Facies A to J.

Facies description		Bed and lamina structure	Interpretation
A	Spherulitic limestone where calcite spherules comprise >90% of the bulk composition	Well-bedded; massive; bed thickness: 3 mm to 0·3 m; bed contacts: slightly diffuse, wavy; discontinuous, wavy, parallel organic and clay-rich laminae (several millimetres to centimetres long). Not bioturbated	Possible high porewater alkalinity and cation supersaturation near seabed (Braissant *et al.*, 2003; Mercedes-Martín *et al.*, 2016)
B	Weakly to moderately carbonate-bearing, moderately siliceous, weakly to moderately lenticular medium to coarse argillaceous [sandy] mudstone [to sandstone], with abundant calcareous bioclasts	Poorly to well-bedded; bed thickness: 0·2 to 0·5 m; bed contacts: typically diffuse, planar and parallel; rarely to moderately commonly laminated; laminae are typically 1 mm thick with sharp, planar to slightly wavy and parallel contacts, and lack internal structure ('mud-caps'); thin interbeds Facies D are moderately common; rare sulphate-bearing laminae. Not bioturbated	Pelagic and hemipelagic sediments deposited during periods of increasing and high accommodation anoxic/euxinic bottom waters, interbedded with small density flow deposits; (calci)turbidites shed from adjacent carbonate-rich highs; dissolution of carbonate in Facies C near seabed; anoxic bottom waters likely
C	Facies B (see above) without bioclasts		
D	Moderately to strongly carbonate-bearing, moderately siliceous to siliceous, commonly argillaceous, coarse mudstone [to sandstone]	Facies D: Well-bedded; bed thickness: 0·01 to 1·0 m; basal bedding contacts are typically sharp, wavy to planar and parallel; wavy parallel-laminated, coarse mud to fine-sand sized grains at base overlain by coarse to fine mud-sized 'mud-cap'. Facies E: Typically chaotic, contorted and deformed basal zone; laminae comprise coarse mud to fine sand-sized grains and gravel-sized mudstone, carbonate and silica cemented clasts, overlain by high-angle discontinuous curved cross-laminae and with organic matter fragments, overlain by coarse to fine mud-sized 'mud-cap'; upper bedding contacts (Facies D and E) may be sharp or diffuse; rare pyritic laminae and sulphate-bearing laminae (Facies D and E). Possible water escape structures or bioturbation towards the top of beds (Facies E only)	Deposition from low density turbidity currents, anoxic bottom water conditions likely
E	Weakly to moderately carbonate-bearing, moderately siliceous argillaceous coarse [sandy] mudstone [to sandstone]		Hybrid flows deposition during periods of low basin accommodation, intermittent bottom water anoxia likely
F	Moderately to strongly lenticular weakly siliceous to siliceous argillaceous mudstone [sandy mudstone to sandstone], rarely weakly carbonate-bearing	Highly fissile when weathered (obscures bedding structure); where observed, bedding contacts are typically diffuse; bed thickness: 0·2 to 3·5 m; moderately laminated; laminae are typically 1 mm thick with sharp, planar to slightly wavy and parallel contacts, and lack internal structure ('mud caps'); relatively homogenous (lenticular) sedimentary fabric; including pyritic laminae, sulphate-bearing laminae (relatively common); thin beds of Facies D are moderately common	Mixed density flow and hemipelagic deposits, during periods of moderate basin accommodation, mud clasts sourced from upslope scour by tidal and/or wind shear and delivered via bedload currents, anoxic bottom waters likely
G	Organic-laminated strongly lenticular argillaceous mudstone [medium sandstone to fine conglomerate]	Bedding obscured by weathering (highly fissile); many discontinuous to discontinuous, anastomosing, wavy to planar-parallel organic-rich laminae; laminae are 0·5 to 1·0 mm thick and lack internal structure ('mud caps') with composition similar to the bulk matrix; bioturbated (pyritized burrows)	Mixed density flow and hemipelagic deposits, possibly colonized by benthic microbial mats, oxic/dysoxic bottom water conditions likely
H I	Weakly carbonate-bearing argillaceous fine mudstone (Facies H), and coarse mudstone to medium sandstone (Facies I), both commonly micaceous	Weakly to well-bedded; bed thickness: *ca* 0·01 to 0·5 m; bed contacts: sharp, erosive bases and diffuse tops where texture is normally-graded, ranging from sand and coarse to fine mud-sized grains; sand-filled scours (Facies I); texture is otherwise typically homogenous; Facies H and I are typically interbedded; Facies H is also interbedded with Facies G; laminae are commonly wavy to planar and parallel; rarely to extensively bioturbated	Deposition from low to high density turbidity currents, hyperpycnal flows, reworking by storms (tempestites), oxic and dominantly freshwater conditions likely
J	Sandstones	Fine to coarse feldspathic quartz sand injected into Facies F and G mudstones	Toe of slope turbidite fan, injectite

Facies descriptions based on composition and texture. Grain size, including mud lenses, is denoted by square brackets [. . .] (*sensu.* Lazar *et al.*, 2015).

weathered slope, located on the edge of the Ribblesdale Fold Belt (Fig. 2B). This is a set of north-east/south-west trending folds, thrust folds and monoclines that developed during Variscan inversion of the basin (Arthurton, 1984). True thicknesses were estimated using the dip and strike of bedding with an Abney level. Sampling was primarily conducted directly within the stream section, in order to minimize the effect of chemical weathering, as described by Emmings *et al.* (2017c). Where stream sections were poorly exposed, logging and sampling was conducted on the adjacent slope. Samples were screened for alteration using visual assessment and site-specific geochemical proxies for weathering, including cross-plots of Cs/Cu and oxygen index used as a local weathering proxy (Emmings *et al.*, 2017c). 'Unaltered' samples are defined with respect to the sedimentological and geochemical analyses applied in this study.

Field/borehole and sample descriptions, including estimates for grain size, composition and bioturbation index, was based on the Lazar *et al.* (2015) method. This included generation of a ternary compositional plot (Appendix S1). Several facies are 'lenticular'; this is defined as a mud lens-rich (intraclastic) texture within an argillaceous clay-sized matrix. Thus, in terms of *grain size* (*sensu* Lazar *et al.*, 2015), several facies are described as 'sandy' mudstones to 'sandstones'. In terms of *composition*, these facies are primarily 'argillaceous mudstones'. Additional thresholds of 'weakly' and 'moderately' used to indicate mud lenses, carbonate and/or quartz abundances of >2·5% and >10% of the bulk composition, respectively. 'Strongly' is used to indicate mud lens abundance of >50% of the bulk composition.

Sedimentary facies were defined at the bed scale, typically millimetres to centimetres in thickness. 'Mud-cap' laminae are defined as mud-rich layers, typically microns to millimetres-thick, which lack internal structure and exhibit uniform composition and texture. Strata between successive marine bands are not necessarily genetically linked (Hampson *et al.*, 1997) and were also subject to local factors such as differential subsidence and changing sediment supply rate (Holdsworth & Collinson, 1988; Galloway, 1989). The bases of marine bands are the most prominent and laterally widespread surfaces, whereas erosion surfaces are laterally discontinuous and may be poorly defined in basinal settings. Therefore, packages are interpreted in terms of changing basin accommodation rather than strictly within a sequence stratigraphic framework (e.g. Posamentier *et al.*, 1988). Sedimentary packages are defined on the basis of increasing, high, decreasing and low basin accommodation (IB, HB, DB and LB, respectively). These stacking patterns may equate to transgressive, highstand, falling stage and lowstand systems tracts of Posamentier *et al.* (1988), respectively.

One hundred and ten samples were selected for geochemical analysis (including nine unaltered samples described by Emmings *et al.*, 2017c), with 37 subsamples thin sectioned. Thus, the confidence of grain-size estimates is robust for samples calibrated with thin sections. Samples were selected in order to attain appropriate temporal and spatial coverage across all sedimentary facies. Whole rock powder X-ray diffraction (XRD) data were collected on a Bruker D8 Advance Powder Diffractometer equipped with a LynxEye Position Sensitive Detector (Bruker, Billerica, MA, USA) with a Bragg Brentano, flat plate θ-θ geometry using CuKα radiation (see Appendix S1 for data example). Scanning electron microscopy (SEM) was conducted on uncoated ultrathin sections using an S-3600N Hitachi microscope (Hitachi, Tokyo, Japan) with an Oxford INCA 350 energy dispersive spectrometer (EDS) (Oxford Instruments, Abingdon, UK). Electron microphotographs were acquired using backscattered electrons (BSE). False colour composite images were compiled using Fiji (ImageJ) software and are overlain on each corresponding BSE microphotograph. Element maps (using SEM–EDS) were mapped to red (R), green (G) or blue (B) channels. Total sulphur (S) was determined using a LECO CS 230 elemental analyzer (LECO Corporation, St. Joseph, MI, USA). X-ray fluorescence (XRF) data were acquired on fused beads (109 samples) and powder briquettes (108 samples) with a PANalytical Axios Advanced XRF spectrometer using default PANalytical SuperQ conditions (Malvern PANalytical, Malvern, UK). Pyrolysis was conducted using a Rock-Eval 6™ apparatus (Vinci Technologies, Nanterre, France) at the British Geological Survey.

Titanium and zirconium are utilized as proxies for the detrital fraction, particularly heavy minerals (Hild & Brumsack, 1998). 'Excess silica' is defined as: $Si_{excess} = Si_{total} - (2{\cdot}5 \times Al_{total})$, *sensu* Sholkovitz & Price (1980), for samples where $Si_{total}/Al_{total} > 2{\cdot}5$ (i.e. *ca* 2·5 is the local detrital Si_{total}/Al_{total}, using Facies G to I). Excess silica is used as a proxy for the biogenic

(radiolarian) Si pool. Siliceous mudstones are silica-rich and contain abundant authigenic quartz cements. Siliciclastic mudstones contain quartz that is considered to be dominantly detrital rather than authigenic in origin. A full description of methods is provided in Appendix S2. Data are available via open access (Emmings *et al.*, 2017a,b).

RESULTS

Sedimentary logs for each basin position indicate that the Bowland Shale comprises limestone, and carbonate-bearing, siliceous and argillaceous mudstones (on the basis of composition; Figs 3 to 7; Appendix S1). Ten sedimentary facies (A to J; Table 1) were defined using observations at field/core-scale through to scanning electron microscopy (Figs 8 to 15). Facies A to J are classified and ordered along a spectrum of decreasing carbonate and/or biogenic silica, and increasing siliciclastic content (Table 1; Fig. 3). Facies A to F lack bioturbation (bioturbation index = 0; based on Lazar *et al.*, 2015). Facies A limestone is the carbonate end-member. Facies B and C are lenticular mudstones with an increasingly diminished carbonate component and moderate to high Si excess. Facies D and E exhibit highly variable, but typically low, carbonate content and moderate to high Si excess. Facies D deposits are typically well-bedded, well-sorted and moderately to highly carbonate-bearing. Facies E deposits are typically chaotic, poorly sorted and weakly carbonate-bearing. Facies F contains minimal carbonate and exhibits variable Si excess. Facies G lenticular mudstones contain trace carbonate and lack excess Si. Facies H to J represent the siliciclastic fine (H) to coarse (I) mudstone and sandstone (J) end-members. Figures 9 to 15 are ordered to match the Facies A to J spectrum.

Limestones

At outcrop, Facies A beds are competent and blocky, with slightly diffuse upper and lower contacts. Facies A comprises >90% calcite cement (Figs 4, 5 and 9A) present as discrete, poorly developed spherules, and is therefore defined as spherulitic limestone (Table 1). Calcite spherules are commonly fan-shaped and slightly elongate, and may radiate from a central nucleus, with individual spherule diameters (Ø) between 50 μm and 200 μm (Fig. 9A). Spherule long axes are typically perpendicular to discontinuous, wavy parallel organic-rich laminae. Widely spaced, sub-vertical wavy calcite veins (*ca* 10 to 20 μm thick) cross-cut calcite spherules and laminae. Extinction of each spherule under cross-polarized light is uniform. Facies A is interbedded with Facies B and C (Figs 4 and 5). Facies A samples exhibit very low total organic carbon (TOC), low silica excess, very high inorganic C and low Ti and Zr content (Fig. 4).

Carbonate-bearing and siliceous mudstones

Facies B and C are blocky to flaggy at outcrop (Fig. 8A), where moderately cemented beds are readily distinguished due to greater resistance to modern weathering (Fig. 8B and C). Facies B (Figs 10A to F and 11A) and C (Fig. 11A to F) exhibit a homogenous (Fig. 10C and D) and rarely deformed (Figs 10E and 11A) sedimentary fabric at the centimetre-scale. Facies B and C are typically weakly to moderately lenticular (Table 1; Fig. 10C to E) at the micron-scale and are compositionally defined as weakly to moderately carbonate-bearing, moderately siliceous, argillaceous mudstones. Planar to slightly wavy, parallel, homogenous laminae comprising fine mud-sized grains (dominantly clay; 'mud-caps') are rare to moderately common in Facies B and

Fig. 8. Field photographs from Hind Clough. (A) Plan-view of a mixed carbonate-phosphate lens or replaced bioclast (black arrow), 0·68 m above base, P2c biozone, Lower Bowland Shale. (B) Contrasting responses to weathering (competent and fissile) demonstrate interbedded carbonate-cemented (strataform dolomite) and poorly cemented lithologies from the E_{1a} marine band. (C) Despite compositions prone to weathering, stream sections expose unaltered material. The stream confluence (black arrow) was used as one of several anchor points during logging and sampling, at 32·0 m above base. (D) Erosional base (white arrows) to hybrid mass transport deposit (Facies E), E_{1a} biozone at 48·8 m above base. Sample 73A is from the underlying mudstone (mud-cap) and sample 75A is from the basal part of the bed. (E) Extensive slope exposure spanning the E_{1a} to probable E_{1b1} biozones. Relatively planar, laterally extensive hybrid mass transport deposits crop out across the slope. Sedimentary logs with interpreted basin accommodation are superimposed. Length of pen and hammer are 0·15 m and 0·30 m, respectively. The true vertical thickness of the visible outcrop section in (C) is *ca* 10 m.

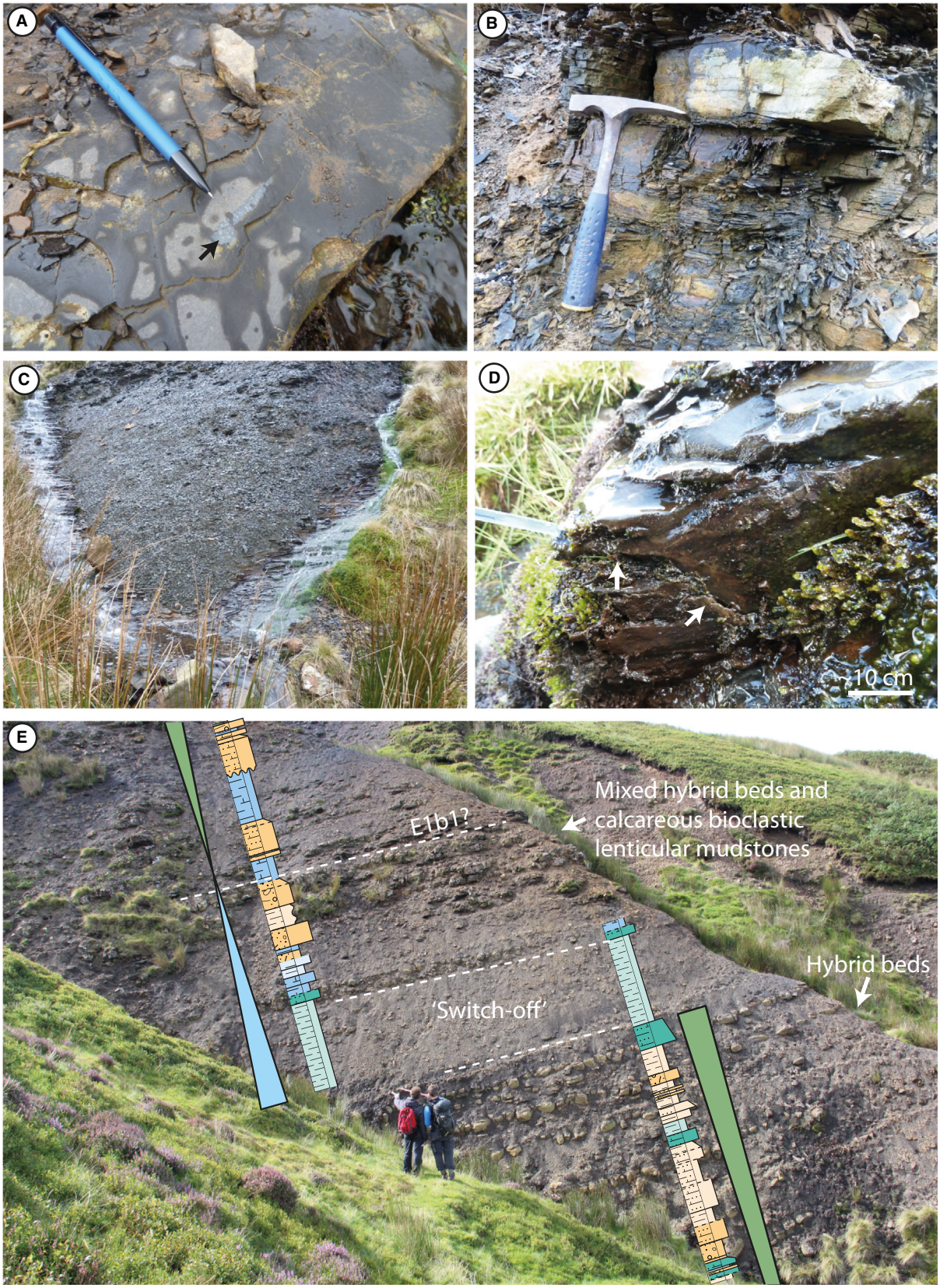

C (Fig. 10A and B). Carbonate, quartz and clays are present in approximately equal proportions (Appendix S1). Facies B and C samples typically exhibit moderate to high TOC, moderate to high silica excess, moderate inorganic C and low to moderate Ti and Zr content (Figs 4 to 7).

Quartz cement in Facies B and C (for example, Fig. 9B) is apparently widespread compared to detrital quartz grains. Bioclasts in Facies B include body fossils such as goniatites, trilobites, posidoniid bivalves, mollusc spat and fish debris (for example, Fig. 10F), and abundant mud to sand-sized shell fragments (for example, Fig. 10C). Bioclasts and shell fragments are often replaced and mantled by finely crystalline calcite cements (including scattered dolomite; Fig. 9C). Facies B also contains rare dispersed single calcite spherules (rounded, spherical, *ca* 30 μm *Ø*) with sweeping extinction. Phosphatic concretions and lenses in Facies B and C tend to exhibit a 'birds-eye' appearance (*sensu* Selley, 2000, after Illing, 1954) with long axis lengths ranging from 500 μm to several millimetres (Fig. 9D to F). Phosphatic concretions comprise amorphous organic matter (OM) and bioclasts (including abundant radiolarian tests) rafted in a mixed phosphate and calcite cement (Fig. 9F). Phosphatic lenses contain mud lenses (Fig. 11B). Facies B mudstones in the $E_{1b2\text{-}b}$ biozone also contain siderite nodules (typically 0·1 to 0·5 m *Ø*, which are spherical to sub-spherical; Fig. 6). Facies C lacks bioclasts but contains finely crystalline carbonate cement.

Facies D and E are blocky at outcrop, and where beds are sufficiently thick, these commonly form conspicuous beds on the slope (Fig. 8D and E). Facies D and E are moderately to strongly carbonate-bearing, and weakly to moderately carbonate-bearing, respectively. Both are typically moderately siliceous, argillaceous, coarse mudstones (i.e. equivalent to siltstones; Lazar *et al.*, 2015) and rarely sandstones (Table 1). Facies D is often wavy parallel-laminated towards the base of each bed and homogenous towards the top of each bed (Fig. 10G and H). Laminae often exhibit erosive bases and 'load and flame' contacts with the underlying mudstone (Figs 10G and 15A). Laminae comprise calcareous bioclastic fragments (typically coarse mud to fine sand-sized; <200 μm *Ø*), detrital quartz and are cemented with carbonate and silica (Fig. 10H). Rarely laminae are cemented with euhedral pyrite. Quartz, carbonate and clays in Facies D and E account for approximately >40%, <20% and <40% of the bulk composition, respectively. Facies D and E samples typically exhibit low to moderate TOC, high silica excess, variable inorganic C and moderate to high Zr and Ti content (Fig. 5).

Facies E typically exhibits chaotic textures towards the base of beds, including deformed laminae (Fig. 12A). Towards the top of each bed, Facies E exhibits homogenous 'starry-night' texture (i.e. 'mud-caps', *sensu* Fonnesu *et al.*, 2017) (Fig. 12B). The centre of Facies E beds exhibits high-angle discontinuous curved and climbing cross-laminae (Fig. 12C and D), frayed fragments of OM (Fig. 12D and E), and abundant gravel-sized carbonate and quartz cemented clasts and lenses (Fig. 12C to G). This sequence of textures is not always present in every bed. The carbonate and silica-cemented clasts and

Fig. 9. Examples of diagenetic textures, including spherulitic limestones (Facies A), carbonate-bearing, siliceous mudstones (Facies B) and booky kaolinite (Facies F to G). (A) XPL (cross-polarized) microphotograph, Facies A, HB package, Sample SSK60776, 13·44 m below surface, MHD4. Spherules are fan-shaped (see inset) and often radiate from a central nucleus (thin white arrow). (B) and (C) Facies B, HB package, Sample 22A, 22·27 m above base. (B) Composite SEM–EDS element map. Macrocrystalline silica cements are readily distinguished from detrital quartz because the former typically exhibits an irregular morphology and commonly infills sheltered pores, such as inside a trilobite test. Note partially dissolved calcite in contact with subsequent silica cements. (C) Composite SEM–EDS element map. Skeletal debris are often recrystallized and mantled by calcite cements (red arrow) and scattered dolomite replacement of calcite [white arrows in (B) and (C)]. (D) to (F) Facies B. (D) Cut-sample microphotograph, sample SSK60782, E_{1a} marine band, 15·45 m below surface, with many early-cemented phosphate concretions (black arrows) and phosphatic lenses (white arrows). (E) and (F) Phosphate concretion, sample SSK60808, MHD4, 24·30 m below surface, HB package, microphotograph. (F) SEM–EDS composite element map within a concretion, comprising amorphous organic matter and bioclasts 'rafted' in a two-phase phosphate and calcite cement. Radiolarian tests (red arrow) are replaced by clays or preserved as organic linings. Presence of silica cement (white arrows) within this early-cemented phosphate concretion suggests biogenic silica was a source of Si for cements. (G) Facies F, sample DC11A, 33·40 m above base, E_{1a} biozone, DB package, with booky kaolinite fill inside organic matter (white arrow). (H) Facies G, sample 188, 83·60 m above base, DB package, booky kaolinite nodule with pyrite euhedra.

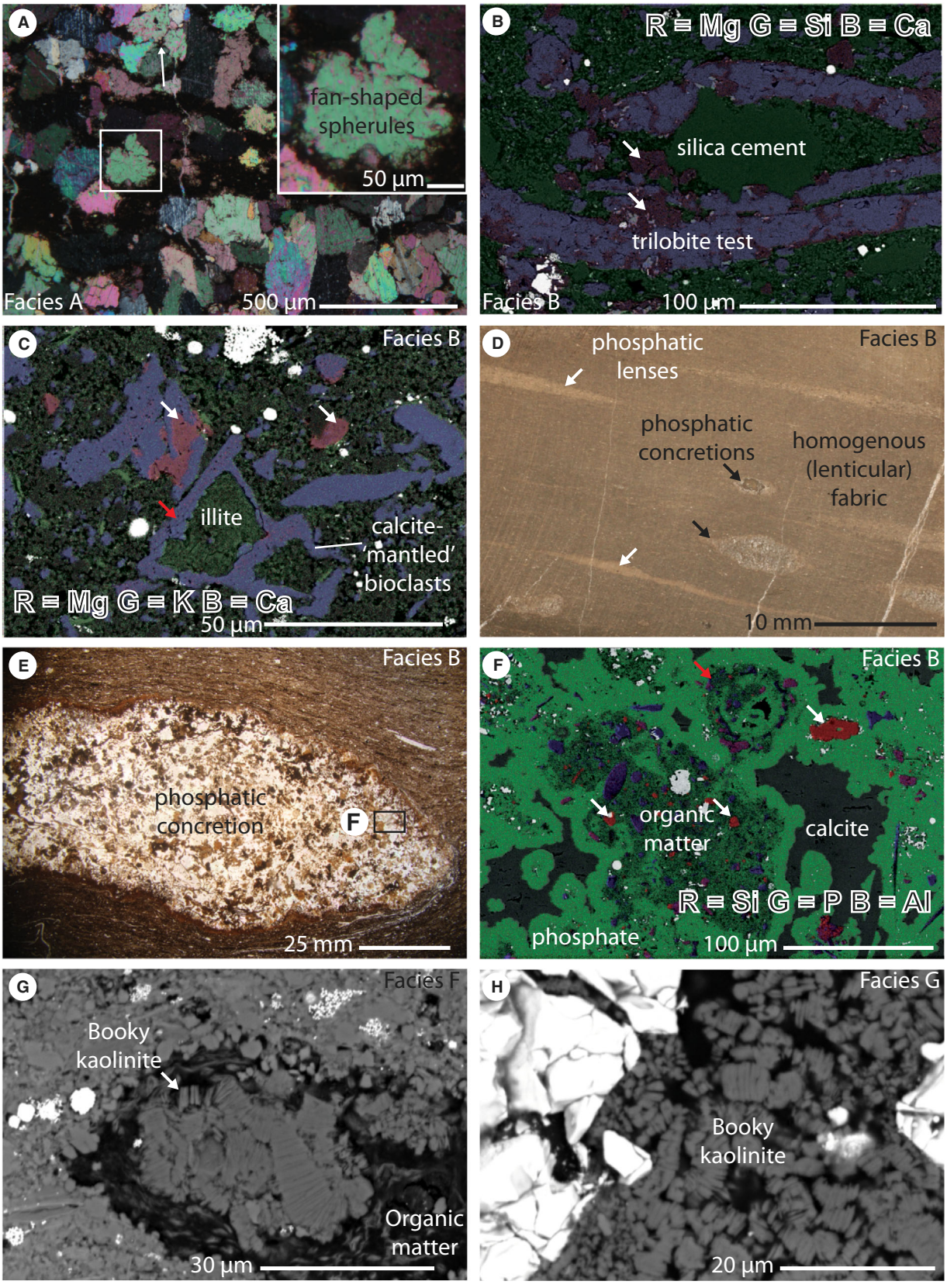

lenses are typically rounded and partially deformed (Fig. 12G), and are often concentrated at the base of each cross-lamina (for example, Fig. 12C). These clasts commonly contain sand-sized euhedral pyrite. Some clasts represent single bioclasts replaced by carbonate and silica cement. In plan-view, coarse mud-rich (silty) laminae are curved, and the carbonate and silica-cemented clasts and lenses are rounded, equant to elongate and aligned (Fig. 12F). These clasts occasionally exhibit tapered edges (Fig. 12G). Facies D and E are commonly interbedded with Facies B, C and F (Figs 5 and 6). Upper contacts of Facies D and E beds and solitary 'mud-cap' laminae are typically sharp (Figs 5, 6, 10A and 10B) and occasionally reworked (Fig. 15A). Facies D and E bed bases are typically sharp, planar to wavy (Figs 8D, 10G, 10H and 15A).

At outcrop, weathering of Facies F generates highly fissile 'paper shale' in slope sections (Fig. 8C), so that individual beds are difficult to recognize. At Hind Clough, shoaling of the inclination of bedding by *ca* 3° (Fig. 8D) coincides with similar inclination observed in hand specimen and thin section at the contact (Fig. 11C to E). Facies F is defined compositionally as weakly siliceous to siliceous argillaceous mudstone and is moderately to strongly lenticular (Table 1). Quartz and clay content is highly variable but typically <40% and >60% of the bulk composition, respectively. Facies F contains trace carbonate (Figs 5 and 6) and rarely contains carbonate, pyrite or silica-replaced bioclast casts or as moulds. Facies F samples typically exhibit moderate to high TOC, low to high silica excess, very low inorganic C and moderate to high Zr and Ti content (Figs 5 and 6). Facies F is rarely interbedded with Facies B to E. Planar to slightly wavy, parallel 'mud-cap' laminae are common in Facies F.

The clay to fine sand-sized 'matrix' of Facies B to F comprises framboidal pyrite (*ca* 5 μm Ø), rare pyrite euhedra and sphalerite, isolated and patchy macro-crystalline to micro-crystalline silica and/or calcite cement, abundant authigenic clay minerals (including illite and/or smectite–illite clays – Fig. 9C; and 'booky' kaolinite – Fig. 9G) and scattered dolomite that partially replaces calcite when present (Figs 9B to C and 12G). Unambiguous examples of detrital quartz in Facies B to F are rare and typically limited to Facies D basal laminae (Fig. 10A), although it is possible that the widespread silica cements (for example, Fig. 9B) are cored by detrital quartz (*sensu* Schieber *et al.*, 2000). The matrix of Facies F lacks carbonate and contains abundant isolated silica cement, authigenic feldspar and authigenic and detrital clay minerals (Fig. 13A to G). Deformed, wavy to crinkled micron-scale to millimetre-scale elongate to platy fragments of OM are common in Facies E and rare to common in Facies B to F (Figs 10C, 12D, 12F and 13D). Spherical (*ca* 20 to 30 μm Ø) particles of OM are also present in Facies B and C and common in Facies F (Fig. 13E). The OM pores in Facies B to F contain silica cement, scattered pyrite framboids and microcrysts (Fig. 13D and E) and locally 'books' of kaolinite in Facies F (Fig. 9G). Sulphate-bearing laminae in Facies F contain Ca-rich sulphate (anhydrite or gypsum) within OM pores (Fig. 11G) but otherwise the sedimentary matrix is similar to the bulk.

Fig. 10. Carbonate-bearing, siliceous mudstones, including Facies B weakly to moderately lenticular mudstones and well-bedded Facies D. (A) to (F) Facies B. (A) LB package, sample SSK60797, 19·80 m below surface, thin section scan, including planar to wavy parallel laminae (mud caps). (B) DB package, sample SSK60804, 22·35 m below surface, thin section scan, including planar parallel laminae (mud caps). (C) HB package, sample 21A, 22·02 m above base, including fragments of organic matter (white arrow), coarse mud-sized to sand-sized bioclasts (partially replaced by calcite) and mud lenses (black arrows). (D) LB package, sample SSK60794, 18·97 m below surface, including relatively large sand-sized mud lenses (white arrow) and few sand-sized calcareous bioclasts (red arrow). Inset = E_{1c1} marine band, HB package, sample SSK61404, 40·72 m below surface, Cominco S9, including small bioclasts (red arrow), fragments of organic matter and fine lenticular texture. (E) HB package, sample 174A, 76·10 m above base, Hind Clough, including large bioclast (white arrow) with soft-sediment deformation textures (black arrow). (F) Sample SSK60812, 26·44 m below surface, P_{2c} biozone, cut-sample photograph, including relatively large trilobite test and phosphatic debris. (G) and (H) Facies D. (G) Sample 117A, Hind Clough, LB package, E_{1a} biozone, 59·37 m above base, cut-sample photograph, and sample 50A (inset), Hind Clough, 35·60 m above base. Laminae exhibit erosive bases (black arrow), 'load and flame' structures (inset, black arrow) and are cemented by calcite. (H) Sample 02A, 0·68 m above base, IB(?) package beneath E_{1a}, P_{2c}(?) biozone. Basal wavy-parallel laminae (white arrows) comprise sand-sized calcareous bioclasts and detrital quartz grains cemented by carbonate and silica and are overlain by homogenous mud.

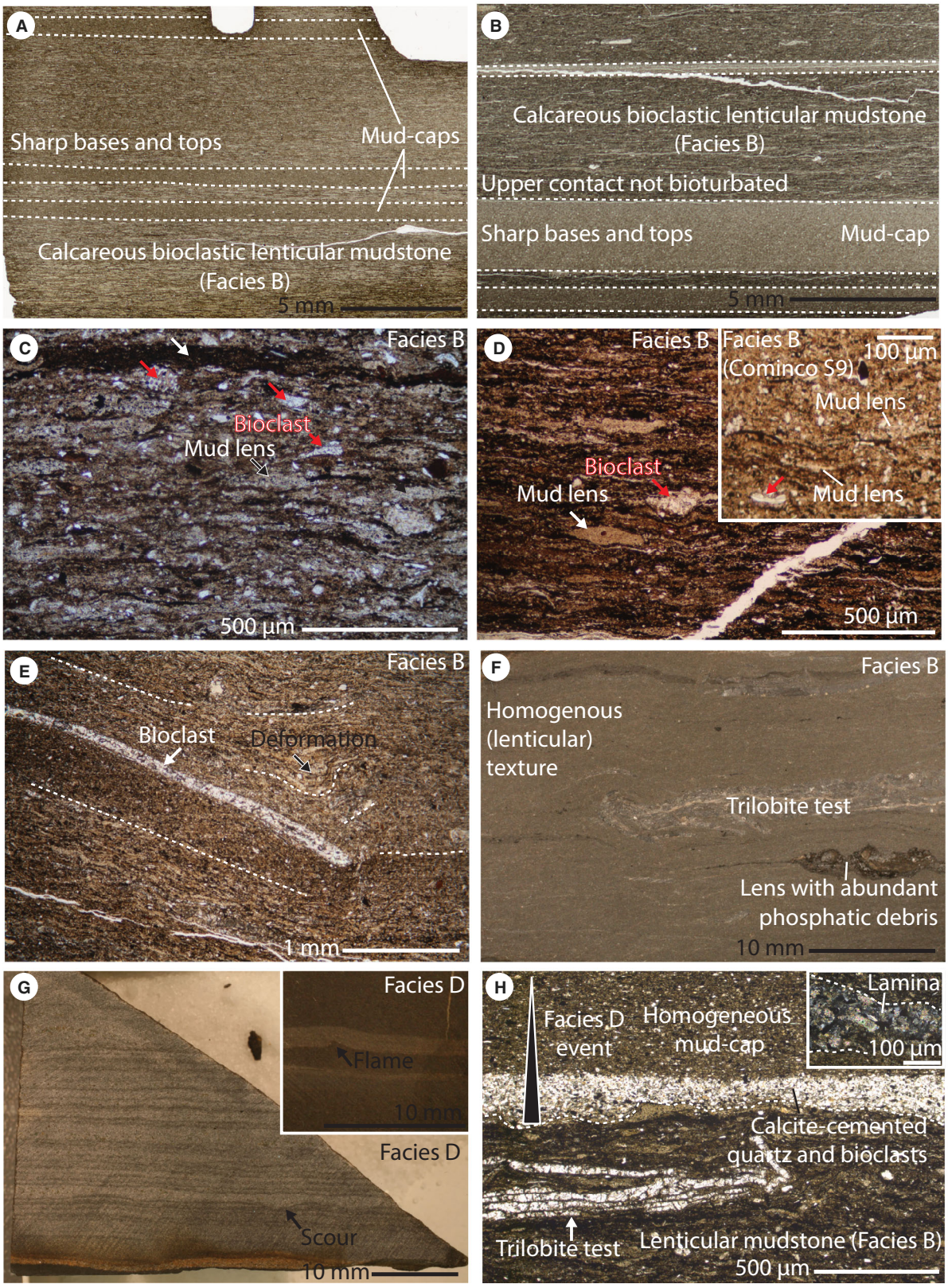

Siliciclastic mudstones

Facies G is defined compositionally as argillaceous mudstone and is strongly lenticular (Table 1; Fig. 14A to F). Facies G also contains organic-rich laminae and a matrix of authigenic and detrital clay minerals (Fig. 14C to G; including authigenic 'booky' kaolinite – Fig. 9H), pyrite euhedra and nodules (0·5 to 20 mm *Ø*, rounded, spherical; Fig. 9H) and detrital quartz. Facies G is typically laminated with homogenous 'mud-caps' (for example, Fig. 14C). The Facies G bulk sediment comprises approximately 90% clays, 10% quartz and trace carbonate (Appendix S1). Facies G samples typically exhibit moderate TOC, very low inorganic C and high Ti and Zr content and lack excess silica (Fig. 6). Single pyritized burrows in Facies G (Fig. 14G) exhibit individual burrow *Ø* of *ca* 50 μm to 1 mm and burrow depth up to *ca* 2 mm (bioturbation index = 1; Lazar *et al.*, 2015).

Facies H and I appear homogenous or exhibit normal grading with sharp bases (Fig. 15B) and are argillaceous fine to coarse, sandy mudstones and medium sandstones (i.e. siltstones; Table 1), respectively. Facies H is typically interbedded with Facies G (at Hind Clough). Facies H and I are also typically interbedded. Facies I also exhibits sand-filled scours along basal contacts (Fig. 15B) that are partially comparable to basal laminae in Facies D (Fig. 15A). The matrix of H and I comprises fine to coarse mud-sized detrital quartz, feldspar, chlorite, muscovite mica, other fine clay minerals (kaolinite, illite group), terrestrial OM and rare euhedral pyrite and is weakly siderite-cemented (Fig. 15C). Micas, clays and heavy minerals typically account for >60% of the bulk composition, with subordinate detrital quartz. Facies H and I also occasionally contain organic-rich laminae comparable to Facies G (Fig. 15E and F). Facies H and I exhibit low to moderate TOC, low inorganic C and high Ti and Zr content (Fig. 7) and lack excess Si.

In Cominco S9, Facies H and I are typically bioturbated, including 'mantle and swirl' textures (Lobza & Schieber, 1999) (Fig. 15F), although well-defined burrows are rare (spanning bioturbation indices 0 to 5 of Lazar *et al.*, 2015). Facies H and I at Cominco S9 exhibit TOC/S > 10 (Fig. 7) whereas all other facies exhibit TOC/S *ca* 1·2. Facies J defines all sandstones, including the Hind Sandstone injectite at Hind Clough (Fig. 15D; Kane, 2010) and the overlying Pendleton Formation (Waters *et al.*, 2009).

Lenticular fabrics and grain size

Mud lenses in Facies B, C and F typically lack the pyrite framboids and OM that are present in the matrix, and comprise abundant kaolinite and subordinate illite, mica, quartz and feldspar (for example, Fig. 13B to F). Mud lenses in Facies G also lack OM that is present in the matrix. Mud lenses in Facies B, C, F and G are flattened in bedding-perpendicular sections (Figs 10C to E, 11B, 13A, 13B, 13G, 14A and C to E) and equant and rounded in phosphatic lenses (Fig. 11F) and in plan-view (Figs 11F, 13H, 14B and 14F). Lenses also rarely exhibit imbrication and deformation textures (Fig. 13A). An early phosphate cement preserves mud lenses with pre-compaction geometry (Figs 11B and F) and suggests that the compacted thickness is *ca* 45% of the original thickness. Facies B and C mud lenses are rare to moderately common and exhibit 50 to 300 μm *Ø* (i.e. coarse mud to medium sand-sized; Figs 10C to E and 13H). Therefore, on the basis of grain size, moderately lenticular Facies B and C are medium to coarse sandy mudstones and sandstones. In

Fig. 11. Facies B and C highly to weakly carbonate-bearing, siliceous, weakly to moderately lenticular mudstones. (A) Facies B, sample 13A, 11·60 m above base, microphotograph including dewatering structure (arrow). (B) Facies C, sample 31A, 25·52 m above base, HB package. An early phosphate cement preserves mud lenses (examples: arrows) with pre-compaction geometry. Comparison of cemented and compacted geometries (examples: arrows) indicates that the compacted thickness is *ca* 45% of the original thickness. (C) to (E) Facies C. Bed dip shoals across the contact in sample 35A, 27·80 m above base. (C) Thin section scan, image rotated so that the base is horizontal. Microphotographs demonstrate the inclined lenticular fabric (D) is *ca* 3°, or a pre-compaction palaeoslope gradient of *ca* 7°, steeper than the horizontal fabric (E). (F) An early phosphate cement preserves mud lenses (examples: arrows) with pre-compaction geometry. Cemented mud lenses exhibit comparable shape to compacted lenses in plan-view (inset). See also (B). (G) Facies F. Moderately lenticular mudstone with sulphate-bearing lamina, sample DC11A, 33·4 m above base, DB package, optical and BSE microphotographs. Ca-sulphate crysts are present within organic pores (white arrows). Note also presence of pyrite euhedra and framboids in the adjacent lamina matrix (red arrow).

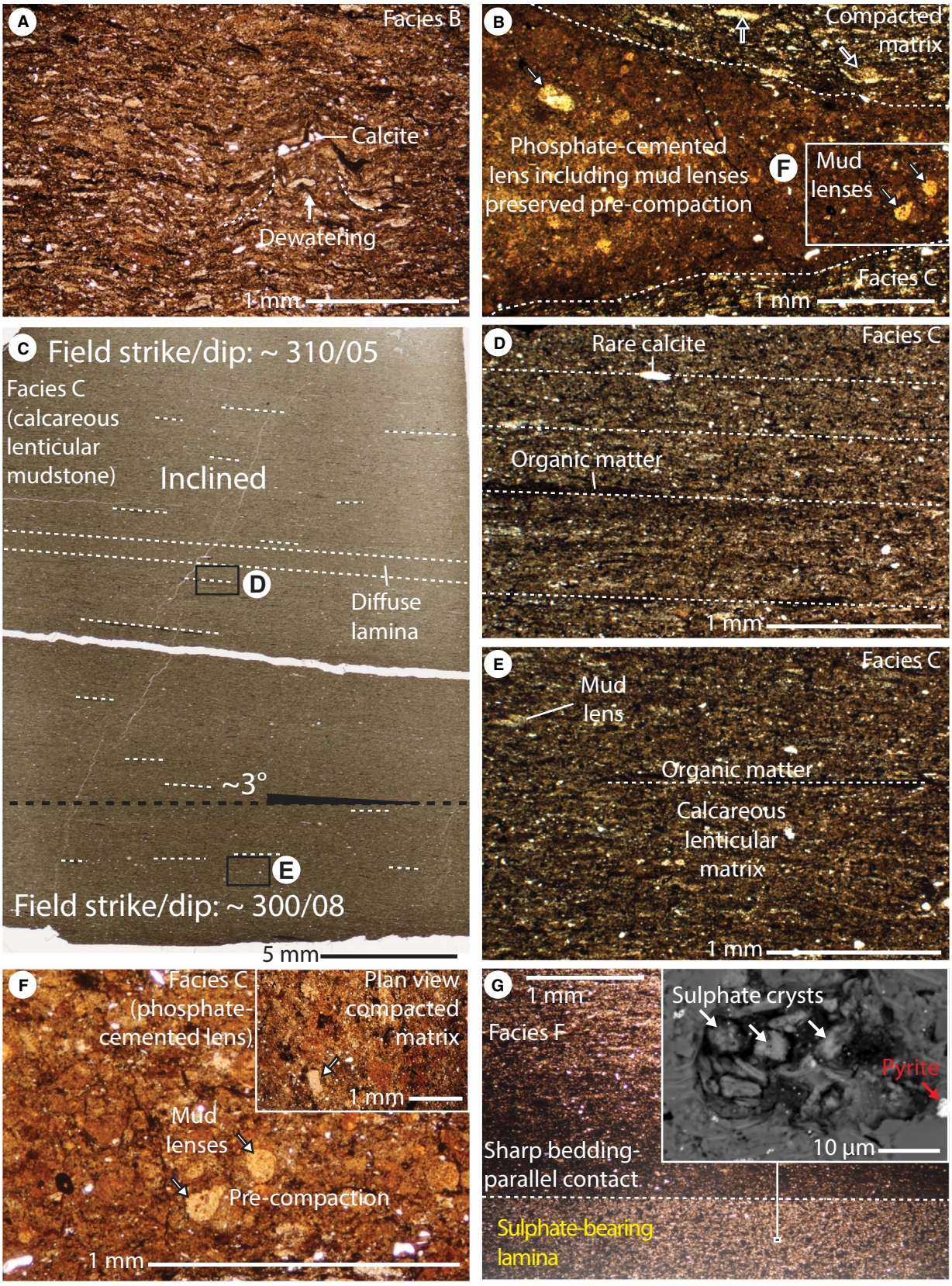

Facies F, mud lenses are 50 to 500 μm Ø (coarse mud to coarse sand-sized) and moderately common to abundant (Figs 13A, 13B, 13G, 14A and 14B). Thus, on the basis of grain size, Facies F is defined as sandy mudstone to sandstone. Lenses in Facies G are 0·5 to 4·0 mm Ø (medium sand to pebble-sized; Fig. 14C to F). Therefore, on the basis of grain size, Facies G is defined as medium sandstone to fine conglomerate. The size and abundance of lenses in Facies F typically increase with height towards the base of Facies G at Hind Clough (for example, Figs 5 and 6; compare Figs 13A, 14A and 14B). 'Composite' lenses, comprising multiple smaller lenses, are present within Facies F directly beneath Facies G at Hind Clough (Fig. 14B).

Sedimentary packages and geochemistry

The abundance of detrital elements (for example, Ti and Zr) strongly declines, whereas TOC, carbonate content and excess silica content increase, through each increasing basin accommodation (IB) package (Figs 4 to 7). In Cominco S9 a lower package (IBa) delineates onset of TOC/S < 10 (Fig. 7). An upper package (IBb) defines the increase in TOC, carbonate and excess silica content (Fig. 7). High basin accommodation (HB) packages exhibit initially relatively high TOC, carbonate and excess silica content that gradually decrease towards the top (Figs 4 to 7). Similarly, detrital elements gradually increase in abundance through each HB package. Decreasing basin accommodation (DB) packages generally exhibit stable TOC, decreasing or no excess silica content and increasing abundance of detrital elements towards the top of each package (Figs 4 to 7). Low basin accommodation (LB) packages tend to exhibit moderate to high detrital element content, whereas carbonate, TOC and excess silica content are highly variable (Figs 5 to 7).

DISCUSSION

Subaqueous sediment density flows

Facies D coarse mudstones (Figs 10G, 10H and 15A) are interpreted as mud-rich low density calciturbidites (Fig. 16A to C; defined by Stow & Shanmugam, 1980) that were in some cases reworked during deposition of overlying lenticular muds (Facies B, C or F). Basal sandy to coarse muddy wavy laminae (Fig. 10G and H) are interpreted as the T_D division of Bouma (1962) that grade into $T_{E\text{-}1}$ of Piper (1978). These laminae possibly formed via deposition of coarse mud in a turbulent boundary layer beneath a dilute suspension (Stow & Bowen, 1978) or in a shear zone beneath a relatively concentrated gelled fluid mud layer (McCave & Jones, 1988). The typically sharp grain-size break between $T_{E\text{-}1}$ and $T_{E\text{-}2}$ is a feature common to many mud-rich low density turbidites and likely relates to flow transition from non-cohesive to cohesive behaviour (Talling *et al.*, 2012). Massive to weakly graded fine mud-rich laminae and beds overlying Facies D coarse mudstones (Figs 10G, 10H and 15A) are interpreted as the $T_{E\text{-}2}$ and $T_{E\text{-}3}$ turbidite divisions of Piper (1978).

Homogenous 'mud-cap' laminae lack underlying coarse mud or sandy laminae so that turbulent, hybrid or laminar flows were all potentially viable depositional mechanisms (Fig. 16H). Facies B (Fig. 10A and B), Facies C (Fig. 11C), Facies F (Fig. 13A), Facies G (Fig. 14C), Facies H (Fig. 15E) and Facies I (Fig. 15F) all include examples of these 'mud-cap' laminae. A lack of intraclasts observed within the 'mud caps' suggests that these deposits did not form via reworking of flocs as bedload on the lee face of ripples beneath relatively fast flows (Schieber *et al.*, 2007a; Talling *et al.*, 2012).

A variety of sedimentary structures suggest that Facies E beds were deposited by hybrid

Fig. 12. Facies E chaotic, weakly carbonate-bearing, siliceous mudstones. (A) Sample 147, E_{1b1}(?) zone, 68·32 m above base, IB package debrite, cut-sample photograph, including contorted basal shear zone overlain by mud containing many cemented and fluidized bioclastic coarse mud-rich chaotica (water escape) and/or bioturbation (black arrow). (B) Sample 73A, E_{1a} zone, LB package, 'starry-night' turbidite mud-cap, 48·14 m above base, microphotograph. (C) to (F) Sample 75A, E_{1a} zone, 48·82 m above base, LB package. (C) Cut sample photograph. (D) Thin section scan with climbing ripples and truncated cross-laminae, and (E) microphotograph, including mud-rich microbial mat rip-up clast (inset). (F) Plan-view equivalent of (D), with many aligned discontinuous laminae and lenses of calcite and silica-replaced bioclasts and fragments of organic matter. Truncated surfaces are curved in plan-view, whereas cross-laminae are linear. (G) Sample 89A, 52·17 m above base, E_{1a} biozone, cross-laminated mudstone with many calcite and silica cemented lenses and fragments of organic matter. Lenses exhibit rounded edges, tapered geometry and partial fragmentation (inset, cross-polarized light).

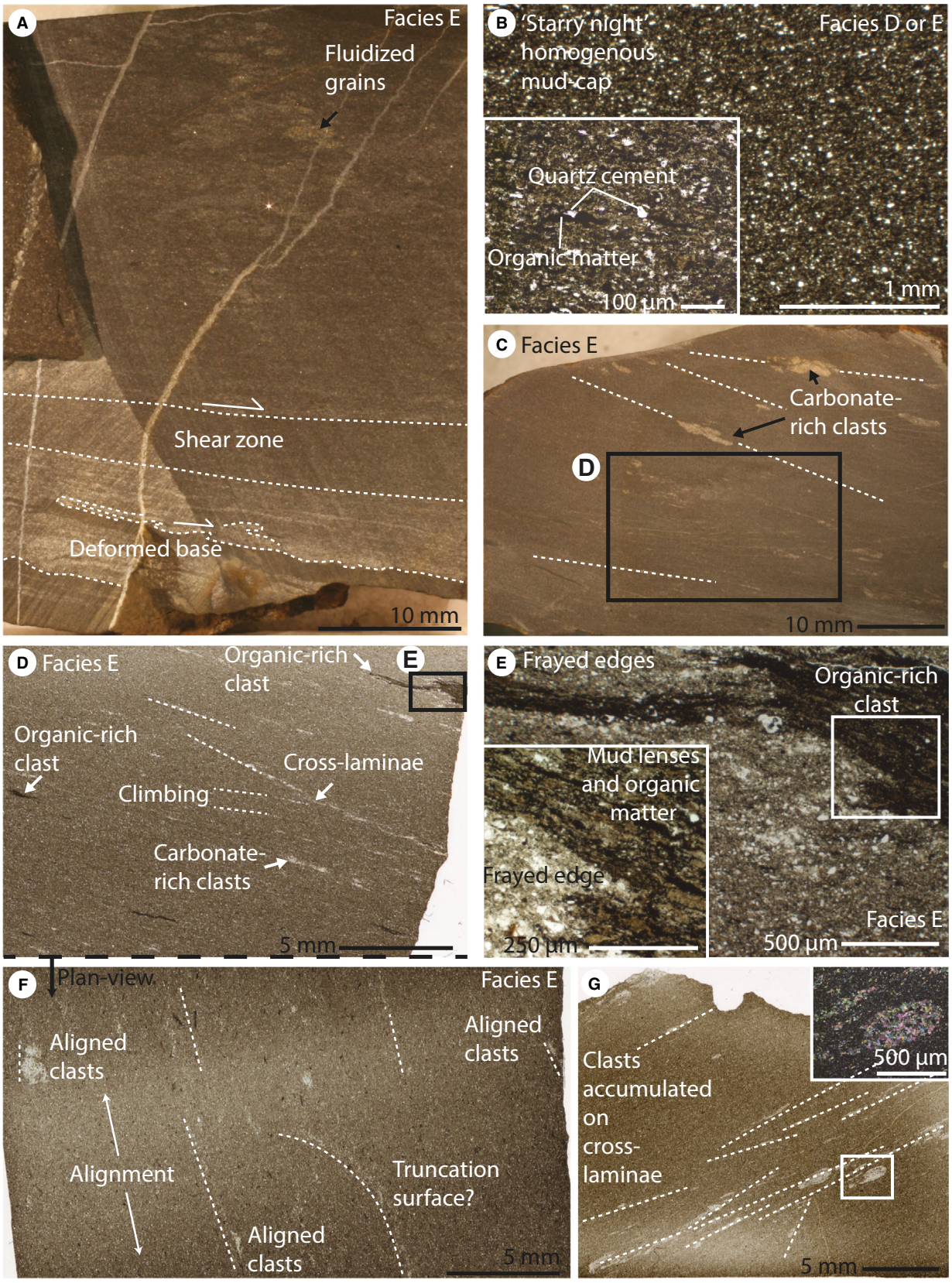

flows, with turbulent and laminar components (Figs 12A to G and 16D to G; defined by Haughton *et al.*, 2009). Facies E beds undergo a distinctive transition through the section at Hind Clough. The lowest Facies E beds at Hind Clough exhibit sharp, planar basal contacts and are homogenous or occasionally weakly graded (Fig. 5) and are therefore interpreted as the deposits from mud-rich turbidity currents (Talling *et al.*, 2012). Above these mud-rich turbidites, Facies E beds exhibit the greatest diversity of sedimentary structures (Figs 8D and 12A to F) that compare best to sediment deposition from 'lower transitional plug flows' (Fig. 16G), characterized by moderate clay concentration and extensive top-down reworking by long-lived post-deceleration steady flows (Baas *et al.*, 2009, 2011). The complete lack of any homogenous basal sand is interpreted as deep scour (for example, Fig. 8D) and complete reworking by the flow. Younger flows were apparently less erosive, because erosive bases, mud clasts and possible microbial mat fragments become increasingly rare (Fig. 5).

Hybrid beds gradually exhibit the characteristics of 'quasi-laminar plug flows' (Baas *et al.*, 2009, 2011). These beds are equivalent to the Type IV deposits of Sumner *et al.* (2009). Above the E_{1b1} marine band, hybrid beds are interpreted as a variety of 'quasi-laminar plug flows' (Fig. 16D), linked-debrites (Fig. 16E) and ungraded mud-caps interpreted as the $T_{E\text{-}3}$ divisions of Piper (1978). The high clay and organic content likely sufficiently damped flow turbulence in order to generate such hybrid beds (Baas *et al.*, 2011).

Facies I scours are filled with homogenous sand (Fig. 15B), indicative of a high density (and likely strongly bypassing) element of turbulent flow (T_A division) (Talling *et al.*, 2012). Sand to coarse mud-rich normally-graded beds in Facies H and I (Fig. 15E to F) are interpreted as the T_D to $T_{E\text{-}1}$ divisions of Piper (1978). Facies H and I muds overlying sand-filled scours (Fig. 15B) are interpreted as the T_D and/or $T_{E\text{-}1}$, $T_{E\text{-}2}$ and $T_{E\text{-}3}$ divisions. Given the thin bedded nature of these deposits, Facies I muds were likely deposited from dilute low density turbidity currents (Stow & Bowen, 1978).

Occasionally Facies H and I exhibit draped mudstone (T_E) and deformation of basal coarse mud (silty) laminae (Fig. 15E and F). These textures are comparable to deposits interpreted as tempestites (Schieber, 1986, 2016). Rare symmetrical coarse mud (silty) laminae in Facies I (Fig. 15E) suggests deposition from waxing and waning of hyperpycnal flows (Li *et al.*, 2015; Schieber, 2016). This is plausible given that a strong halocline probably existed at the basin margins, considering that Facies H and I at Cominco S9 were deposited under a freshwater column (Fig. 7; Berner & Raiswell, 1984).

Origin of mud lenses

Mud lenses in Facies B, C, F and G (Figs 10C, 10F, 11A to G, 13A to H and 14A to H) are interpreted as clasts that were transported as partially consolidated muds in the bedload of bottom currents (Schieber *et al.*, 2010). Rarity of pyrite framboids within partially consolidated clasts (Fig. 13C) suggests that the solutes required for pyrite precipitation were largely unavailable. A relatively low clast permeability compared to surrounding sediments potentially limited infiltration by syngenetic and/or diagenetic (sulphidic) pore-fluids. Figure 11F demonstrates that lenticular mudstones were clast-supported prior to compaction. A rip-up interpretation is supported by dominantly equant lens shape geometry in un-compacted (Fig. 11F) and plan-view (Figs 11F, 13H, 14B and 14F), increasing clast diameter and abundance

Fig. 13. Comparison of lenticular fabrics and organic matter, including Facies F moderately to strongly lenticular siliceous mudstones. (A) to (F) Facies F, sample DC01, 38·22 m above base, DB package, microphotographs (A) and (B) and BSE microphotographs (C) to (F). Mud lenses are present throughout – examples: white arrows in (A). The fine mud-rich, pyritic (dark) planar, parallel laminae contains few, relatively small lenses. Note also deformed lenses and multiple examples of imbricated lenses – red arrows in (A). BSE microphotograph lens and 'matrix' comparison. The sediment matrix (D) and (E) comprises pyrite framboids (pf), organic matter, macrocrystalline silica cement (si), illite laths (white arrows), and mixed fine clays and quartz. Organic matter exhibits two geometries; sheets (D) and equant particles (E). Mud lenses (F) contain illite laths (white arrows), mica, kaolinite (black arrow), feldspar (albite, with alteration rim) and fine quartz and kaolinite, and typically lack organic matter and pyrite. (G) Sample DC04, 37·37 m above base, DB package, microphotograph with strong lenticular texture (white arrows) and organic matter (red arrows). (H) Facies C, sample 31, 25·52 m above base, HB package, plan-view microphotograph, including organic matter (organominerallic aggregates; white arrow), mud lenses (black arrow) and carbonate and quartz grains (red arrow).

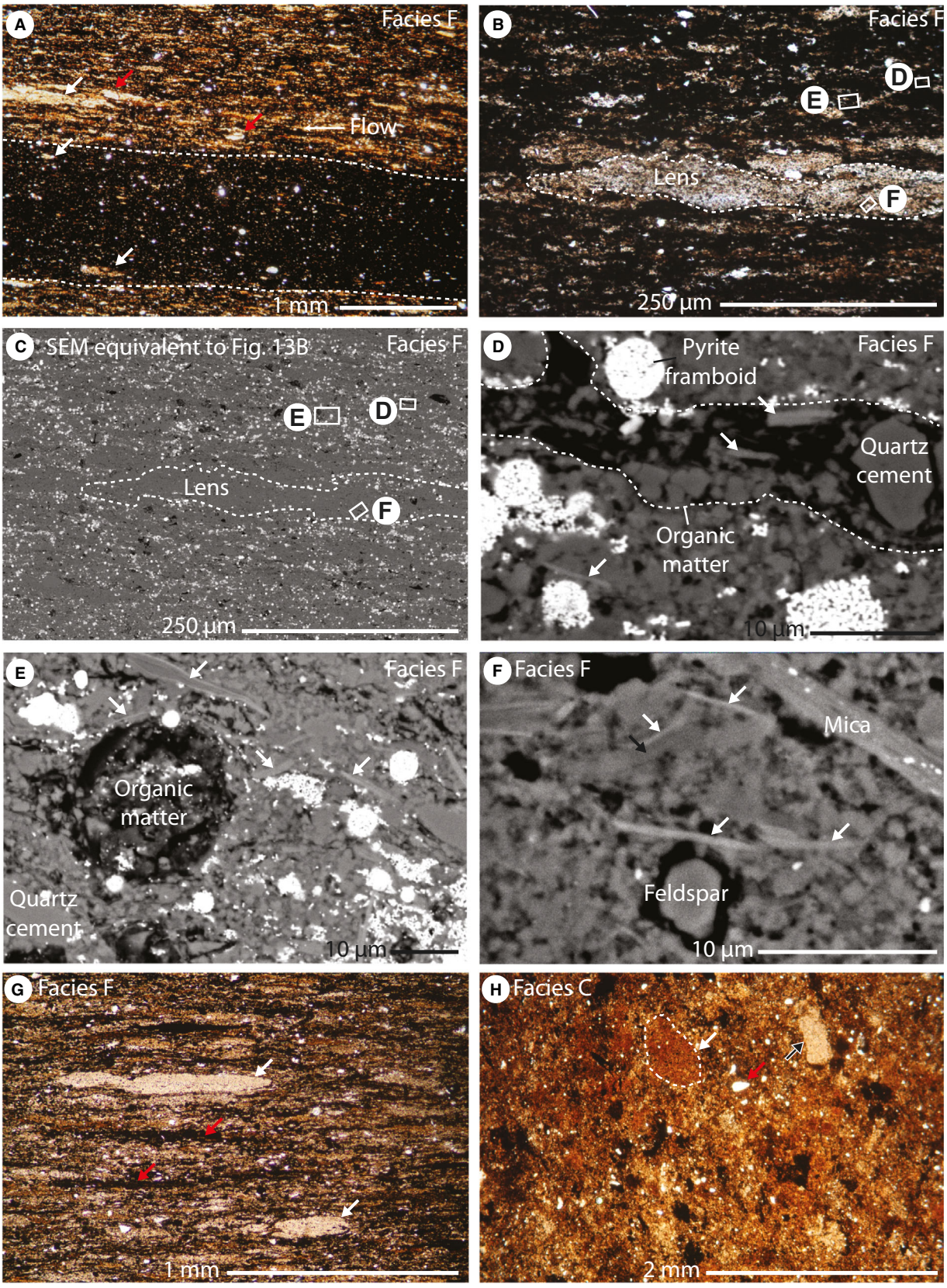

towards the base of Facies G at Hind Clough (Figs 3, 5 and 6; also compare Figs 13A, 14A and 14B) and imbrication/stacking of lenses (Figs 13A and 14H). Dominance of clay (kaolinite) and lack of OM and bioclasts in mud lenses (Fig. 13F) precludes a faecal-pellet origin (e.g. Röhl *et al.*, 2001). In some cases, lenses are composites of several smaller lenses (Fig. 14B), which may represent clasts of Facies G. Thus, the dense accumulations of lenses in Facies G (Fig. 14C to F) were potentially intermittently scoured to produce larger, composite 'clasts of clasts' observed downslope in Facies F (Fig. 14A and B).

Where Facies B, C or F overlie 'mud-cap' laminae, the contact is often sharp to slightly diffuse (Fig. 10A and B), suggesting that bottom currents at the site were capable of depositing mud clasts without substantial scour of the underlying deposits. A sharp transition from turbidite laminae into overlying lenticular muds (Facies B; Fig. 10B) also demonstrates that mud lenses are unlikely to represent burrows, on the basis that upper contacts were not homogenised. Bioturbated upper turbidite contacts in Facies H and I (Fig. 15F) are dissimilar to the lenticular fabrics observed elsewhere.

Namurian deltas generally lack sedimentary features indicative of tidal currents and to some extent wave action, suggesting river-dominance (Collinson, 1988). The region was probably shielded from high-energy waves, and long, constricted and shallow connections between basins potentially damped tidal forcing and wave energy (Keulegan & Krumbein, 1949). Yet tidal and/or wind-driven currents are thought to generate mud-rich rip-up clasts (Schieber, 2016). Bottom currents are amplified by suitable bathymetric roughness and shape (Klein & Ryer, 1978; Sztanó & Boer, 1995; Schieber, 2016), and/or favourable water depth and stratification (Egbert *et al.*, 2004). Thus, is it possible that bottom currents were locally amplified in the Craven Basin. This is supported by presence of tempestites in Facies H and I, suggestive of intermittently vigorous storm-driven bottom currents with potential for seabed scour. Microbial mats potentially also promoted biostabilization and consolidation of mud at the seabed (see below).

Particulate organic matter and candidate microbial mats

Most micron to millimetre-scale OM particles in Facies A to F (for example, Figs 13D, 13E and 14H) are interpreted as organominerallic aggregates (Tyson, 1995; Macquaker *et al.*, 2010). Lack of compaction of the spherical OM particles (Fig. 13E) indicates very early cementation around and/or within the particles. Juxtaposition of spherical and elongate forms of OM is important (Fig. 13C to E). This suggests that elongate particles are not compressed versions of originally spherical particles and supports a distinctive origin for micron-scale elongate forms of OM.

Organominerallic aggregates likely represent phytodetritus, a type of 'marine snow' (e.g. Alldredge & Silver, 1988; Macquaker *et al.*, 2010). This is common beneath productive water columns (Riley, 1971) where OM aggregates with detritus through grain collision and clumping with extracellular polysaccharides (Alldredge & Silver, 1988), precipitates from dissolved organic matter (Bowen, 1984; Velimirov, 1987; Mann, 1988) or are the faecal pellets of zooplankton (e.g. Porter & Robbins, 1981). Although the microscopic techniques utilized could not fully resolve nanoscale structures, Facies B to F contain finely (i.e. less than micron-sized) disseminated OM associated with the clay matrix (Fig. 13F) (Salmon *et al.*, 2000; Kennedy *et al.* 2014). Organic matter in Facies B to F is

Fig. 14. Strongly lenticular fabrics, including Facies G siliciclastic strongly lenticular mudstones. (A) and (B) Facies F, sample 184, 83·60 m above base, DB package, microphotograph with wide ranging size of mud lenses. This sample is near to the basal contact with Facies G – see (C) to (G). (B) Plan-view image, thin section scan, including large 'composite' lens (i.e. a lens comprising multiple lenses, white arrow). (C) to (G) Facies G, DB package, sample 188, 83·60 m above base, microphotographs [(C) to (E), plan-view: (F) inset], plan-view thin section scan (F) and BSE microphotograph (G). Facies G exhibits layering of large and abundant mud lenses (black arrows), 'mud-cap' laminae of similar composition to mud lenses and organic-rich laminae (examples: white arrows). Note also kaolinite nodules cemented by pyrite euhedra (see also Fig. 9H) and pyritized burrows – red arrow in (G). Mud lenses are coarse sand to gravel-sized and equant in plan-view (F). Organic-rich laminae exhibit 'roll-up' texture – white arrow in (E) (*sensu* Schieber, 2004) and are deformed beneath burrows (G). (H) Facies B, sample 13A, 11·60 m above base, HB package, microphotograph, including abundant mud lenses, dewatering structures and stacked lenses coupled with organic-rich fragments (red arrows).

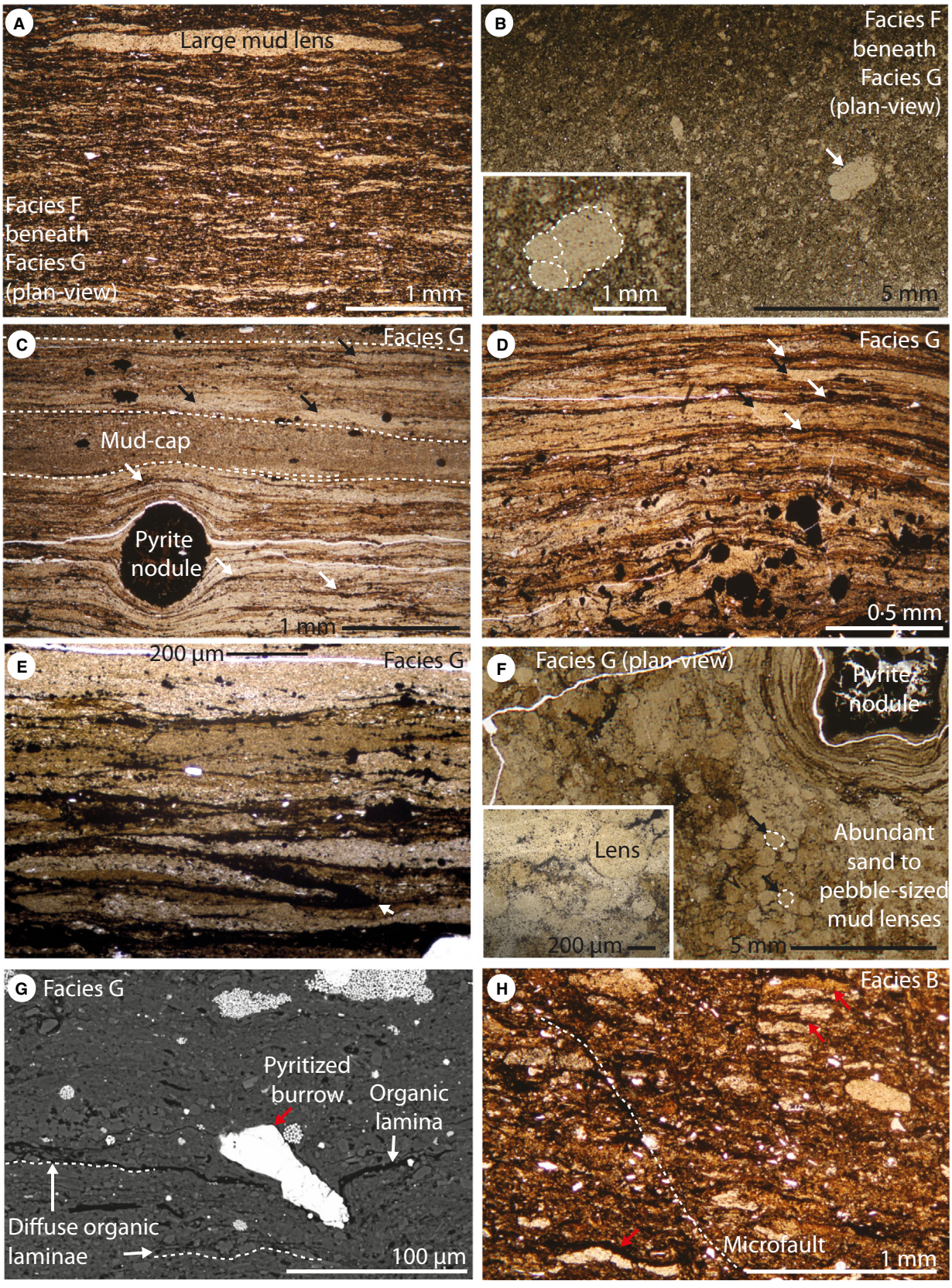

therefore comparable to the Chattanooga Shale and Marcellus Shale (Camp *et al.*, 2013). Conversely in Facies H and I, OM is in discrete, rounded to angular, spherical to elongate forms which are not mineral-bound. This texture is comparable to the Stuart Range Formation (Rahman *et al.*, 2017). Organic matter in Facies H and I (for example, Fig. 15C) is interpreted primarily as terrigenous to mixed in origin.

Organic-rich clasts in Facies E exhibit frayed edges (Fig. 12E), a feature that suggests these are fragments of microbial mats (Schieber, 1986, 2004; Schieber *et al.*, 2007b; Davies *et al.*, 2016). Relatively large elongate OM in Facies A to F also potentially represent mat fragments (for example Fig. 10C) or sheet-like organominerallic aggregates (e.g., Riley, 1971; Macquaker *et al.*, 2010; see also review by Turner, 2015; Fig. 13D). The organic laminae in Facies G (Fig. 14C to G) are interpreted as *in situ* microbial mats, similar to those described by Schieber (2004). The anastomosing nature of laminae could also support the existence of mats, although differential compaction around the mud lenses could also produce this texture (Schieber *et al.*, 2007b). Facies G is comparable to modern sedimentary and microbial textures associated with oxygen and salinity restricted conditions in similar water depth (Virtasalo *et al.*, 2011). Rare 'roll-over' of organic-rich laminae (Fig. 14E) suggests that the mats were intermittently locally re-worked. Organic-rich clasts in Facies E resemble Facies G (Figs 5, 6, 12D and 12E), and are therefore potentially down-dip, transported fragments scoured from Facies G during passage of density flows. Organic-rich laminae in Facies A are difficult to interpret due to distortion by calcite spherules but could also represent microbial mats, which were possibly a catalyst for spherule growth (Dupraz *et al.*, 2004).

Upslope colonization by microbial mats could explain the origin and relatively high abundance of mud lenses observed in Facies B to F and G. Microbial mats bind sediment, increasing the sediment tensile strength, limiting short-term erodibility and therefore initially protect muds from bottom currents that would otherwise induce scour (Neumann *et al.*, 1970). This is supported by the presence of dewatering structures (Figs 11A and 14H) and microfaulting (Figs 4 to 7, 12A and 14H) in underlying Facies B to F, and early diagenetic nodular (pyrite and kaolinite) cements (Figs 9H and 14C) and pyritized burrows (Fig. 14G) in Facies G. These observations suggest that sulphidic porewaters gently advected through, or stagnated in, relatively cohesive sediment (e.g. Rickard, 2012) beneath the candidate microbial mats in Facies G muds. Inherent instability of large microbial mats (Vignaga *et al.*, 2013), coupled with periodically stronger currents, would trigger periodic catastrophic failure of the mat and re-suspension of mat fragments and semi-consolidated (biostabilized) mud clasts. Thus, mud clasts and microbial mats were potentially genetically linked. Rare coupling of mud lenses and organic fragments 'stuck' together as single larger rip-up clasts supports this hypothesis (Fig. 14H).

Organic matter is enriched in muds via seasonal or persistent bottom water anoxia (Demaison & Moore, 1980; Tyson & Pearson, 1991), high organic loadings under productive water columns (Calvert *et al.*, 1992), sorption onto clay mineral surfaces (Keil *et al.*, 1994) and/or low sediment accumulation rate (Tyson, 2001). The presence of phosphatic fish faecal pellets and radiolaria is suggestive of at least moderate rates of primary productivity, perhaps triggered by nutrient upwelling or loading at the front of the Pendle delta. Presence of phosphate and chert nodules on the Askrigg shelf edge suggests that these conditions were relatively widespread (Davies *et al.*, 1993; Fairbairn, 2001). Facies D and E tend to exhibit relatively high Ti and Zr content compared to Facies B and C, and high excess Si content compared to Facies F. This

Fig. 15. Mostly examples of Facies H and I siliciclastic mudstones. (A) Facies D, sample 125A, 62·4 m above base, IB package, thin section scan, laminae comprise detrital quartz, carbonate grains and bioclasts, and exhibit sharp, erosive bases. (B) and (C) Facies I. Sample SSK61356, Cominco S9, DB package, 13·32 m below surface, cut-sample photograph, with sand-filled scours and overlying mud-cap. (C) Sample SSK61352, Cominco S9, 11·89 m below surface, DB package, BSE microphotograph, including mica laths (white arrows), chlorite, feldspar and quartz (black arrows). (D) Facies J, Hind Sandstone injectite, 96·0 m above base, thin section scan (sample HC03) and microphotographs (sample HC02, plane and cross-polarized light). (E) Facies H, DB package(?), sample HC01, 118·0 m above base, thin section scan, including laminae of detrital quartz coarse mud (silt), often overlain by normally graded coarse mudstone and organic-rich laminae (black arrows). Coarse mudstone laminae are often bioturbated (white arrows). (F) Facies I, sample SSK61384, Cominco S9, 28·86 m below surface, thin section scan, moderately bioturbated (white arrows) including 'mantle and swirl' textures (black arrow; *sensu* Lobza & Schieber, 1999).

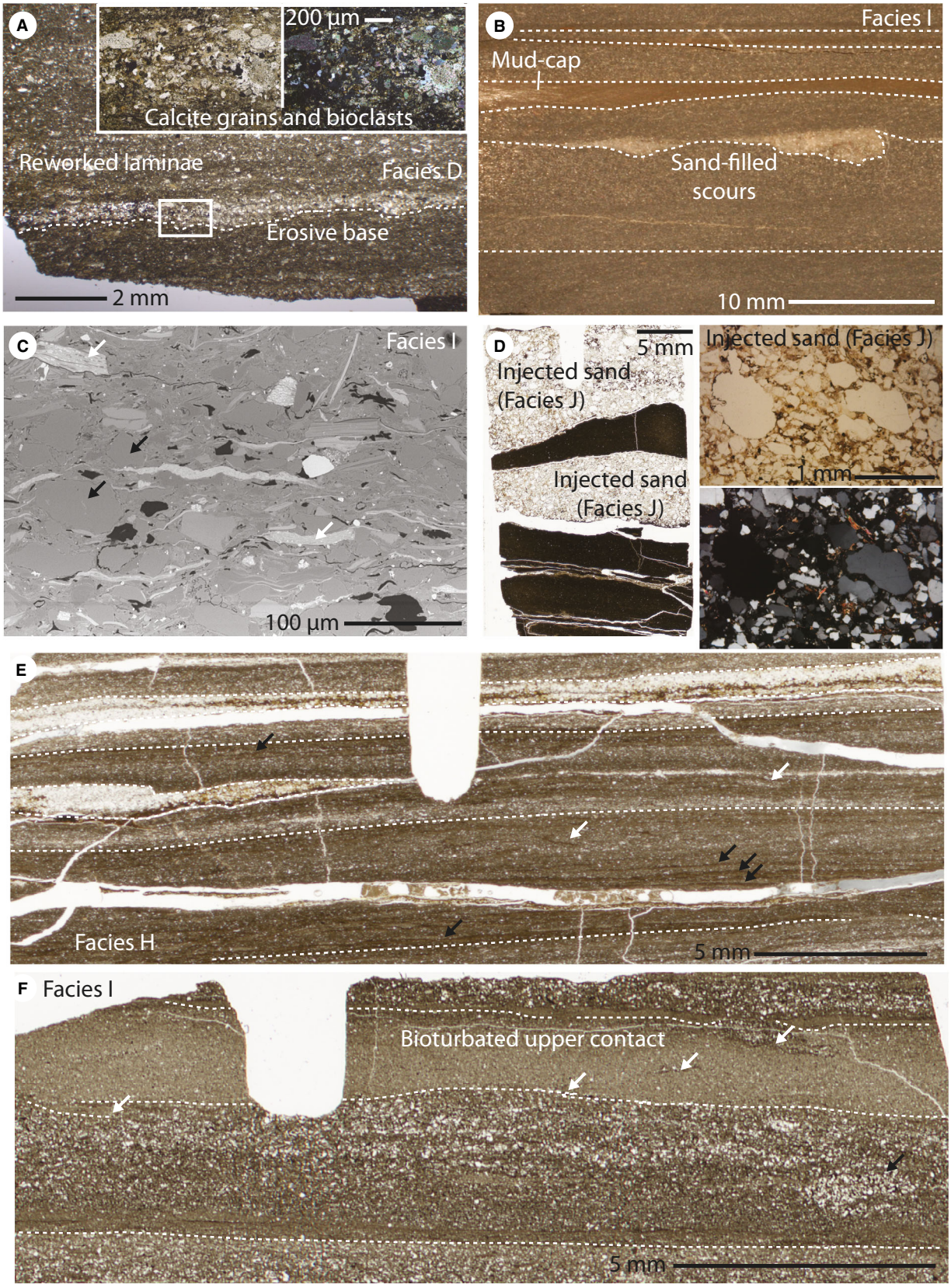

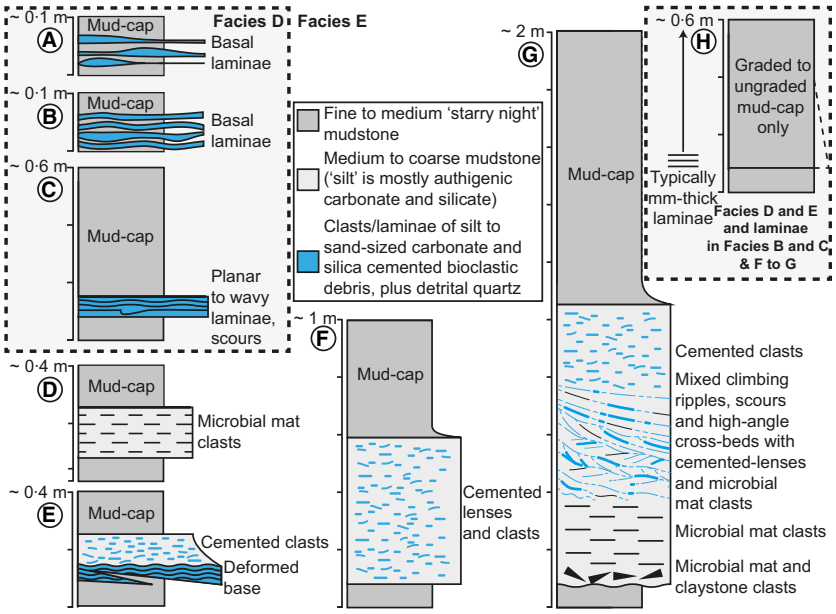

Fig. 16. Idealized subaqueous sediment density flow deposits in the Bowland Shale at Hind Clough. (A) to (C) Wavy-parallel laminated basal laminae and mud-caps of Facies D calciturbidites. (C) Cut-out low-density turbidite of Facies D (Talling *et al.*, 2012). (D) to (G) Density flows of Facies E. Mud-caps may be present without basal sections. (D) Microbial-mat-rich debrite comparable to 'quasi-laminar plug flows' of Baas *et al.* (2009) and 'Type IV' deposits of Sumner *et al.* (2009). (E) Cemented clast-rich linked-debrite with deformed basal zone (e.g. Haughton *et al.*, 2003) comparable to 'quasi-laminar plug flows' of Baas *et al.* (2009) and 'Type III' deposits of Sumner *et al.* (2009). (F) Clast and lens-rich debrite comparable to 'quasi-laminar plug flows' of Baas *et al.* (2009) and 'Type IV' deposits of Sumner *et al.* (2009). (G) High angle cross-laminated clast-and-lens-rich debrite with claystone and microbial mat clast-rich basal zone, similar to 'lower transitional plug flows' (LTPFs) (Baas *et al.*, 2011). (H) 'Mud-caps' at the top of Facies D and E and commonly as thin laminae in Facies B and C and F and G. These are slightly graded to ungraded deposits likely from dilute expanded suspensions (Stow & Bowen, 1978) or dense fluid mud layers (McCave & Jones, 1988; Talling *et al.*, 2012).

suggests that the reduced TOC in this interval is primarily a function of dilution by siliciclastic sediment and silica cement.

Abundant framboidal pyrite and lack of bioturbation in Facies A to F is consistent with the interpretation that sediment porewaters at seabed (at least) were likely euxinic and therefore toxic to infaunal organisms (Wang & Chapman, 1999). Emmings *et al.* (2017c) suggested that bottom waters were also (at least intermittently) anoxic during deposition of Facies F muds (above the E_{1a1} marine band; see Fig. 5). Several redox-sensitive trace elements (e.g. Tribovillard *et al.*, 2006), such as Mo, are enriched in Facies F and were likely fixed in association with solid sulphides (Emmings *et al.*, 2017c). These conditions apparently persisted despite relatively vigorous bottom current conditions, and were likely inhospitable to all aerobic, benthic (including infaunal, epifaunal and nektobenthonic) organisms. Clearly the relatively high TOC in Facies A to F is linked to at least moderate rates of OM export into anoxic bottom waters. Yet these processes are interlinked and often coupled. Interpretation is further complicated by the effects of changing sediment accumulation rate, autodilution (for example, radiolarian Si) and remineralization of OM during diagenesis.

Facies H and I exhibit lower TOC concentration than any other facies (excluding Facies A). Bioturbation in these facies suggests that bottom waters were at least intermittently oxygenated and supported benthic fauna (Eagar *et al.*, 1985). Thus, oxygenated bottom waters, increased bioturbation, dilution by detrital sediment, weaker organic loadings, change in mineralogy, change in sediment properties (for example, porosity) and/or change in OM type and distribution are all viable mechanisms for the relatively low TOC in Facies H and I.

Marine bands

Discrete and repeated packages of carbonate-rich macrofauna-bearing Facies B interbedded with

Facies A, C and D fit with definitions of marine bands (Ramsbottom, 1977; Waters & Condon, 2012). Facies B and C (Figs 9B to F, 10C to E and 11B to F) are interpreted as mixed pelagic and hemipelagic sediments (Table 1), interbedded with calciturbidites (Facies D), deposited during periods of increasing to high basin (IB to HB) accommodation (Posamentier *et al.*, 1988; Martinsen *et al.*, 1995).

Facies B body fossils are primarily euhaline ('normal marine') and pelagic (e.g. Flügel, 2004), equivalent to the faunal phases 4 to 6 of Ramsbottom *et al.* (1962). Goniatites were nektonic and probably relatively intolerant to basin desalination events (Ramsbottom & Saunders, 1985). The Pendle delta system likely induced a strong salinity gradient (Collinson, 1988) with potential for euhaline faunal occlusion. This explains why Facies H and I, deposited under a freshwater column (TOC/S > 10), are 'barren' (Fig. 7). Freshwater likely prograded as a plume from the Pendle delta, and was not basin-wide. All other mudstones were likely deposited in marine conditions, on the basis of low TOC/S (Berner & Raiswell, 1984). Lack of bioclasts in Facies C (Fig. 11B and F) suggests either that conditions in the water column were unfavourable for colonization, perhaps due to reduced salinity (Ramsbottom *et al.*, 1962), or that the aragonitic bioclasts (e.g. Flügel, 2004) were not preserved at the seabed (Ku *et al.*, 1999).

Mississippian trilobites (Fig. 10E) were primarily benthic organisms (e.g. Flügel, 2004). This suggests that bottom water anoxia, as a possible explanation for the relatively high TOC, was transient or that the trilobites were tolerant to sub-oxic conditions (Fortey & Wilmot, 1991). Nyhuis *et al.* (2015) favoured this explanation for the presence of trilobites in concomitant rocks. Alternatively, trilobites and mud lenses were potentially transported together, from a nearby oxic and euhaline basinal high, downslope, into anoxic bottom waters. This is the favoured explanation for presence of benthic fauna in the contemporaneous US Barnett Shale (Loucks & Ruppel, 2007).

Relatively small mud lenses in marine bands (Figs 3 to 7) possibly indicates that the provenance of mud lenses shifted further away onto adjacent shelves (Figs 2A and 10C to E) and that clasts were fractionated over a longer run-out distance during marine transgressions. The basal Facies B package in the E_{1a1} marine band is an exception to this pattern, however, because it contains relatively large mud lenses similar to Facies F (Fig. 5). Perhaps these large clasts were shed initially from relatively steep and mud-rich (syn-rift) slopes on adjacent highs (Fig. 2A) during the E_{1a1} marine transgression (Fig. 1). Subsequent marine bands possibly lack these relatively large lenses because local highs lacked available mud, perhaps because the inherited syn-rift structures became progressively infilled and smoothed during progradation of the Pendle delta. Relatively abundant and large clasts in Facies F, likely deposited during periods of reduced basin accommodation (Figs 13A, 13B, 14A and 14B), suggests that clasts were sourced nearby or that bottom currents were enhanced.

In Cominco S9 mudstones in the E_{1c} marine band are finely lenticular, whereas the underlying and overlying Facies H and I lack mud lenses and instead comprise coarse mud (silt) and fine sand (Fig. 7; Fig. 10D *versus* Fig. 15B and C). The switch from marine band fine mudstone to coarse mudstone, is indicative of the movement of a pseudo-'mudline' in response to eustatic sea-level fluctuation (Weaver, 1989). During periods of high sea-level, mud-rich sediments accumulated close to Cominco S9 (i.e. on the Askrigg Block or adjacent slope) and were intermittently scoured and transported as rip-up clasts to be deposited as part of the E_{1c} marine band. In more distal and older marine bands, pelagic components tend to dominate over mud lenses, possibly because bottom currents transporting lenses had run-out. During the subsequent sea-level fall, coarse mud (silt) was deposited primarily via turbidity currents at Cominco S9, whereas mud likely bypassed this proximal site.

Phosphate concretions

Phosphatic concretions in Facies B (Fig. 9D to F) are interpreted as early-cemented faecal pellets, possibly from fish (Saba & Steinberg, 2012; Zatoń & Rakociński, 2014). These are compositionally similar to phosphatic bromolites described by Hunt *et al.* (2012) and geometrically comparable to siderite-cemented coprolites in the Mississippian Lower Oil Shale Group (Bojanowski & Clarkson, 2012). Preservation of contents, such as radiolarian tests (mostly spumellarian entactinids; Casey, 1993), skeletal material and amorphous OM (Fig. 9F; e.g. Tyson, 1995) in unflattened geometry indicates that cementation occurred very early. Radiolarian tests are preserved within the phosphate concretions as thin organic linings rafted in phosphate cement (Fig. 9F). Radiolarian silica

dissolved and locally precipitated within each concretion as patchy quartz cements (Fig. 9F). Modern radiolaria often host symbionts as mixotrophs (Mitra *et al.*, 2016). This means that radiolaria are important primary producers in some marine environments (e.g. Caron *et al.*, 1995) and that radiolarian OM could have contributed significantly to the organic fraction in these rocks. The presence of radiolaria is further evidence for at least intermittently euhaline upper water column conditions (e.g. Flügel, 2004).

Absence of radiolarian tests outside concretions suggests that the relatively labile silica tests completely dissolved and, in the absence of the protective early phosphate cement, silica-rich fluids then re-precipitated in pores as clay and/or quartz cement during early diagenesis (e.g. Taylor & Macquaker, 2014). The high abundances of radiolarian linings preserved in the concretions and pervasive quartz cements elsewhere is important. Interpreting concretion contents as an approximation for the local pelagic fraction deposited at each site, this supports a pelagic and biogenic origin for the excess silica, and for many or all of the patchy quartz and clay mineral cements in the matrix (Figs 9B, 9C and 13D). It is beyond the scope of this paper to further discuss diagenetic phases (e.g. Curtis, 1977; Kastner *et al.*, 1977; Moore *et al.*, 2004; Macquaker *et al.*, 2014). These phases include spherulitic calcite (Facies A; Fig. 9A), patchy calcite (Fig. 9C), fine framboidal (Fig. 13A to E) and euhedral and nodular (Fig. 14C to G) pyrite, sulphate (Fig. 11G), scattered dolomite replacing calcite (Figs 9B, 9C and 12G), quartz (Fig. 9B) and clay mineral cements (Fig. 9G and H).

Controls on Craven Basin infill

Field to micron-scale analysis of the Upper Bowland Shale demonstrates that the epicontinental Craven Basin received sediment from three provenances. Firstly, detrital clay, coarse mud (silt) and sand supplied via turbulent and hybrid flows, including direct supply from the Pendle delta system; secondly, clay-rich mud clasts scoured from nearby mud-rich, potentially biostabilized, slopes; and, finally, pelagic and hemipelagic sediment, rich in clays, OM and biogenic carbonate and, silica. Changing basin accommodation, moderated by eustatic sea-level fluctuation, delta progradation and fault instability at the basin margins moderated the supply of sediment from these provenances.

Changing basin accommodation

At Hind Clough relatively thin packages of marine band Facies B and/or C, interbedded with low density turbidites of Facies D, are interpreted as deposition during periods of increasing basin (IB) accommodation (Figs 5 to 7). Siliciclastic turbidites in IB packages could represent the final flows through shelf to basin conduits (for example, canyons), such as via the Dent Fault between the Southern Lake District High and Askrigg Block (Fig. 2). Such flows were potentially cut-off by rising sea-level (Piper & Normark, 2009; Talling, 2014). Turbidites could also represent failure of sediments that accumulated at canyon heads by longshore drift (Covault & Graham, 2010). Calciturbidity currents were also potentially sourced by slope failure of the flank of the Askrigg Block and local highs, by loading via carbonate accumulation on slopes, or possibly thicker and/or warmer water column (e.g. Maslin *et al.*, 2004; Talling, 2014).

Increasing basin (IB) packages (Figs 4 to 7) record the increasing and decreasing input of (hemi)pelagic mud and turbidity currents with time, respectively. This is consistent with increasing rarity of thin calciturbidite beds (Facies D; Figs 10H and 15A) and progressive dominance of calcareous lenticular mudstones (Facies B and C). Juxtaposition with overlying marine bands suggests that IB packages were deposited during rising eustatic sea-level driven by onset of deglaciation on Gondwana (Veevers & Powell, 1987). The IB packages may therefore correspond to the transgressive systems tract (Posamentier *et al.*, 1988). At MHD4, an equivalent IB package is highly condensed (Fig. 4) likely because the isolated basinal high position further limited sediment supply.

The contact between the IB packages and overlying carbonate-rich packages is relatively sharp at Hind Clough and MHD4, and is attributed to the transition from increasing to high basin (HB) accommodation. The HB packages best fit the definition of marine bands. The HB packages were almost certainly deposited during periods of high eustatic sea-level (e.g. Ramsbottom, 1979; Fig. 17A) and therefore represent deposition initially during the maximum rate of transgression and the subsequent highstand systems tract (high to slightly decreasing basin accommodation) (Posamentier *et al.*, 1988). Relatively high TOC, carbonate and excess silica content in HB packages (Figs 4 to 7) is consistent with a dominance of calcareous, weakly

lenticular mudstones (Facies B and C; for example, Fig. 10E). Calciturbidity currents (of Facies D; for example, Fig. 10G and H) were probably delivered by shedding from local carbonate-rich highs (Fig. 17A). These calciturbidites are more abundant in older marine bands (E_{1a} and E_{1b1}) possibly because fringe reefs/carbonate accumulations on the shelf or slope were relatively widespread (Fig. 2A).

At Hind Clough, lenticular Facies F and G commonly overlie the HB packages and are collectively interpreted as deposition during periods of decreasing basin (DB) accommodation. Persistence of DB packages above HB packages suggests a common driver. Decreasing basin packages may therefore form part or all of the falling stage systems tract (Posamentier *et al.*, 1988). Accommodation in shallow waters reduced sufficiently to permit scour of previously deposited (and biostabilized) muds and transport as clasts into the basin. Above the $E_{1a1\text{-}b}$ marine band, a conformable package (DBa) is overlain by an inclined package (DBb) (Figs 5 and 11C to E). The majority of scoured sediments were possibly initially trapped in proximal positions because clasts are typically small in DBa (Fig. 17B). An increasing supply of mud lenses and thin 'mud-cap' laminae (Facies F; for example, Figs 11C to E and 13A to G) during falling sea-level is consistent with an increasing abundance of detrital elements towards the top of each DB package (Figs 4 to 7).

Given that the primary source of sediment was likely from the north-east (e.g. Collinson, 1988), the inferred angle of palaeodip (towards the north-east) of package DBb is the reverse of the expected direction for progradational clinoforms (e.g. Hampson, 2010) from the Pendle delta (north-east). Lack of deformation structures probably also discounts a slope failure origin for this structural change. This geometry could represent an aggradational and onlapping package of lenticular sediments that accumulated on a gently sloping seabed. Bottom currents transporting the mud clasts rapidly decelerated, and aggraded, on the relatively low-gradient seabed at Hind Clough. Given that lenses are typically larger and more abundant than the conformable DBa package beneath, this implies a phase of more significant sea-level fall, increased sediment supply and/or tectonic uplift (Fig. 17C). Intermittent presence of goniatite moulds, cemented lenses, increased excess silica and Facies D interbeds (Fig. 5) in package DBb suggests a pulse of increased basin accommodation (possibly the $E_{1a1\text{-}c}$ flooding event; Fig. 1C, perhaps local rather than regional). This increase in basin accommodation was insufficient to isolate the basin from the primary source of rip-up clasts.

Above the DBb package at Hind Clough, the succession of density flow deposits (Facies E) (Figs 5 and 16) is interpreted as deposition during a period of decreasing to low basin (LB) accommodation (Fig. 17D). Delta progradation coupled to falling sea-level and/or slope instability at the fault-bound basin margins could have triggered these mass transport processes (Piper & Normark, 2009; Talling, 2014). This is consistent with the relatively high abundance of detrital elements in LB packages. Beneath the E_{1a1} marine band in MHD4, a discrete package of Facies B and C with slump structures is also interpreted as a LB package (Fig. 4).

The transition between types of hybrid flows in Facies E (Figs 5 and 6) potentially relates to changing sea floor geometry or the type of sediment entrained in the flow. At the onset of deposition of the E_{1a} LB package at Hind Clough, flows potentially passed over a low-gradient and/or irregular seabed relief defined by the underlying onlapping DBb package (Figs 11C to E and 17D). This relief probably promoted rapid deceleration of the flow and scour of underlying sediment. Following this initial deceleration, steady flows were apparently long-lived. Gradual infill and/or smoothing of the basin sea floor could therefore explain the transition between deposit types. A reduction in clay content, possibly due to increased input of coarse mud and sand from the Pendle delta, changing seabed geometry, a change in the type of failed sediment and/or reduced entrainment of clays and OM during passage, promoted sediment deposition from more turbulent flows above the E_{1b1} marine band. The succession between E_{1b1} to $E_{1b2\text{-}b}$ marine bands (Figs 6, 17D and 17E) is interpreted as a combination of changing basin accommodation and mass transport processes potentially triggered by slope failure at the fault-bound margins of the basin (Fig. 2A).

The $E_{1b2\text{-}b}$ DB package is associated with colonization and biostabilization of the seabed by candidate microbial mats at Hind Clough (Facies G). Such mats potentially occupied a niche environment linked to delta progradation (Fig. 17F), perhaps associated with a high redox gradient at seabed (Grunke *et al.*, 2011). Overlying the $E_{1b2\text{-}b}$ DB package at Hind Clough, Facies H to J

(Fig. 3A) are collectively interpreted as a LB package. This package represents a significant step-change in the basin evolution, however, with the introduction of coarse siliciclastic fill as the turbidite-fronted Pendle delta (e.g. Collinson, 1988). This explains the enrichment in detrital elements through the E_{1c1} LB package (Fig. 7). Shelfal and basinal barriers had become sufficiently infilled and/or breached, ultimately permitting development of the Pendle Grit toe of slope fan in the Craven Basin (Martinsen *et al.*, 1995). This was potentially fed by a lowstand-dominated river-fed canyon system (Covault & Graham, 2010), perhaps as a breach along the Dent Line between the Askrigg Block and Southern Lake District High (Fig. 2A). Thus, the E_{1c1} DB package was potentially originally much thicker in Cominco S9 but was scoured during deposition of the overlying LB package (Figs 7 and 15B). Associated with this increased siliciclastic input, a plume of freshwater extended from the Pendle delta outflow across the adjacent Askrigg Block to (at least) the proximal margins of the Craven Basin.

Delta progradation and slope instability

The potential for complex sediment routing and sediment lock-up in more proximal basins towards the north-east of the Askrigg Block (for example, Stainmore Trough) meant that the Pendle delta system was poorly (but increasingly) connected to the Craven Basin during deposition of the Bowland Shale. Siliciclastic turbidity currents supplied directly from river-fed canyons likely initially followed circuitous routes first through adjacent basins (for example, the Cleveland Basin to the east), around the Askrigg Block (perhaps through the Dent Line; Fig. 2A), before deposition into the Craven Basin (Brandon *et al.*, 1998; Fraser & Gawthorpe, 2003). The entrance points in adjacent basins were likely poorly connected to the Pendle river system, with potential for stranding of canyons at the shelf break (for example, lowstand-dominated; Covault & Graham, 2010).

Mud lenses typically increase in size and abundance in Facies F through the section at Hind Clough, because adjacent intrabasinal mud traps, such as on the South Craven Fault, were progressively infilled with mud sourced from the Pendle delta (for example, Fig. 17E). Therefore, a greater area of (potentially biostabilized; Fig. 17B) mud-rich seabed was likely exposed to erosion by wave shear and/or storm-driven currents. Thus, biogenic input (delivered via bedload or pelagic settling) was increasingly diluted by the escalating input of rip-up clasts and hemipelagic settling of detrital clays. Whilst the main basin margin with the Askrigg Block likely retained the sharp 'block-edge' geometry (Fig. 2A) into the E_{2c} biozone (Martinsen *et al.*, 1995), mud was likely available on the Askrigg Block (Hudson, 1940) as a source for mud clasts.

Unconformities north of the Middle and South Craven faults suggest periods of inversion, especially within the E_{1a} biozone (Hudson, 1940; Rowell & Scanlon, 1957; Arthurton *et al.*, 1988). 'Limestone boulders' in the footwall of the South Craven Fault (Arthurton *et al.*, 1988) are broadly contemporaneous with the Facies E beds observed at Hind Clough. Therefore at least some of the hybrid flows were likely fed by slope failure on the scarps of the Middle & South and/or North Craven faults (for example, Fig. 17D) or other fault-bound highs. Both Middle and South and North Craven faults bounding the Craven Basin were intermittently active and/or the basin flexed at these points, in order to accommodate the basin subsidence required for accumulation of the several kilometre-thick Millstone Grit Group succession on top of the Bowland Shale in the Craven Basin (e.g. Fraser & Gawthorpe, 2003).

Synthesis

Figure 18 is a conceptual cross-section across the Craven Basin (Fig. 2A) which integrates findings across the three sites and stratigraphic relationships on the Askrigg Block and slope. It simplifies the expected heterogeneities in sediment package geometries, particularly across intrabasinal highs and lows. The strong asymmetry of packages is characteristic of sediments deposited under the combined influence of eustatic sea-level fluctuation and basin subsidence (e.g. Martinsen *et al.*, 1995). Initially the basin exhibited steep bounding slopes ('block-edge' geometry) and fringing reefs on both South and North Craven faults (e.g. Wensleydale Group; Arthurton *et al.*, 1988). Thus the Lower Bowland Shale in the Craven Basin represents a carbonate-dominated succession fed by unstable basin margins (Newport *et al.*, 2018). Linked-debrites of Facies E are similar, although not equivalent, to Facies 5 of Newport *et al.* (2018). Shedding of carbonate from reefs (e.g. Riley, 1990) contributed to the comparatively large carbonate component, with potential for basinal thickening, in the E_{1a1} marine band. These

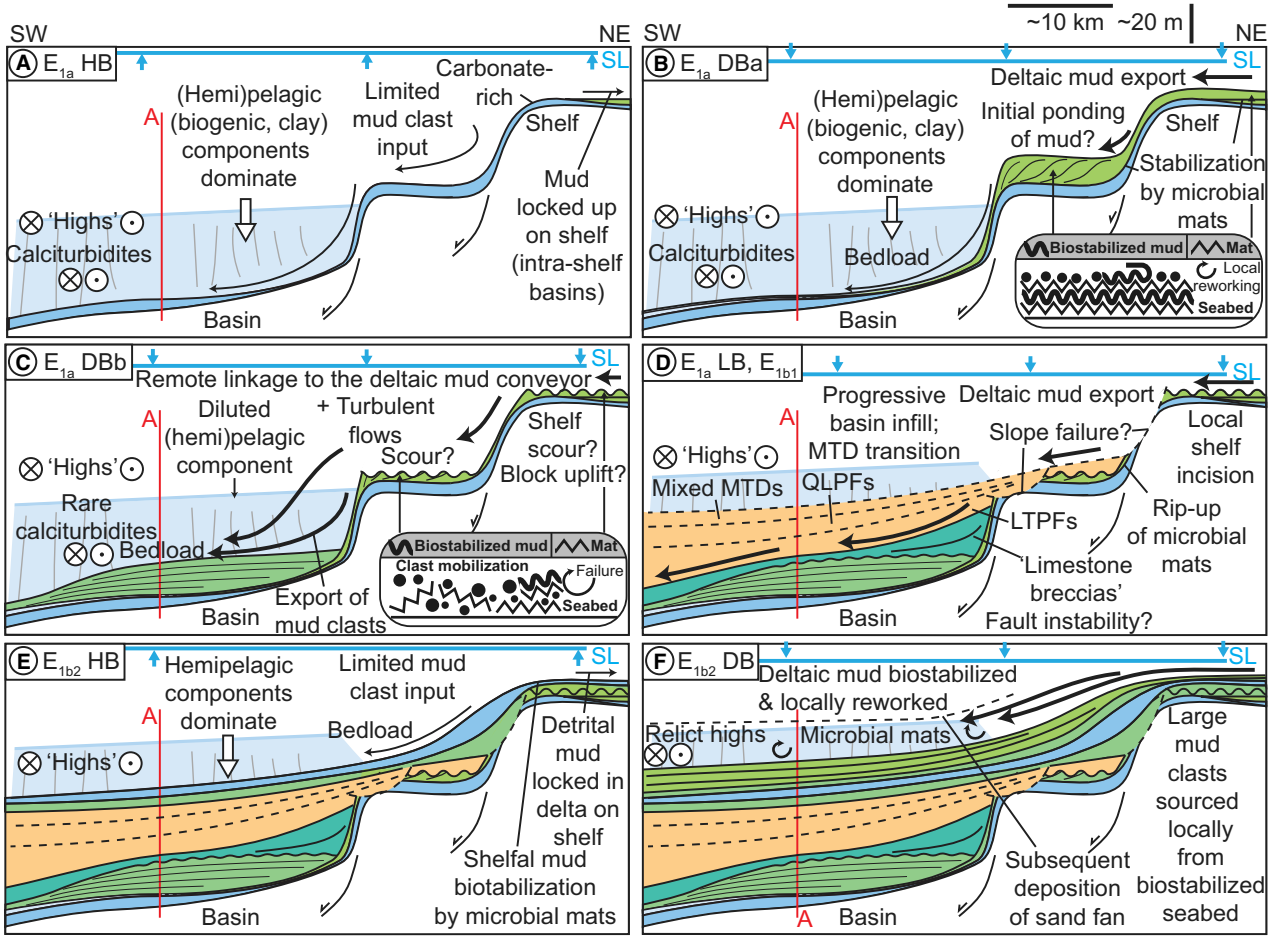

Fig. 17. Cross-section from the Askrigg Block (north-east) to Craven (Bowland) Basin (south-west) for a range of basin accommodation states. Section A, Hind Clough, is marked for reference. SL = estimated position of sea-level (relative). See Fig. 18 for supporting references regarding basin structure and shelfal hiatuses. (A) to (D) Represents a single fourth-order cycle, including: (A) deposition of the E_{1a1} marine band during a period of increasing to high basin (HB) accommodation (sea-level highstand); (B) deposition of rip-up clasts transported from the upper slope or shelf, possibly biostabilized by microbial mats (Facies G), during decreasing basin (DBa) accommodation; (C) widespread scour and failure of partially consolidated, biostabilized muds on the shelf and/or slope and deposition as an aggradational lenticular package during continued decreasing basin accommodation (DBb); (D) development of a mid-E_{1a} unconformity on the shelf and upper slope during low basin (LB) accommodation via sea-level fall or uplift of the Askrigg Block. Density flow deposits (MTDs) transition from quasi-laminar plug hybrid flows (QLPFs), lower transitional plug hybrid flows (LTPFs) and mixed mass transport deposits (including turbidites, linked-debrites and LTPFs). (E) A period of increased basin (IB) accommodation via E_{1b2} sea-level rise resulted in deposition of calcareous bioclastic lenticular sediments coupled to shelfal mud biostabilization. Facies D calciturbidites are absent, suggesting cessation of carbonate production and/or slope failure on nearby basin highs. See (B) for mud biostabilization model. (F) Progradation of the Pendle delta, potentially coupled with sea-level fall, reduced basin accommodation and promoted expansion of microbial mats and local reworking of large rip-up mud clasts. See (B) for mud biostabilization model.

calciturbidites (Facies D) are partially equivalent to the homogenous and lag-containing Facies 1 in the contemporaneous Morridge Formation, in the Widmerpool Gulf (Könitzer *et al.*, 2014) and Facies 4 of Newport *et al.* (2018).

Progressive basin infill and cessation of rifting (Leeder, 1982) smoothed and infilled intrabasinal structures. This regional shift in intraplate deformation style promoted deposition of discrete marine band packages (Facies A to C) in the Upper Bowland Shale, driven by fourth-order eustatic sea-level cyclicity. Equivalents are observed in many other Namurian successions (see Waters & Condon, 2012), such as Facies 1 of Könitzer *et al.* (2014). These 'marine band' packages are also texturally comparable to

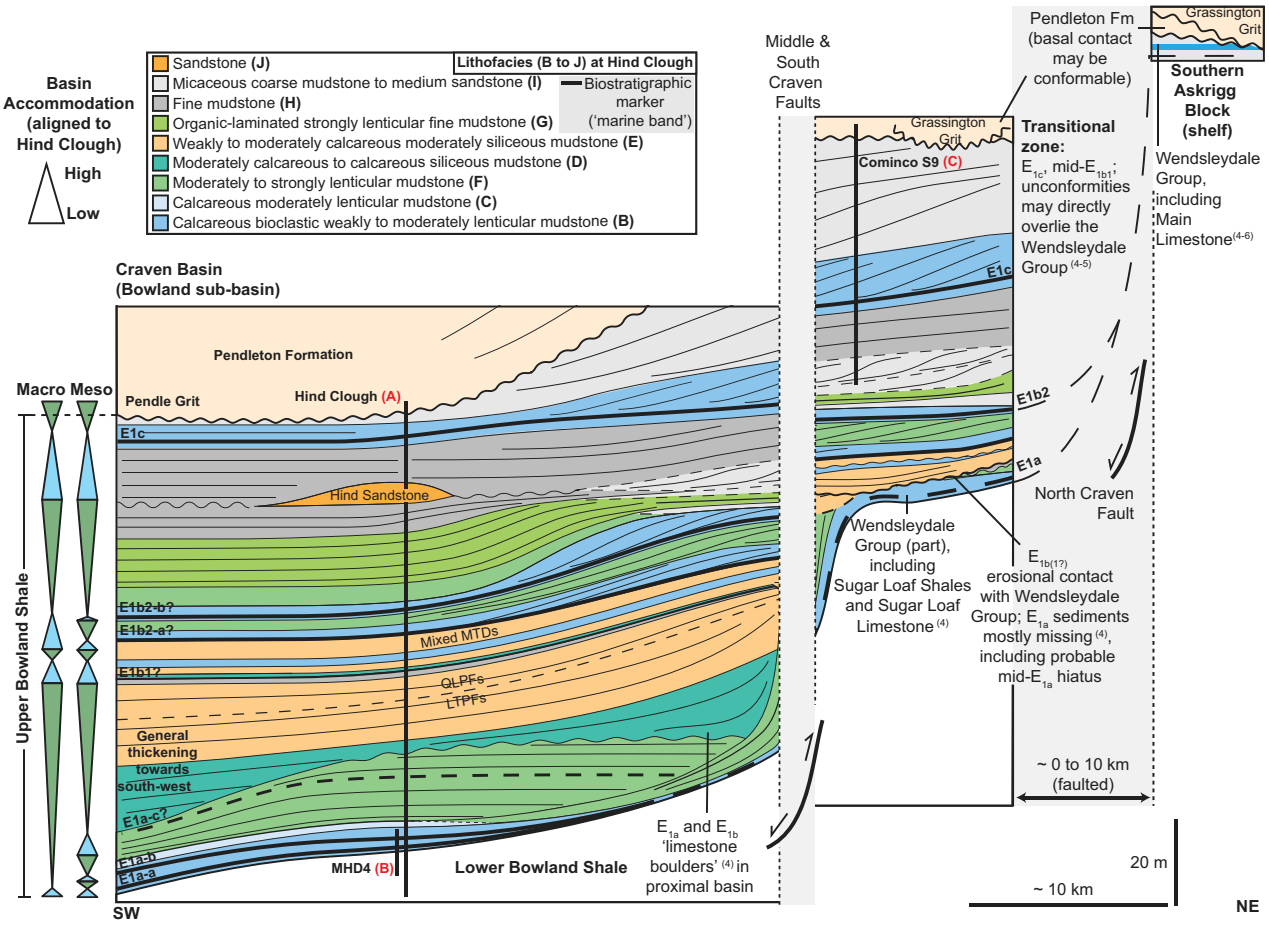

Fig. 18. Cross-section from the Askrigg Block (north-east) to Craven (Bowland) Basin (south-west), with extrapolated sedimentary facies observed at Hind Clough (A), MHD4 (B) and Cominco S9 (C). '1' Aitkenhead *et al.*, 1992; '2' Brandon *et al.*, 1998; '3' Kirby *et al.*, 2000; '4' Arthurton *et al.*, 1988; '5' Rowell & Scanlon, 1957; '6' Hudson, 1940. See text for *Discussion* and see Fig. 2 for transect position.

several intervals in the Lower Bowland Shale (Facies 1 and/or 2; Newport *et al.*, 2018), which are relatively diffuse, likely due to the combined effects of active rifting and diminished glacio-eustasy (Veevers & Powell, 1987).

Packages are likely to be most spatially complex in the E_{1a1} biozone, and progressively simplify as the basin evolved towards a muddy ramp-type system. Lenticular muds are present in both the Upper (Facies F) and Lower Bowland Shale (Facies 3 of Newport *et al.*, 2018), and are common in many epicontinental successions (for example, Facies 3, 4a and 4c of Könitzer *et al.*, 2014). Highly lenticular Facies G may represent a clast-rich version of Facies 3, or Facies 4a, of Könitzer *et al.* (2014). Abundant and relatively large rip-up clasts in DB packages suggest that scour of shelfal mud-rich successions is the most likely provenance for such clasts. Linkage between highly lenticular, microbial-mat-bearing Facies G deposited during delta progradation (Fig. 17F) suggests that clasts were sourced specifically from prodeltaic and biostabilized muds trapped on shelves and slopes. Under a thermal sag regime, proximal basins, such as the Stainmore Trough (e.g. Waters *et al.*, 2009), were infilled by the Pendle delta system and ultimately connected the Craven Basin with the Pendle prodelta. Unconfined delta progradation triggered the development of a toe of slope fan system in the Craven Basin, recognized as Facies H to J. These facies are partially comparable to Facies 4a and 5 in the Morridge Formation (Könitzer *et al.*, 2014).

Taking 100 m of uncompacted lenticular sediment (assuming 55% compaction) (Fig. 11B and F), deposited over *ca* 400 ka (spanning E_{1a1}–E_{1b2} marine bands; Waters & Condon, 2012), yields an estimated *ca* 0·250 mm year^{-1} mean sediment accumulation rate (SAR; Fig. 3B).

Assuming deposition over *ca* 1·8 Myr (using the chronostratigraphy of Waters *et al.*, 2011), an uncompacted sediment thickness of 100 m (assuming 55% compaction), the Lower Bowland Shale basinal high succession (P_2 biozone) described by Newport *et al.* (2018) exhibits a SAR of *ca* 0·055 mm year^{-1}. This compares with *ca* 0·080 mm year^{-1} SAR calculated for an average Lower Bowland Shale thickness in the Lancaster Fells sub-basin (after subtraction of the Pendleside Sandstone member; Brandon *et al.*, 1998). Similarly, SARs of 0·013 mm year^{-1} and 0·002 to 0·008 mm year^{-1} are estimated for the contemporaneous Barnett Shale (Loucks & Ruppel, 2007) and North American Late Pennsylvanian Midcontinent Seaway cyclothems (Algeo *et al.*, 1997, 2008), respectively (Fig. 3B).

Attaining an appropriate estimate for SARs across different settings is clearly problematic and depends on an appropriate assignment and understanding of sedimentary facies. Lenticular mudstones are perhaps best interpreted as deposits on a continuum of processes (e.g. Rebesco *et al.*, 2014) between mud densite (Talling *et al.*, 2012) and (hemi)pelagite end-members. Weakly to moderately lenticular 'marine band' mudstones (Facies B and C) are dominated by hemipelagic and pelagic components and are therefore interpreted as (hemi)pelagites with subordinate densite mud. Strongly lenticular mudstones (Facies F and G) are interpreted primarily as mud densites mixed with subordinate hemipelagite.

The estimated SAR calculated for the Bowland Shale is an order of magnitude higher than the Barnett Shale. This cannot be explained solely by different timespans (i.e. frequency of hiatuses). Clearly the export of mud from the Pendle delta system was large and relatively fast, despite shielding by the Askrigg Block and intrabasinal complexity. The SARs estimated for the Bowland Shale and contemporaneous Morridge Formation are closest to the 'deltaic' median SAR (Fig 3B; after Sadler, 1999). This high SAR is linked to the evidence for widespread and sustained deposition both from bedload and suspension. All other the organic-rich mudstone successions are closest to abyssal plain, abyssal rise, continental slope and/or turbidite fan median SARs (Fig. 3B). Considering that the Bowland Shale is up to 500 to 700 m thick into the deeper basin (Aitkenhead *et al.*, 1992; Brandon *et al.*, 1998; Kirby *et al.*, 2000; Clarke *et al.*, 2018), a relatively large volume of sediment likely also bypassed the studied sites. This is consistent with the interpretation of deposition of rip-up clasts by laminar flows, and passage of hybrid flows with variable degrees of turbulence damping. 'Allogenic' megaflutes in the Hind Sandstone (Kane *et al.*, 2009) also support this interpretation.

The Bowland Shale is heterogeneous, with a significant clay component, compared to the Barnett Shale (Loucks & Ruppel, 2007). Whilst the marine bands of the Upper Bowland Shale are likely the most prospective horizons (high TOC, carbonate and quartz cementation and widespread occurrence; Jarvie *et al.*, 2007), the composition of each marine band varies considerably depending on basin position and age. Marine bands deposited during the early stages of basin infill, within inherited rift structures, are likely to be more complex than younger marine bands. Hybrid event beds exhibit lower TOC but are compositionally varied, due to their probable slope failure origin. Given the extensive cementation in these units, hybrid event beds may be considered prospective for unconventional hydrocarbon extraction. However, the geometry of such deposits is likely to be complex. Hind Clough is located in a relatively deep and confined part of the basin (Fig. 2A; see also Kane, 2010), which likely explains the relatively abundant hybrid deposits.

CONCLUSIONS

The Bowland Shale is an organic-rich mudstone that exhibits substantial compositional heterogeneity. Geochemical and sedimentological analyses at the bed, hand specimen and thin section scale from three localities in the Craven Basin demonstrate:

1 The epicontinental Craven Basin was supplied by three sediment provenances. Firstly, detrital clay, coarse mud (silt) and sand supplied via turbulent and hybrid flows, including direct supply from the Pendle delta system; secondly, clay-rich mud clasts scoured from nearby mud-rich, potentially biostabilized slopes; and finally, pelagic and hemipelagic sediment, rich in clays, organic material (OM) and carbonate.

2 A variety of laminar, turbulent and hybrid flows developed during periods of reduced basin accommodation and/or fault activity.

3 Lenticular fabrics indicate persistent deposition of mud clasts from bedload. Mud clasts are interpreted as rip-up clasts, generated by bottom

current scouring of partially consolidated mud. Lenticular mudstones represent mixtures of (hemi)pelagic and densite muds. Mud clasts were potentially biostabilized by microbial mats. The Pendle prodelta was likely the primary source for these mud clasts, demonstrating the far-reaching effects of the delta system.

4 Marine transgressions ('marine bands') promoted pelagic and hemipelagic settling, including fixation of abundant biogenic silica, and diminished mud density flows.

5 Lack of bioturbation and benthic faunal tests during the early phases of basin infill and in all marine bands suggests that bottom waters were at least intermittently anoxic.

6 Abundant organominerallic aggregates, silica enrichment, phosphatic faecal pellets containing radiolaria and pelagic macrofauna suggests that the water column was productive.

7 Candidate *in situ* microbial mats, and as rip-up clasts in a variety of down-dip hybrid event beds, were potentially important consolidators of mud and burial of OM.

8 The Bowland Shale accumulated an order of magnitude faster than other epicontinental mudstones, such as the Barnett Shale, and the Lower Bowland Shale unit.

Epicontinental basins remotely linked to delta systems, such as the Craven Basin, were capable of rapidly accumulating both sediment and OM. This rapid accumulation has implications for understanding the role of epicontinental seaways as a carbon sink and the present day hydrocarbon prospectivity of these mudstones.

ACKNOWLEDGEMENTS

This study was funded by the Natural Environment Research Council (NERC), (Grant no. NE/L002493/1), within the Central England Training Alliance (CENTA) consortium. The study received CASE funding from the British Geological Survey. Nick Riley (Carboniferous Limited) is thanked for sharing his expertise and assistance. Charlotte Watts is thanked for providing field assistance. Nick Marsh, Tom Knott, Cheryl Haidon and Annika Burns are thanked for offering expertise and laboratory assistance. Pete Sadler (University of California) is thanked for compilation and provision of the background sediment accumulation rate dataset. We thank all reviewers, Editor Peir Pufahl and Elaine Richardson (Editorial Office) for their valuable comments and advice, which have significantly improved this manuscript.

DATA AVAILABILITY

Data are available via open access (Emmings *et al.*, 2017a,b).

REFERENCES

Aitkenhead, N., **Bridge, D.**, **Riley, N.J.** and **Kimbell, S.** (1992) *Geology of the country around Garstang: memoir for 1:50 000 sheet 67*. HMSO, London.

Algeo, T.J., **Hoffman, D.L.**, **Maynard, J.B.**, **Joachimski, M.M.**, **Hower, J.C.** and **Watney, W.L.** (1997) Environmental reconstruction of anoxic marine systems: core black shales of upper pennsylvanian midcontinent cyclothems. In: *Cyclic Sedimentation of Appalachian Devonian and Midcontinent Pennsylvanian Black Shales: Analysis of Ancient Anoxic Marine Systems—A Combined Core and Field Workshop* (Eds T.J. Algeo and J.B. Maynard), pp. 103–147. Joint Meeting of Eastern Section AAPG and The Society for Organic Petrography (TSOP), Lexington, KY.

Algeo, T., **Heckel, P.H.**, **Maynard, J.B.**, **Blakey, R.** and **Rowe, H.** (2008) Modern and ancient epeiric seas and the superestuarine circulation model of marine anoxia. In: *Dynamics of Epeiric Seas: Sedimentological, Paleontological and Geochemical Perspectives* (Eds B.R. Pratt and C. Holmden), *Geological Association of Canada, Special Paper*, **48**, 7–38.

Alldredge, A.L. and **Silver, M.W.** (1988) Characteristics, dynamics and significance of marine snow. *Prog. Oceanogr.*, **20**, 41–82.

Andrews, I.J. (2013) The Carboniferous Bowland Shale gas study: geology and resource estimation. *Br. Geol. Sur. Dep. Energy Clim. Change*.

Aplin, A.C. and **Macquaker, J.H.S.** (2011) Mudstone diversity: Origin and implications for source, seal, and reservoir properties in petroleum systems. *AAPG Bull.*, **95**, 2031–2059.

Arthurton, R.S. (1972) *Record of Shaft or Borehole*. Cominco S9, Institute of Geological Sciences.

Arthurton, R.S. (1984) The Ribblesdale fold belt, NW England—a Dinantian-early Namurian dextral shear zone. In: *Variscan Tectonics of the North Atlantic Region* (Eds D.H.W. Hutton and D.J. Sanderson) *Geological Society, London, Special Publications*, **14**, 131–138.

Arthurton, R.S., **Mundy, D.W.**, **Johnson, E.W.** and British Geological Survey (1988) *Geology of the country around Settle*. HMSO, London, ix, 147 pp.

Baas, J.H., **Best, J.L.**, **Peakall, J.** and **Wang, M.** (2009) A phase diagram for turbulent, transitional, and laminar clay suspension flows. *J. Sediment. Res.*, **79**, 162–183.

Baas, J.H., **Best, J.L.** and **Peakall, J.** (2011) Depositional processes, bedform development and hybrid bed formation in rapidly decelerated cohesive (mud–sand) sediment flows. *Sedimentology*, **58**, 1953–1987.

Baines, J.G. (1977) *The stratigraphy and sedimentology of the skipton moor grits (Namurian E1c) and their lateral equivalents*. Unpublished PhD Thesis. University of Keele, Keele.

Berner, R.A. and **Canfield, D.E.** (1989) A new model for atmospheric oxygen over Phanerozoic time. *Am. J. Sci.*, **289**, 333–361.

Berner, R.A. and **Raiswell, R.** (1984) C/S method for distinguishing freshwater from marine sedimentary rocks. *Geology*, **12**, 365–368.

Bisat, W.S. (1923) The carboniferous goniatites of the north of England and their zones. *Proc. Yorkshire Geol. Soc.*, **20**, 40–124.

Bojanowski, M.J. and **Clarkson, E.N.K.** (2012) Origin of siderite concretions in microenvironments of methanogenesis developed in a sulfate reduction zone: an exception or a rule? *J. Sediment. Res.*, **82**, 585–598.

Bouma, A.H. (1962) *Sedimentology of some flysch deposits: a graphic approach to facies interpretation*. Elsevier, Amsterdam, 168 pp.

Bowen, S.H. (1984) Evidence of a detritus food chain based on consumption of organic precipitates. *Bull. Mar. Sci.*, **35**, 440–448.

Braissant, O., **Cailleau, G.**, **Dupraz, C.** and **Verrecchia, E.P.** (2003) Bacterially induced mineralization of calcium carbonate in terrestrial environments: the role of exopolysaccharides and amino acids. *J. Sediment. Res.*, **73**, 485–490.

Brandon, A., **Aitkenhead, N.**, **Crofts, R.**, **Ellison, R.**, **Evans, D.** and **Riley, N.** (1998) *Geology of the Country around Lancaster: Memoir for 1:50 000 sheet 59 (England and Wales)*. The Stationery Office, London, 193 pp.

Calvert, S.E., **Bustin, R.M.** and **Pedersen, T.F.** (1992) Lack of evidence for enhanced preservation of sedimentary organic matter in the oxygen minimum of the Gulf of California. *Geology*, **20**, 757–760.

Camp, W.K., **Diaz, E.** and **Wawak, B.** (2013) *Electron Microscopy of Shale Hydrocarbon Reservoirs*, AAPG, Tulsa, OK, 306 pp.

Caron, D.A., **Michaels, A.F.**, **Swanberg, N.R.** and **Howse, F.A.** (1995) Primary productivity by symbiont-bearing planktonic sarcodines (Acantharia, Radiolaria, Foraminifera) in surface waters near Bermuda. *J. Plankton Res.*, **17**, 103–129.

Casey, R. (1993) Radiolaria. In: *Fossil Prokaryotes and Protists* (Ed. J. Lipps), pp. 249–284. Blackwell Science, Boston, MA.

Church, K.D. and **Gawthorpe, R.L.** (1994) High resolution sequence stratigraphy of the late Namurian in the Widmerpool Gulf (East Midlands, UK). *Mar. Pet. Geol.*, **11**, 528–544.

Clarke, H., **Turner, P.**, **Bustin, R.M.**, **Riley, N.** and **Besly, B.** (2018) Shale gas resources of the Bowland Basin, NW England: a holistic study. *Petrol. Geosci.*, **24**, 287–322. https://doi.org/10.1144/petgeo2017-066

Collinson, J.D. (1988) Controls on Namurian sedimentation in the Central Province basins of northern England. In: *Sedimentation in a Synorogenic Basin Complex: The Upper Carboniferous of Northwest Europe* (Eds B.M. Besly and G. Kelling), pp. 85–101. Blackie, Glasgow.

Cope, J.C.W., **Guion, P.D.**, **Sevastopulo, G.D.** and **Swan, A.R.H.** (1992) Carboniferous. In: *Atlas of palaeogeography and lithofacies* (Eds J.C.W. Cope, J.K. Ingham and P.F. Rawson), *Geological Society, London*, **13**, 67–86.

Covault, J.A. and **Graham, S.A.** (2010) Submarine fans at all sea-level stands: Tectono-morphologic and climatic controls on terrigenous sediment delivery to the deep sea. *Geology*, **38**, 939–942.

Curtis, C.D. (1977) Geochemistry: Sedimentary geochemistry: environments and processes dominated by involvement of an aqueous phase. *Philos. Trans. R. Soc. London. Ser. A, Math. Phys. Sci.*, **286**, 353–372.

Davies, S.J. (2008) The record of Carboniferous sea-level change in low-latitude sedimentary successions from Britain and Ireland during the onset of the late Paleozoic ice age. In: *Resolving the Late Paleozoic Ice Age in Time and Space* (Eds C.R. Fielding, T.D. Frank and J.L. Isbell), *Geological Society of America Special Papers*, **441**, 187–204.

Davies, R.J., **Austin, R.** and **Moore, D.** (1993) Environmental controls of Brigantian conodont-distribution: evidence from the Gayle limestone of the Yoredale Group in Northern England. *Annales de la Société géologique de Belgique*, **116**, 221–241.

Davies, S., **Hampson, G.**, **Flint, S.** and **Elliott, T.** (1999) Continental-scale sequence stratigraphy of the Namurian, Upper Carboniferous and its applications to reservoir prediction. *Geol. Soc., London, Petrol. Geol. Conf. Ser.*, **5**, 757–770.

Davies, S.J., **Leng, M.J.**, **Macquaker, J.H.S.** and **Hawkins, K.** (2012) Sedimentary process control on carbon isotope composition of sedimentary organic matter in an ancient shallow-water shelf succession. *Geochem. Geophys. Geosyst.*, **13**, 1–15.

Davies, N.S., **Liu, A.G.**, **Gibling, M.R.** and **Miller, R.F.** (2016) Resolving MISS conceptions and misconceptions: A geological approach to sedimentary surface textures generated by microbial and abiotic processes. *Earth Sci. Rev.*, **154**, 210–246.

Davydov, V.I., **Crowley, J.L.**, **Schmitz, M.D.** and **Poletaev, V.I.** (2010) High-precision U-Pb zircon age calibration of the global Carboniferous time scale and Milankovitch band cyclicity in the Donets Basin, eastern Ukraine. *Geochem. Geophys. Geosyst.*, **11**, 1–22. https://doi.org/10.1029/2009gc002736

Dean, M.T., **Browne, M.A.E.**, **Waters, C.N.** and **Powell, J.H.** (2011) A lithostratigraphical framework for the Carboniferous successions of northern Great Britain (Onshore). British Geological Survey Research Report RR/10/07, 174 pp.

DECC (2016) https://www.gov.uk/government/uploads/system/uploads/attachment_data/file/504823/Landwells23Feb2016_xlsx.

Demaison, G.J. and **Moore, G.T.** (1980) Anoxic environments and oil source bed genesis. *Org. Geochem.*, **2**, 9–31.

Drewery, S., **Cliff, R.A.** and **Leeder, M.R.** (1987) Provenance of Carboniferous sandstones from U-Pb dating of detrital zircons. *Nature*, **325**, 50–53.

Dunham, K. (1990) Geology of the northern Pennine Orefield: Economic memoir covering the areas of 1:50000 and one-inch geological sheets 19 and 25 and parts of 13, 24, 26, 31, 32 (England and Wales) volume 1 Tyne to Stainmore. *Memoirs of the Geological Survey*. HMSO, London.

Dunham, A.C. and **Wilson, A.A.** (1985) Geology of the Northern Pennine Orefield : Economic memoir covering the areas of one-inch and 1:50,000 geological sheets 40, 41 and 50, and parts of 31, 32, 51, 60 and 61, New Series Volume 2 Stainmore to Craven.

Dupraz, C., **Visscher, P.T.**, **Baumgartner, L.K.** and **Reid, R.P.** (2004) Microbe–mineral interactions: early carbonate precipitation in a hypersaline lake (Eleuthera Island, Bahamas). *Sedimentology*, **51**, 745–765.

Eagar, R.M.C., **Baines, J.G.**, **Collinson, J.D.**, **Hardy, P.G.**, **Okolo, S.A.** and **Pollard, J.E.** (1985) Trace fossil

assemblages and their occurrence in Silesian (mid-Carboniferous) deltaic sediments of the central pennine basin, England. In: *Biogenic Structures, Their Use in Interpreting Depositional Environments* (Ed. H.A. Curran), *SEPM Special Publication*, **35**, 99–149.

Earp, J.R. (1961) *Geology of the country around Clitheroe and Nelson (one-inch geological sheet 68, new series)*. HMSO, London.

Egbert, G.D., **Ray, R.D.** and **Bills, B.G.** (2004) Numerical modeling of the global semidiurnal tide in the present day and in the last glacial maximum. *J. Geophys. Res. Oceans*, **109**, 1–15. https://doi.org/10.1029/2003JC001973.

Elliott, T. (1975) The sedimentary history of a delta lobe from a yoredale (Carboniferous) cyclothem. *Proc. Yorkshire Geol. Soc.*, **40**, 505–536.

Emmings, J., **Davies, S.**, **Vane, C.H.**, **Leng, M.**, **Moss-Hayes, V.** and **Stephenson, M.** (2017a) *Bowland Shale Dataset: Field and Sample Photographs, Sample Descriptions, Microphotographs, X-Ray Fluorescence, LECO Elemental Analysis, X-Ray Diffraction and RockEval Pyrolysis from Hind Clough, MHD4 and Cominco S9*. British Geological Survey. Available at: https://doi.org/10.5285/9ceadcad-a93c-4bab-8ca1-07b0de2c5ed0.

Emmings, J., **Davies, S.**, **Vane, C.H.**, **Leng, M.**, **Moss-Hayes, V.**, **Stephenson, M.** and **Jenkin, G.** (2017b) *Data Accompanying: Stream and Slope Weathering Effects on Organic-rich Mudstone Geochemistry and Implications for Hydrocarbon Source Rock Assessment: A Bowland Shale Case Study*. British Geological Survey. Available at: http://www.bgs.ac.uk/services/ngdc/accessions/index.html#item72789.

Emmings, J., **Davies, S.**, **Vane, C.H.**, **Leng, M.**, **Moss-Hayes, V.**, **Stephenson, M.** and **Jenkin, G.** (2017c) Stream and slope weathering effects on organic-rich mudstone geochemistry and implications for hydrocarbon source rock assessment: a bowland shale case study. *Chem. Geol.*, **471**, 74–91.

Ettensohn, F.R. (1997) Assembly and dispersal of Pangea: Large-scale tectonic effects on coeval deposition of North American, marine, epicontinental, black shales. *J. Geodyn.*, **23**, 287–309.

Fairbairn, R.A. (2001) The stratigraphy of the namurian great/main limestone on the alston block, stainmore trough and askrigg block of northern England. *Proc. Yorkshire Geol. Polytech. Soc.*, **53**, 265–274.

Fauchille, A.L., **Ma, L.**, **Rutter, E.**, **Chandler, M.**, **Lee, P.D.** and **Taylor, K.G.** (2017) An enhanced understanding of the Basinal Bowland shale in Lancashire (UK), through microtextural and mineralogical observations. *Mar. Pet. Geol*, **86**, 1374–1390.

Flügel, E. (2004) *Microfacies of Carbonate Rocks: Analysis, Interpretation and Application*. Springer-Verlag, Berlin, Heidelberg, 976 pp.

Fonnesu, M., **Felletti, F.**, **Haughton, P.D.W.**, **Patacci, M.** and **McCaffrey, W.D.** (2017) Hybrid event bed character and distribution linked to turbidite system sub-environments: The North Apennine Gottero Sandstone (north-west Italy). *Sedimentology*, **65**, 151–190.

Fortey, R.A. and **Wilmot, N.V.** (1991) Trilobite cuticle thickness in relation to palaeoenvironment. *Paläontologische Zeitschrift*, **65**, 141–151.

Fraser, A.J. and **Gawthorpe, R.L.** (1990) Tectono-stratigraphic development and hydrocarbon habitat of the Carboniferous in northern England. In: *Tectonic Events Responsible for Britain's Oil and Gas* (Eds R.F.P. Hardman and J. Brooks), *Geological Society of London Special Publication*, **55**, 49–86.

Fraser, A.J. and **Gawthorpe, R.** (2003) *An Atlas of Carboniferous Basin Evolution in Northern England*. Geological Society, London, Memoir 28, 88 pp.

Galloway, W.E. (1989) Genetic stratigraphic sequences in basin analysis; I, Architecture and genesis of flooding-surface bounded depositional units. *AAPG Bull.*, **73**, 125–142.

Gastaldo, R.A., **Purkyňová, E.**, **Šimůnek, Z.** and **Schmitz, M.D.** (2009) Ecological persistence in the late Mississippian (Serpukhovian, Namurian A) megafloral record of the upper silesian basin, Czech Republic. *Palaios*, **24**, 336–350.

Gawthorpe, R. (1987) Tectono-sedimentary evolution of the Bowland Basin, N England, during the Dinantian. *J. Geol. Soc.*, **144**, 59–71.

Gross, D., **Sachsenhofer, R.F.**, **Bechtel, A.**, **Pytlak, L.**, **Rupprecht, B.** and **Wegerer, E.** (2015) Organic geochemistry of Mississippian shales (Bowland Shale Formation) in central Britain: Implications for depositional environment, source rock and gas shale potential. *Mar. Pet. Geol*, **59**, 1–21.

Grunke, S., **Felden, J.**, **Lichtschlag, A.**, **Girnth, A.C.**, **De Beer, D.**, **Wenzhofer, F.** and **Boetius, A.** (2011) Niche differentiation among mat-forming, sulfide-oxidizing bacteria at cold seeps of the Nile Deep Sea Fan (Eastern Mediterranean Sea). *Geobiology*, **9**, 330–348.

Hampson, G.J. (2010) Sediment dispersal and quantitative stratigraphic architecture across an ancient shelf. *Sedimentology*, **57**, 96–141.

Hampson, G.J., **Elliott, T.** and **Davies, S.J.** (1997) The application of sequence stratigraphy to Upper Carboniferous fluvio-deltaic strata of the onshore UK and Ireland: implications for the southern North Sea. *J. Geol. Soc.*, **154**, 719–733.

Harris, N.B., **Mnich, C.A.**, **Selby, D.** and **Korn, D.** (2013) Minor and trace element and Re–Os chemistry of the Upper Devonian Woodford Shale, Permian Basin, west Texas: Insights into metal abundance and basin processes. *Chem. Geol*, **356**, 76–93.

Haughton, P.D.W., **Barker, S.P.** and **McCaffrey, W.D.** (2003) 'Linked' debrites in sand-rich turbidite systems – origin and significance. *Sedimentology*, **50**, 459–482.

Haughton, P., **Davis, C.**, **McCaffrey, W.** and **Barker, S.** (2009) Hybrid sediment gravity flow deposits – Classification, origin and significance. *Mar. Pet. Geol.*, **26**, 1900–1918.

Hennissen, J.A.I., **Hough, E.**, **Vane, C.H.**, **Leng, M.J.**, **Kemp, S.J.** and **Stephenson, M.H.** (2017) The prospectivity of a potential shale gas play: An example from the southern Pennine Basin (central England, UK). *Mar. Pet. Geol.*, **86**, 1047–1066. https://doi.org/10.1016/j.marpetgeo.2017.06.033

Hild, E. and **Brumsack, H.J.** (1998) Major and minor element geochemistry of Lower Aptian sediments from the NW German Basin (core Hohenegglesen KB 40). *Cretac. Res.*, **19**, 615–633.

Holdsworth, B. and **Collinson, J.D.** (1988) Millstone Grit cyclicity revisited. In: *Sedimentation in a Synorogenic Basin Complex: The Upper Carboniferous of Northwest Europe* (Eds B.M. Besly and G. Kelling), pp. 132–152. Blackie, Glasgow.

Hudson, R.G.S. (1940) The mirk fell beds (Namurian, E_2) of tan hill, Yorkshire. *Proc. Yorkshire Geol. Polytech. Soc.*, **24**, 259–289.

Hunt, A., **Lucas, S.**, **Spielmann, J.** and **Lockley, M.** (2012) Bromalites from the Mississippian bear gulch lagerstätte of

central Montana, USA. *Vert. Coprol. New Mexico Mus. Nat. His. Sci., Bull.*, **57**, 171–174.

Illing, L. (1954) Bahaman calcareous sands. *AAPG Bull.*, **38**, 1–95.

Jarvie, D.M., **Hill, R.J.**, **Ruble, T.E.** and **Pollastro, R.M.** (2007) Unconventional shale gas systems: The Mississippian Barnett Shale of north-central Texas as one model for thermogenic shale gas assessment. In: *Barnett Shale* (Eds R.J. Hill and D.M. Jarvie), *AAPG Bull.*, **91**, 475–499.

Kane, I.A. (2010) Development and flow structures of sand injectities: The Hind Sandstone Member injectite complex, Carboniferous, UK. *Mar. Pet. Geol.*, **27**, 1200–1215.

Kane, I.A., **McCaffrey, W.D.** and **Martinsen, O.J.** (2009) Allogenic vs. Autogenic Controls on Megaflute Formation. *J. Sediment. Res.*, **79**, 643–651.

Kastner, M., **Keene, J.B.** and **Gieskes, J.M.** (1977) Diagenesis of Siliceous Oozes. 1. Chemical Controls on Rate of Opal-a to Opal-CT Transformation - Experimental-Study. *Geochim. Cosmochim. Acta*, **41**, 1041–1059.

Keil, R.G., **Montlucon, D.B.**, **Prahl, F.G.** and **Hedges, J.I.** (1994) Sorptive preservation of labile organic matter in marine sediments. *Nature*, **370**, 549–552.

Kennedy, M.J., **Löhr, S.C.**, **Fraser, S.A.** and **Baruch, E.T.** (2014) Direct evidence for organic carbon preservation as clay-organic nanocomposites in a Devonian black shale; from deposition to diagenesis. *Earth Planet Sci Lett*, **388**, 59–70.

Kerschke, D. and **Schulz, H.-M.** (2013) The shale gas potential of Tournaisian, Visean, and Namurian black shales in North Germany: baseline parameters in a geological context. *Environ. Earth Sci.*, **70**, 3817–3837.

Keulegan, G.H. and **Krumbein, W.C.** (1949) Stable configuration of bottom slope in a shallow sea and its bearing on geological processes. *EOS Trans. Am. Geophys. Union*, **30**, 855–861.

Kirby, G.A., **Baily, H.E.**, **Chadwick, R.A.**, **Evans, D.J.**, **Holliday, D.W.**, **Holloway, S.**, **Hulbert, A.G.**, **Pharaoh, T.C.**, **Smith, N.J.P.**, **Aitkenhead, N.** and **Birch, B.** (2000) *Structure and Evolution of the Craven Basin and Adjacent Areas.* Subsurface Memoir of the British Geological Survey, The Stationery Office, London, 148 pp.

Klein, G.D. and **Ryer, T.A.** (1978) Tidal circulation patterns in Precambrian, Paleozoic, and Cretaceous epeiric and mioclinal shelf seas. *Geol. Soc. Am. Bull.*, **89**, 1050–1058.

Könitzer, S.F., **Davies, S.**, **Stephenson, M.** and **Leng, M.** (2014) Depositional controls on mudstone lithofacies in a basinal setting: implications for the delivery of sedimentary organic matter. *J. Sediment. Res.*, **84**, 198–214.

Ku, T.C.W., **Walter, L.M.**, **Coleman, M.L.**, **Blake, R.E.** and **Martini, A.M.** (1999) Coupling between sulfur recycling and syndepositional carbonate dissolution: evidence from oxygen and sulfur isotope composition of pore water sulfate, South Florida Platform, U.S.A. *Geochim. Cosmochim. Acta*, **63**, 2529–2546.

Lawrence, S.R., **Coster, P.W.** and **Ireland, R.J.** (1987) Structural development and petroleum potential of the northern flanks of the Bowland Basin (Carboniferous), North-west England. In: *Proceedings of the 3rd Conference on Petroleum Geology of North West Europe* (Eds J. M. Brooks and K. Glennie), **1**, pp. 225–233. Graham & Trotman, London.

Lazar, O.R., **Bohacs, K.M.**, **Macquaker, J.H.S.**, **Schieber, J.** and **Demko, T.M.** (2015) Capturing Key Attributes Of Fine-Grained Sedimentary Rocks In Outcrops, Cores And Thin Sections: Nomenclature And Description Guidelines. *J. Sediment. Res.*, **85**, 230–246.

Leeder, M.R. (1982) Upper Palaeozoic basins of the British Isles—Caledonide inheritance versus Hercynian plate margin processes. *J. Geol. Soc.*, **139**, 479–491.

Li, Z., **Bhattacharya, J.** and **Schieber, J.** (2015) Evaluating along-strike variation using thin-bedded facies analysis, Upper Cretaceous Ferron Notom Delta, Utah. *Sedimentology*, **62**, 2060–2089.

Lobza, V. and **Schieber, J.** (1999) Biogenic sedimentary structures produced by worms in soupy, soft muds; observations from the Chattanooga Shale (Upper Devonian) and experiments. *J. Sediment. Res.*, **69**, 1041–1049.

Loucks, R. and **Ruppel, S.** (2007) Mississippian Barnett Shale: Lithofacies and depositional setting of a deep-water shale-gas succession in the Fort Worth Basin, Texas. *AAPG Bull.*, **91**, 579–601.

Loutit, T.S., **Hardenbol, J.**, **Vail, P.R.** and **Baum, G.R.** (1988) Condensed sections: the key to age determination and correlation of continental margin sequences. In: *Sea-Level Changes: An Integrated Approach* (Eds C.K. Wilgus, B.S. Hastings, H. Posamentier, J.V. Wagoner, C.A. Ross and C.G.S.C. Kendall), *SEPM Special Publication*, **42**, 183–213.

Macquaker, J.H.S., **Keller, M.A.** and **Davies, S.J.** (2010) Algal blooms and "Marine Snow": mechanisms that enhance preservation of organic carbon in ancient fine-grained sediments. *J. Sediment. Res.*, **80**, 934–942.

Macquaker, J.H.S., **Taylor, K.G.**, **Keller, M.A.** and **Polya, D.** (2014) Compositional controls on early diagenetic pathways in fine-grained sedimentary rocks: Implications for predicting unconventional reservoir attributes of mudstones. *AAPG Bull.*, **98**, 587–603.

Mann, K.H. (1988) Production and use of detritus in various freshwater, estuarine, and coastal marine ecosystems. *Limnol. Oceanogr.*, **33**, 910–930.

Martinsen, O. (1993) Namurian (Late Carboniferous) Depositional Systems of the Craven-Area, Northern England: Implications for Sequence-Stratigraphic Models. In: *Sequence Stratigraphy and Facies Associations* (Eds H.W. Posamentier, C.P. Summerhayes, B.U. Haq and G.P. Allen), *IAS Special Publication*, **18**, 247–281.

Martinsen, O.J., **Collinson, J.D.** and **Holdsworth, B.K.** (1995) Millstone grit cyclicity revisited, II: sequence stratigraphy and sedimentary responses to changes of relative sea-level. In: *Sedimentary Facies Analysis* (Ed. A.G. Plint), *IAS Special Publication*, **22**, 305–327.

Maslin, M., **Owen, M.**, **Day, S.** and **Long, D.** (2004) Linking continental-slope failures and climate change: Testing the clathrate gun hypothesis. *Geology*, **32**, 53–56.

Maynard, J.R. and **Leeder, M.R.** (1992) On the periodicity and magnitude of Late Carboniferous glacio-eustatic sea-level changes. *J. Geol. Soc.*, **149**, 303–311.

McCave, I.N. and **Jones, K.P.N.** (1988) Deposition of ungraded muds from high-density non-turbulent turbidity currents. *Nature*, **333**, 250–252.

Mercedes-Martín, R., **Rogerson, M.R.**, **Brasier, A.T.**, **Vonhof, H.B.**, **Prior, T.J.**, **Fellows, S.M.**, **Reijmer, J.J.G.**, **Billing, I.** and **Pedley, H.M.** (2016) Growing spherulitic calcite grains in saline, hyperalkaline lakes: experimental evaluation of the effects of Mg-clays and organic acids. *Sed. Geol.*, **335**, 93–102.

Mitchum, R.M. and **Van Wagoner, J.C.** (1991) High-frequency sequences and their stacking patterns: sequence-stratigraphic evidence of high-frequency eustatic cycles. *Sed. Geol.*, **70**, 131–160.

Mitra, A., **Flynn, K.J.**, **Tillmann, U.**, **Raven, J.A.**, **Caron, D.**, **Stoecker, D.K.**, **Not, F.**, **Hansen, P.J.**, **Hallegraeff, G.**, **Sanders, R.**, **Wilken, S.**, **McManus, G.**, **Johnson, M.**, **Pitta, P.**, **Våge, S.**, **Berge, T.**, **Calbet, A.**, **Thingstad, F.**, **Jeong, H.J.**, **Burkholder, J.**, **Glibert, P.M.**, **Granéli, E.** and **Lundgren, V.** (2016) Defining planktonic protist functional groups on mechanisms for energy and nutrient acquisition: incorporation of diverse mixotrophic strategies. *Protist*, **167**, 106–120.

Moore, T.S., **Murray, R.W.**, **Kurtz, A.C.** and **Schrag, D.P.** (2004) Anaerobic methane oxidation and the formation of dolomite. *Earth Planet. Sci. Lett.*, **229**, 141–154.

Moseley, F. (1952) The namurian of the Lancaster fells. *Quart. J. Geol. Soc.*, **109**, 423–450 NP, 451–454.

Moseley, F. (1962) The structure of the south-western part of the sykes anticline, Bowland, West Yorkshire. *Proc. Yorkshire Geol. Polytech. Soc.*, **33**, 287–314.

Neumann, A.C., **Gebelein, C.D.** and **Scoffin, T.P.** (1970) The composition, structure and erodability of subtidal mats, Abaco, Bahamas. *J. Sediment. Res.*, **40**, 274–297.

Newport, S.M., **Jerrett, R.M.**, **Taylor, K.G.**, **Hough, E.** and **Worden, R.H.** (2018) Sedimentology and microfacies of a mud-rich slope succession: in the Carboniferous Bowland Basin, NW England (UK). *J. Geol. Soc.*, **175**, 247–262.

Nyberg, B. and **Howell, J.A.** (2015) Is the present the key to the past? A global characterization of modern sedimentary basins. *Geology*, **43**, 643–646.

Nyhuis, C.J., **Riley, D.** and **Kalasinska, A.** (2015) Thin section petrography and chemostratigraphy: Integrated evaluation of an upper Mississippian mudstone dominated succession from the southern Netherlands. *Netherlands J. Geosci. - Geologie en Mijnbouw*, **95**, 3–22.

Peters, S. and **Loss, D.** (2012) Storm and fair-weather wave base: A relevant distinction? *Geology*, **40**, 511–514.

Piper, D. (1978) Turbidite muds and silts on deepsea fans and abyssal plains. In: *Sedimentation in Submarine Canyons, Fans, and Trenches* (Eds D.J. Stanley and G. Kelling), pp. 163–176. Dowden, Hutchinson & Ross, Stroudsburg, PA.

Piper, D.J.W. and **Normark, W.R.** (2009) Processes that initiate turbidity currents and their influence on turbidites: a marine geology perspective. *J. Sediment. Res.*, **79**, 347–362.

Porter, K.G. and **Robbins, E.I.** (1981) Zooplankton Fecal Pellets Link Fossil Fuel and Phosphate Deposits. *Science*, **212**, 931–933.

Posamentier, H.W., **Jervey, M.T.** and **Vail, P.R.** (1988) Eustatic controls on clastic deposition i - conceptual framework. In: *Sea-Level Changes: An Integrated Approach* (Eds C.K. Wilgus, B.S. Hastings, H. Posamentier, J. Van Wagoner, C.A. Ross and C.G.St.C. Kendall), *Society of Economic Paleontologists and Mineralogists Special Publication*, **42**, 110–124.

Rahman, H.M., **Kennedy, M.**, **Löhr, S.** and **Dewhurst, D.N.** (2017) Clay-organic association as a control on hydrocarbon generation in shale. *Org. Geochem.*, **105**, 42–55.

Ramsbottom, W.H.C. (1973) Transgressions and regressions in the dinantian: a new synthesis of british dinantian stratigraphy. *Proc. Yorkshire Geol. Polytech. Soc.*, **39**, 567–607.

Ramsbottom, W.H.C. (1977) Major cycles of transgression and regression (mesothems) in the Namurian. *Proc. Yorkshire Geol. Polytech. Soc.*, **41**, 261–291.

Ramsbottom, W.H.C. (1979) Rates of transgression and regression in the Carboniferous of NW Europe. *J. Geol. Soc.*, **136**, 147–153.

Ramsbottom, W.H.C. and **Saunders, W.B.** (1985) Evolution and Evolutionary Biostratigraphy of Carboniferous Ammonoids. *J. Paleontol.*, **59**, 123–139.

Ramsbottom, W.H.C., **Rhys, G.J.** and **Smith, E.G.** (1962) Boreholes in the Carboniferous rocks of the Ashover district. *Derbyshire, Bull. Geol. Sur. Great Britain*, **19**, 75–168.

Rebesco, M., **Hernández-Molina, F.J.**, **Van Rooij, D.** and **Wåhlin, A.** (2014) Contourites and associated sediments controlled by deep-water circulation processes: State-of-the-art and future considerations. *Mar. Geol.*, **352**, 111–154.

Rickard, D. (2012) Sedimentary pyrite. In: *Sulfidic Sediments and Sedimentary Rocks* (Ed. D. Rickard) *Developments in Sedimentology*, **65**, 233–285.

Riley, G.A. (1971) Particulate organic matter in sea water. *Adv. Mar. Biol.*, **8**, 1–118.

Riley, N. (1988) Stratigraphy of the BP Minerals BH MHD 4, Marl Hill, Whitewell, Lancs. *BGS Technical Report No. WH/88/300R.*

Riley, N.J. (1990) Stratigraphy of the Worston Shale Group (Dinantian), Craven Basin, north-west England. *Proc. Yorkshire Geol. Polytech. Soc.*, **48**, 163–187.

Röhl, H.-J., **Schmid-Röhl, A.**, **Oschmann, W.**, **Frimmel, A.** and **Schwark, L.** (2001) The Posidonia Shale (Lower Toarcian) of SW-Germany: an oxygen-depleted ecosystem controlled by sea level and palaeoclimate. *Palaeogeogr. Palaeoclimatol. Palaeoecol.*, **165**, 27–52.

Rowell, A.J. and **Scanlon, J.E.** (1957) The Relation Between The Yoredale Series And The Millstone Grit On The Askrigg Block. *Proc. Yorkshire Geol. Polytech. Soc.*, **31**, 79–90.

Rygel, M.C., **Fielding, C.R.**, **Frank, T.D.** and **Birgenheier, L.P.** (2008) The magnitude of late paleozoic glacioeustatic fluctuations: a synthesis. *J. Sediment. Res.*, **78**, 500–511.

Saba, G.K. and **Steinberg, D.K.** (2012) Abundance, composition, and sinking rates of fish fecal pellets in the santa barbara channel. *Sci. Rep.*, **2**, 716. Available at: https://www.nature.com/articles/srep00716

Sadler, P. (1999) The influence of hiatuses on sediment accumulation rates. *GeoRes. Forum*, **5**, 15–40.

Sadler, P.M. (1981) Sediment Accumulation Rates and the Completeness of Stratigraphic Sections. *J. Geol*, **89**, 569–584.

Sadler, P.M. and **Jerolmack, D.J.** (2014) Scaling laws for aggradation, denudation and progradation rates: the case for time-scale invariance at sediment sources and sinks. In: *Strata and Time: Probing the Gaps in Our Understanding* (Eds D.G. Smith, R.J. Bailey, P.M. Burgess and A.J. Fraser), *Geological Society, London, Special Publications*, **404**, 69–88.

Salmon, V., **Derenne, S.**, **Lallier-Vergès, E.**, **Largeau, C.** and **Beaudoin, B.** (2000) Protection of organic matter by mineral matrix in a Cenomanian black shale. *Org. Geochem.*, **31**, 463–474.

Schieber, J. (1986) The possible role of benthic microbial mats during the formation of carbonaceous shales in shallow Mid-Proterozoic basins. *Sedimentology*, **33**, 521–536.

Schieber, J. (1994) Evidence for high-energy events and shallow-water deposition in the Chattanooga Shale, Devonian, central Tennessee, USA. *Sed. Geol.*, **93**, 193–208.

Schieber, J. (2004) Microbial mats in the siliciclastic rock record: a summary of diagnostic features. In: *The*

Precambian Earth: Tempos and Events, Developments in Precambrian Geology (Eds P. Eriksson, W. Altermann, D. Nelson, W. Mueller, O. Catuneanu and K. Strand), pp. 663–672. Elsevier Science.

Schieber, J. (2016) Mud re-distribution in epicontinental basins – Exploring likely processes. *Mar. Pet. Geol.*, **71**, 119–133.

Schieber, J., **Krinsley, D.** and **Riciputi, L.** (2000) Diagenetic origin of quartz silt in mudstones and implications for silica cycling. *Nature*, **406**, 981–985.

Schieber, J., **Southard, J.** and **Thaisen, K.** (2007a) Accretion of mudstone beds from migrating floccule ripples. *Science*, **318**, 1760–1763.

Schieber, J., **Sur, S.** and **Banerjee, S.** (2007b) Benthic microbial mats in black shale units from the Vindhyan Supergroup, Middle Proterozoic of India: the challenges of recognizing the genuine article. In: *Atlas of Microbial Mat Features Preserved Within the Clastic Rock Record* (Eds J. Schieber, P. Bose, P. Eriksson, S. Banerjee, S. Sarkar, W. Altermann and O. Catuneau), pp. 189–197. Elsevier, Amsterdam.

Schieber, J., **Southard, J.** and **Schimmelmann, A.** (2010) Lenticular shale fabrics resulting from intermittent erosion of water-rich muds - interpreting the rock record in the light of recent flume experiments. *J. Sediment. Res.*, **80**, 119–128.

Selley, R.C. (Ed.) (2000) Particles, pores, and permeability. In: *Applied Sedimentology*, 2nd edn, pp. 41–86. Academic Press, San Diego, CA.

Sholkovitz, E.R. and **Price, N.B.** (1980) The major-element chemistry of suspended matter in the Amazon Estuary. *Geochim. Cosmochim. Acta*, **44**, 163–171.

Słowakiewicz, M., **Tucker, M.E.**, **Vane, C.H.**, **Harding, R.**, **Collins, A.** and **Pancost, R.D.** (2015) Shale-Gas potential of the mid-carboniferous bowland-hodder unit in the Cleveland basin (Yorkshire), Central Britain. *J. Pet. Geol*, **38**, 59–75.

Spears, D.A. (2006) Clay mineralogy of onshore UK Carboniferous mudrocks. *Clay Miner.*, **41**, 395–416.

Stow, D.A.V. and **Bowen, A.J.** (1978) Origin of lamination in deep sea, fine-grained sediments. *Nature*, **274**, 324–328.

Stow, D.A.V. and **Shanmugam, G.** (1980) Sequence of structures in fine-grained turbidites: Comparison of recent deep-sea and ancient flysch sediments. *Sed. Geol.*, **25**, 23–42.

Sumner, E.J., **Talling, P.J.** and **Amy, L.A.** (2009) Deposits of flows transitional between turbidity current and debris flow. *Geology*, **37**, 991–994.

Sztanó, O. and **Boer, P.L.** (1995) Basin dimensions and morphology as controls on amplification of tidal motions (the Early Miocene North Hungarian Bay). *Sedimentology*, **42**, 665–682.

Talling, P.J. (2014) On the triggers, resulting flow types and frequencies of subaqueous sediment density flows in different settings. *Mar. Geol.*, **352**, 155–182.

Talling, P., **Masson, D.**, **Sumner, E.** and **Malgesini, G.** (2012) Subaqueous sediment density flows: depositional processes and deposit types. *Sedimentology*, **59**, 1937–2003.

Taylor, K.G. and **Macquaker, J.H.S.** (2014) Diagenetic alterations in a silt- and clay-rich mudstone succession: an example from the Upper Cretaceous Mancos Shale of Utah, USA. *Clay Miner.*, **49**, 213–227.

Tissot, B.P. and **Welte, D.H.** (1978) Sedimentary processes and the accumulation of organic matter. In: *Petroleum Formation and Occurrence: A New Approach to Oil and Gas Exploration* (Eds B.P. Tissot and D.H. Welte), pp. 55–62. Springer-Verlag, Berlin, Heidelberg.

Titus, A.L., **Korn, D.**, **Harrell, J.E.** and **Lambert, L.L.** (2015) Late Viséan (late Mississippian) ammonoids from the Barnett Shale, Sierra Diablo Escarpment, Culberson County, Texas, USA. *Foss. Rec.*, **18**, 81–104.

Tribovillard, N., **Algeo, T.**, **Lyons, T.** and **Ruboulleau, A.** (2006) Trace metals as paleoredox and paleoproductivity proxies: An update. *Chem. Geol.*, **232**, 12–32.

Turner, J.T. (2015) Zooplankton fecal pellets, marine snow, phytodetritus and the ocean's biological pump. *Prog. Oceanogr.*, **130**, 205–248.

Tyson, R. (1995) *Sedimentary Organic Matter: Organic Facies and Palynofacies*. Springer, Dordrecht, 615 pp.

Tyson, R.V. (2001) Sedimentation rate, dilution, preservation and total organic carbon: some results of a modelling study. *Org. Geochem.*, **32**, 333–339.

Tyson, R.V. and **Pearson, T.H.** (1991) Modern and ancient continental shelf anoxia: an overview. In: *Modern and Ancient Continental Shelf Anoxia* (Eds R.V. Tyson and T.H. Pearson), *Geological Society, London, Special Publications*, **58**, 1–24.

Veevers, J.J. and **Powell, C.M.** (1987) Late Paleozoic glacial episodes in Gondwanaland reflected in transgressive-regressive depositional sequences in Euramerica. *Geol. Soc. Am. Bull.*, **98**, 475–487.

Velimirov, B. (1987) Organic matter derived from a seagrass meadow: origin, properties, and quality of particles. *Mar. Ecol.*, **8**, 143–173.

Vignaga, E., **Sloan, D.M.**, **Luo, X.**, **Haynes, H.**, **Phoenix, V.R.** and **Sloan, W.T.** (2013) Erosion of biofilm-bound fluvial sediments. *Nat. Geosci.*, **6**, 770–774.

Virtasalo, J.J., **Leipe, T.**, **Moros, M.** and **Kotilainen, A.T.** (2011) Physicochemical and biological influences on sedimentary-fabric formation in a salinity and oxygen-restricted semi-enclosed sea: Gotland Deep, Baltic Sea. *Sedimentology*, **58**, 352–375.

Wang, F. and **Chapman, P.M.** (1999) Biological implications of sulfide in sediment—a review focusing on sediment toxicity. *Environ. Toxicol. Chem.*, **18**, 2526–2532.

Warr, L.N. (2000) The variscan orogeny: the welding of Pangaea. In: *Geological History of Britain and Ireland* (Eds N.H. Woodcock and R. Strachan), pp. 271–294. Wiley-Blackwell, Hoboken, NJ.

Waters, C.N. and **Condon, D.J.** (2012) Nature and timing of Late Mississippian to Mid-Pennsylvanian glacio-eustatic sea-level changes of the Pennine Basin, UK. *J. Geol. Soc.*, **169**, 37–51.

Waters, C.N. and **Davies, S.J.** (2006) Carboniferous: extensional basins, advancing deltas and coal swamps. In: *The Geology of England and Wales* (Ed. P.J. Brenchley), pp. 173–223. Geological Society of London, London.

Waters, C.N., **Waters, R.A.**, **Barclay, W.J.** and **Davies, J.R.** (2009) A lithostratigraphical framework for the Carboniferous successions of southern Great Britain (onshore). *British Geological Survey Research Report* RR/09/01.

Waters, C.N., **Somerville, I.D.**, **Jones, N.S.**, **Cleal, C.J.**, **Collinson, J.D.**, **Waters, R.A.**, **Besly, B.M.**, **Dean, M.T.**, **Stephenson, M.H.**, **Davies, J.R.**, **Freshney, E.C.**, **Jackson, D.I.**, **Mitchell, W.I.**, **Powell, J.H.**, **Barclay, W.J.**, **Browne, M.A.E.**, **Leveridge, B.E.**, **Long, S.L.** and **McLean, D.** (2011) *A revised correlation of Carboniferous rocks in the British Isles*. Geological Society of London, Bath, 186 pp.

Weaver, C. (1989) *Clays, Muds and Shales*. Elsevier Science Publishers B.V, Amsterdam, 819 pp.

Zatoń, M. and **Rakociński, M.** (2014) Coprolite evidence for carnivorous predation in a Late Devonian pelagic environment of southern Laurussia. *Palaeogeogr. Palaeoclimatol. Palaeoecol.*, **394**, 1–11.

Manuscript received 15 April 2018; revision accepted 18 June 2019

Supporting Information

Additional information may be found in the online version of this article:

Appendix S1. Ternary plot with data normalized to 100%. Based on integration of macroscopic and microscopic observations with geochemical data.

Appendix S2. Methodology.